

COMPUTATIONAL INVESTIGATION OF THE DEFECT BEHAVIOR AND SURFACE  
PHENOMENA OF CERAMICS

By

MINKI HONG

A DISSERTATION PRESENTED TO THE GRADUATE SCHOOL  
OF THE UNIVERSITY OF FLORIDA IN PARTIAL FULFILLMENT  
OF THE REQUIREMENTS FOR THE DEGREE OF  
DOCTOR OF PHILOSOPHY

UNIVERSITY OF FLORIDA

2013

© 2013 Minki Hong

To my beloved family, especially Hanna and James

## ACKNOWLEDGMENTS

At the time of finishing my doctoral study, my sincere gratitude should be dedicated to my graduate advisor, Prof. Susan B. Sinnott, for giving me such a great opportunity to explore the world of computational materials science and for guiding me with her best patience and kindness. I should say that I was extremely lucky to have Prof. Simon R. Phillpot as my secondary advisor, for his valuable discussions and good humor throughout my study, and Dr. Blas P. Uberuaga as my co-advisor, for all his hard work, nailing critique, profound discussion, among many other things without which I would never actually be able to succeed with any of my own work. Also, I would like to thank each of my committee members for their support and advice.

I also thank all the members of the Computational Materials Science Focus Group for their mentoring, discussions, helps, and supports. In particular, I deeply thank Dr. Chan-woo Lee for being my mentor when I first joined the group as well as for sharing his precious secrets on how to use VASP. Dr. Dong-hyun Kim, Dong-hwa Lee, and Dr. Aleksandr Chernatynskiy have also been my sincere mentors and friends; I appreciate all their help and the valuable discussions we have had which at times have been very prolonged. I also thank Dr. Rakesh K. Behera for teaching me every detail of GULP.

I need to thank several co-workers outside the group too; Dr. Juan C. Nino enabled my first official collaboration with experimentalist, Hyuck-soo Han. Dr. Beverly Hinojosa provided me with a super useful code to generate DOS plots, which I am still using, as well as several baby products for free. I also thank my Korean friends in the MSE department and my church members for their friendship and support.

Last but not least, I would like to send my grateful heart to my family for all of their love and prayers. Simply and certainly, it would be impossible to continue my doctoral study without all of their support. And most of all, I am humbly thankful to my beloved wife, Hanna, and my beloved son, James. They are the very reason that I have been able to keep myself from falling down.

***“The mountains melted from before the LORD...”***

***Deborah, Judges 5:5***

## TABLE OF CONTENTS

	<u>Page</u>
ACKNOWLEDGMENTS.....	4
LIST OF TABLES.....	8
LIST OF FIGURES.....	9
ABSTRACT .....	11
CHAPTER	
1 INTRODUCTION .....	13
2 METHODOLOGY .....	23
Molecular Dynamics.....	23
Density Functional Theory .....	24
Temperature Accelerated Dynamics.....	26
3 DEFECT BEHAVIOR IN URANIUM DIOXIDE .....	29
Solubility and Clustering of Ruthenium .....	29
Computational Details .....	31
Electronic Structure Calculations .....	31
Thermodynamic Calculations.....	33
Allowed Chemical Potential.....	34
Stability of Ru in UO <sub>2</sub> .....	38
Clustering Behavior of Ru.....	40
Fission Product Segregation to Grain Boundaries in UO <sub>2</sub> .....	42
Computational Details .....	43
Segregation Energy Calculations by Empirical Potentials .....	45
Effect of Charge on FP Segregation.....	47
Effect of Ionic Radius on FP Segregation.....	48
Factors that Affect FP Segregation .....	49
Discussion.....	50
Effect of Cr Doping in UO <sub>2</sub> .....	51
Computational Details .....	52
Cr Segregation to the $\Sigma 5$ Grain Boundary: DFT Confirmation .....	53
Electronic Structure at the Grain Boundary .....	55
Conclusions .....	57
4 SURFACE DIFFUSION ON SrTiO <sub>3</sub> (100).....	76
Computational Details.....	76
Results and Discussion.....	77

Diffusion Mechanism Predicted by TAD Simulations.....	77
DFT Verification.....	80
Generalization: Other Metal Adatoms .....	82
Conclusions .....	83
5 OXIDATION OF TiN (001) STEPPED SURFACE .....	91
Computational Details.....	91
Results and Discussion.....	92
Adsorption of Atomic and Molecular Oxygen.....	92
O <sub>2</sub> Dissociation.....	94
TiO <sub>2</sub> Formation .....	95
Conclusions .....	97
6 GENERAL CONCLUSIONS .....	102
APPENDIX: HOW TO CONSTRUCT GRAIN BOUNDARIES .....	105
LIST OF REFERENCES .....	113
BIOGRAPHICAL SKETCH.....	123

## LIST OF TABLES

<u>Table</u>	<u>page</u>
3-1. Defect formation energy of uranium vacancy in $\text{UO}_2$ for different $k$ -meshes .....	60
3-2. Trap site formation energies of defects in $\text{UO}_2$ .....	60
3-3. Lattice parameters of $\alpha$ -U.....	60
3-4. Defect formation energies (eV) of uranium and oxygen vacancies; it is assumed that $\text{UO}_2$ phase is maintained under O-rich conditions .....	60
3-5. The chemical potentials of Ru for different reference states .....	61
3-6. Incorporation energies of Ru at various trap-sites using different reference states; the lowest energies are denoted in bold .....	61
3-7. Solution energies of Ru at various trap-sites using different reference states; the lowest energies are denoted in bold .....	61
3-8. Solution energies of Ru dimers in various configurations using different reference states; the lowest energies are denoted in bold .....	62
3-9. Solution and Binding energies of Ru atoms in Schottky defect in $\text{UO}_2$ relative to different states .....	62
3-10. Segregation energies of fission products to both the $a$ - and $b$ -sites.....	63
3-11. Solution energies (eV) of Cr in $\text{UO}_{2+x}$ : the negative sign is indicative of Cr solubility.....	63
4-1. The diffusion mechanisms and barriers (eV) observed during TAD simulations with the Sekiguchi potential .....	85
4-2. DFT results for Sr and O adsorptions on SrO terminated STO surface compared with the empirical potential results .....	85
4-3. Effective charges of Sr and O adatoms at atop- and bridge-site on SrO terminated STO surface .....	86
4-4. DFT results for selected species on SrO terminated STO surface.....	86
5-1. Predicted adsorption energies for atomic O on the flat and stepped TiN surfaces.....	98

## LIST OF FIGURES

<u>Figure</u>	<u>page</u>
1-1. Simplified portion of the U-O phase diagram, emphasizing solid phases with compositions between $\text{UO}_2$ and $\text{UO}_3$ .....	19
1-2. Thermal conductivity (left) and the radial temperature distribution of $\text{UO}_2$ (right) ...	20
1-3. $^{235}\text{U}$ and $^{239}\text{Pu}$ fission product creation rates in FR(fast reactor) and PWR(pressurized water reactors).....	21
1-4. Cross-sectional micrographs of annealed TiN films at (a) 500, (b) 600, (c) 700, and (d) 800 °C for 2 h in air .....	22
3-1. The allowed chemical potentials in various uranium oxides .....	64
3-2. The chemical potential of Ru in $\text{UO}_2$ within the allowed oxygen chemical potential .....	65
3-3. The separated $\text{Ru}_T+\text{Ru}_U$ dimer (left) and the bound dimer (right) in $\text{UO}_2$ : Ru atoms are circled .....	66
3-4. Ru atom, dimer, and trimer in the Schottky defect in $\text{UO}_2$ (circled) .....	66
3-5. (a) DOS plots of the $\text{UO}_2$ with Ru atoms in the Schottky defect (b) DOS plot of the Ru metal and partial DOS plots of Ru atoms in the Schottky defect.....	67
3-6. $\Sigma 5$ (310)/[001] tilt grain boundary in $\text{UO}_2$ ; the half-filled uranium columns resulting from removing atoms are indicated by the dotted outlines .....	68
3-7. The energy profiles of Xe and $\text{Ru}^{4+}$ across the grain boundary; the inset images are the projections of the uranium layer of the <i>a</i> - and <i>b</i> -site.....	68
3-8. Effective charges of all oxygen ions for both Xe (open) and Ru (closed) cases; the positions of segregates are indicated with dashed lines.....	69
3-9. Segregation energies of cation fission products at <i>a</i> - and <i>b</i> -site .....	70
3-10. Segregation energy contour for the <i>a</i> -site and the <i>b</i> -site (right); blue indicates where segregation is unfavored.....	71
3-11. $\Sigma 5(310)/[001]$ tilt grain boundary of $\text{UO}_2$ : the relative energy profile of Cr obtained by empirical potentials .....	72
3-12. Cr-doped grain boundary: Cr at uranium site (left) and Cr at interstitial site (right). Cr is the small green atom .....	72
3-13. Bader charges of uranium and oxygen for $\text{Cr}_U$ (upper) and $\text{Cr}_i$ cases (lower).....	73

3-14. Bader charges of uranium and oxygen for the case that Cr is added in the bulk region .....	74
3-15. Charge density difference for $Cr_U$ (upper images) and $Cr_i$ (bottom images).....	75
4-1. (a) A model SrO-terminated STO surface (for TAD) and adsorption sites on both (b) SrO- and (c) $TiO_2$ -terminations.....	87
4-2. The mechanism for Sr migration on the SrO-terminated STO(100) surface .....	88
4-3. The mechanism for Sr migration on the $TiO_2$ -terminated STO(100) surface .....	89
4-4 O vacancy diffusion on the SrO-terminated STO surface .....	90
5-1. The TiN (001) surface with a monatomic step and the three stable adsorption sites (denoted as b, t, and e) for atomic O.....	99
5-2. Predicted adsorption energies for molecular oxygen on the stepped TiN surfaces .....	99
5-3. The differential charge density of the $O_2$ precursor at the <i>t</i> site.....	100
5-4. The lowest energy configuration of dissociated O atoms (left) and the estimated dissociation paths for $O_2$ precursor at the <i>b</i> and <i>t</i> sites (right) .....	100
5-5. $TiO_2$ formation associated with the dissociation of $O_2$ precursor at <i>t</i> site .....	101

Abstract of Dissertation Presented to the Graduate School  
of the University of Florida in Partial Fulfillment of the  
Requirements for the Degree of Doctor of Philosophy

COMPUTATIONAL INVESTIGATION OF THE DEFECT BEHAVIOR AND SURFACE  
PHENOMENA OF CERAMICS

By

Minki Hong

August 2013

Chair: Susan B. Sinnott

Major: Materials Science and Engineering

Classical atomic-scale and first principles, quantum-based computational methods are used to examine impurity behavior in  $\text{UO}_2$  and surface phenomena on  $\text{SrTiO}_3$  and  $\text{TiN}$ .

Firstly, the accommodation of fission products in  $\text{UO}_2$  fuels is investigated. In particular, the stability and clustering of Ru is examined using density functional theory in combination with classical thermodynamics. As observed in experiments, Ru is predicted to be insoluble and metallic and its aggregates are identified as the probable nucleus of metallic precipitates. For further investigation of fission product behavior especially near a  $\Sigma 5$  grain boundary, segregation energies of various fission products to the boundary are calculated using empirical potentials and their dependency on site, charge, and ionic radius is determined. These results provide insights into the way in which the microstructure of the nuclear fuel influences fission product retention, which is important for fuel design to length lifetime. Additionally, the microstructure of  $\text{UO}_2$  affects the accommodation of Cr, a common grain enlarger of  $\text{UO}_2$ . The bonding within the grain boundary is investigated using density functional theory and the results indicate that Cr prefers to reside in U substitutional sites. They further predict that Cr will

segregate to grain boundaries and form bonds with neighboring O atoms that weaken the ionic nature of adjacent U-O bonds.

Secondly, the surface diffusion mechanism of adatoms and vacancies on SrTiO<sub>3</sub> (001) is explored using temperature accelerated dynamics. Ad-species are predicted to be mobile with relatively low diffusion barriers on the SrO-terminated surface, whereas they are predicted to be largely immobile on the TiO<sub>2</sub>-terminated surface. An additional important finding is that, of the two lowest binding sites on the SrO-terminated surface, one is typically very close in energy to the saddle point.

Finally, the surface oxidation of the TiN (001) surface with a monatomic step is examined using density functional theory. The energy released during the adsorption and dissociation of O<sub>2</sub> on the stepped surface is predicted to be much larger than on the flat surface with the same orientation. Furthermore, a TiO<sub>2</sub> formation reaction associated with O<sub>2</sub> dissociation is predicted to be especially favorable at the step edge.

## CHAPTER 1 INTRODUCTION

Since the discovery of the nuclear fission of uranium by Lise Meitner and Otto Frisch in 1939, various nuclear fuels have been produced and investigated to utilize the energy associated with the fission reaction. In order to maximize the performance of nuclear generators, nuclear fuels must have several material properties: 1) sufficient geometric stability during operation, 2) satisfactory thermal stability and transport character during operation, 3) acceptable chemical compatibility with cladding materials, 4) sufficient compatibility with coolants and 5) economically acceptable manufacturing costs. Uranium dioxide ( $\text{UO}_2$ ) has good properties with respect to these criteria such as thermal stability under irradiation, good phase stability, high melting temperatures, and compatibility with possible cladding materials such as stainless steel and zircaloy. It is therefore used as the main fuel base for most nuclear reactors<sup>1</sup>.  $\text{UO}_2$  has the fluorite structure (space group  $Fm\bar{3}m$ ) with a lattice parameter of 5.47 Å. Uranium forms a closed-packed cation sublattice and, oxygen fills all tetrahedral sites to form a simple cubic sublattice.  $\text{UO}_2$  exhibits almost a single phase up to its melting point, which is 2865°C<sup>2</sup>, and this phase encompasses a broad range of stoichiometries (Figure 1-1). Its large free energy of formation (-218.2 kcal/mol at 1000°C) implies excellent chemical stability, which is the most powerful characteristic of  $\text{UO}_2$ .<sup>1</sup> However,  $\text{UO}_2$  has several limiting properties as a nuclear fuel material.

The most important of these is poor thermal conductivity (Figure 1-2), which is the source of high lateral thermal gradient, and low fracture strength in  $\text{UO}_2$ . This poor thermal conductivity leads to cracks and low heat transfer to the coolant. Recently, a computer simulation on the origin of this property was conducted; it found that the

anharmonicity of longitudinal optical phonon modes is the source of low conductivity<sup>3</sup>. During operation,  $\text{UO}_2$  undergoes two distinctive thermal conditions: 1) high operating temperatures (approaching the melting temperature,  $\sim 2800^\circ\text{C}$ ), and 2) steep thermal gradients ( $10^4^\circ\text{C}/\text{cm}$ )<sup>4</sup> between the core and the outer part in the pellet. High operating temperatures usually accompany solid-state reactions, grain growth, densification, and fission product diffusion<sup>4-6</sup>. The steep thermal gradient is the source of various undesired process such as re-distribution of important components<sup>7</sup> through atomic diffusion and thermal stress that causes plastic deformation in high temperature regions as well as cracks in low temperature regions<sup>8-10</sup>. In order to improve the thermal properties of  $\text{UO}_2$  fuels, many material modifications have been carried out, including modifying the microstructure of the fuel pellet<sup>11, 12</sup>, forming solid solutions with other refractory materials<sup>13, 14</sup>, and doping<sup>15, 16</sup>. Another important disadvantage is that  $\text{UO}_2$  can experience phase deviations, which can influence the mechanical properties of  $\text{UO}_2$  as well as its melting point and thermal conductivity. For example, the fluorite structure of  $\text{UO}_2$  is stable up to an O/U ratio of 2.25 and, eventually,  $\text{U}_4\text{O}_9$  starts to form. The higher oxides, such as  $\text{U}_3\text{O}_7$ ,  $\text{U}_3\text{O}_8$ , and  $\text{UO}_3$ , can also be formed typically under low temperature (less than  $400^\circ\text{C}$ ) conditions in the presence of water vapor and/or gamma radiation<sup>17-19</sup> (see Figure 1-1).

To overcome these demerits, achieving a comprehensive understanding of the behavior of fission products as well as dopants during the operation of nuclear reactors is essential. This entails developing an improved understanding of the nature of  $\text{UO}_2$  itself because generated fission products and dopants can drastically change its physical properties.

Fission reactions are complex, and involve the release of products and the generation of defects, such as voids and fission-gas filled bubbles, dislocations and stacking faults, which affect the structural and mechanical properties of the fuel<sup>4, 20</sup>. Thus, the knowledge of the chemical state and the migration behavior of the fission products are critical because these will influence important physical properties of the fuel, such as thermal conductivity, swelling, creep, and melting. For decades, a vast amount of work has revealed the chemical states and locations of fission products in various fuel materials (see Figure 1-3). Dopants have also been investigated in order to improve the properties of  $\text{UO}_2$ , such as electrical conductivity<sup>21</sup>, chemical stability<sup>22</sup>, fission gas release (FGR)<sup>23</sup>, and so forth. Recently, enhanced by the capability of modern computing systems, atomic level calculations and simulations of various defect structures associated with fission products and dopants in  $\text{UO}_2$  have become feasible with high-fidelity methods. These approaches are used to quantify the energetics of fission product and dopant interaction with defects in  $\text{UO}_2$ , as detailed in Chapter 3 of the dissertation.

Strontium titanate ( $\text{SrTiO}_3$ ; STO) is of considerable interest due to its uses as substrate materials for high  $T_c$  superconducting films<sup>24</sup>, high mobility oxide interfaces<sup>25, 26</sup>, and ferroelectric superlattices<sup>27</sup>. Since the performance of such heterostructures depends on the growth of atomically smooth films<sup>28</sup>, the ability to tailor the substrate surface on the atomic level is of utmost importance. Thus, many thin film growth methods have been used to create an atomically smooth STO surface, including chemical vapor deposition (CVD)<sup>29</sup>, pulsed laser deposition (PLD)<sup>30</sup>, sol-gel method<sup>31</sup>, and atomic-layer deposition (ALD)<sup>32</sup>. Generally, the growth of the epitaxial films is

governed by numerous factors, including misfit strain, chemical compatibility, and growth conditions. In particular, the surface morphology is very sensitive to surface mobility<sup>33, 34</sup>. In order to understand the atomic-level processes which occur during atomic layer deposition, SrO, TiO<sub>2</sub>, and STO thin films have been deposited utilizing molecular dynamics (MD) simulations<sup>24, 35-37</sup>. From these studies it was found that there was a significant dependence of the growth characteristics on the termination layer (SrO or TiO<sub>2</sub>) as well as the incident species, with SrO particles growing in a layer-by-layer fashion and TiO<sub>2</sub> particles producing 3D island morphology.

Thin film growth through particle deposition involves phenomena that occur at two time-scale regimes<sup>38</sup>. The first encompasses the initial non-equilibrium kinetic behavior of the incident atoms, molecules, or clusters and involves their collision with the surface and short-term relaxation. These processes typically occur in the picoseconds (ps) time range; they thus influence thin film morphology at low temperatures, but do not necessarily dominate at higher temperatures. The second relevant time-scale regime involves subsequent thermal diffusion of the deposited particles between deposition events. This diffusion occurs on a time-scale of microseconds to seconds ( $\mu$ s-s), depending on growth conditions<sup>39</sup>, and determines the final morphology of the film.

While MD investigations give insight into the growth and morphology of said thin films, the inherent limitation of classical MD method to probe nanosecond to microseconds (ns- $\mu$ s) time scale regimes precludes their use in determining the kinetically limited diffusion behavior of the depositing particles. That is, MD is typically limited to examining the first regime of growth via the deposition of the incoming

particles. At the same time, the diffusive behavior of ad-species on a surface must be characterized in order to fully understand and predict thin film growth behavior. There has therefore been considerable interest in accelerated MD (AMD)<sup>40-45</sup> methods, which can extend the time-scales considered in atomistic simulations to orders-of-magnitude greater than traditional MD, to probe these time-scales relevant for film growth<sup>46, 47</sup>. As one of the accelerated MD methods, temperature accelerated MD (TAD) is used to understand the surface diffusion behavior of ad-species on SrTiO<sub>3</sub> (001) in Chapter 4.

Titanium nitride (TiN) is used in the form of thin or thick films in applications where it is typically subjected to extreme conditions, such as wear-resistant coatings for cutting tools<sup>48</sup>, diffusion barriers for metallization on silicon-based devices<sup>49</sup>, and biocompatible and corrosion-resisting coatings for orthopedic implants and dental surgery tools<sup>50</sup>. The properties of TiN surfaces are therefore important, as are their chemical interactions with oxygen because oxidation is known to significantly modify these properties. For example, oxygen contamination can be present during the growth of TiN film by chemical vapor deposition method, which can alter the film quality<sup>51</sup>. It is known that TiN spontaneously forms a thin oxide layer when it is exposed to air, which prevents further oxidation and corrosion at temperatures under 500°C<sup>52</sup>. However, when the temperature goes over ~500°C, rapid growth of TiO<sub>2</sub> can occur, which compromises the film quality. Chen *et al.* has reported that the rutile-TiO<sub>2</sub> can be detected over 600°C and grows inward and faster with increasing temperature (see Figure 1-4)<sup>53</sup>. Many experiments agree that oxynitride layers form first on top of TiN surfaces, followed by the formation of TiO<sub>2</sub> although there is controversy regarding the pathways and mechanisms by which the TiO<sub>2</sub> layers develop<sup>51, 54, 55</sup>.

Several theoretical studies using first-principles calculations have been conducted to identify these mechanisms. For example, Piskanec *et al.* predicted barrierless O<sub>2</sub> adsorption and dissociation followed by Ti-O chain formation along the O<sub>2</sub> dissociation path<sup>50</sup>. Similar results were reported by Zimmermann *et al.*, who also predicted the formation of stable Ti vacancies beneath the initial ultrathin TiO<sub>2</sub> layers that are thought to induce nitrogen vacancy segregation<sup>56</sup>. In contrast, Graciani *et al.* predicted that an N-O exchange process was the preferred mechanism and provided a nitrogen exit channel that encouraged further oxidation of TiN rather than the direct formation of TiO<sub>2</sub> layers<sup>57</sup>. Despite some disagreements, all three of these studies agreed that the endothermic O<sub>2</sub> dissociation is the key reaction that is necessary to provide the energy needed for further oxidation and Ti-N dissociation. A key limitation of all three was that the modeled surfaces were both flat and pristine, while it is well-established that surface defects are essential components for many surface reactions<sup>58-62</sup>. In particular, steps on metal<sup>63, 64</sup> as well as ceramic<sup>65, 66</sup> surfaces have been identified as reactive sites for molecular reactions, such as for O<sub>2</sub> dissociation<sup>67-69</sup>. Therefore O<sub>2</sub> adsorption and dissociation on the stepped TiN (001) surface is investigated and a TiO<sub>2</sub> formation path is predicted in Chapter 5.

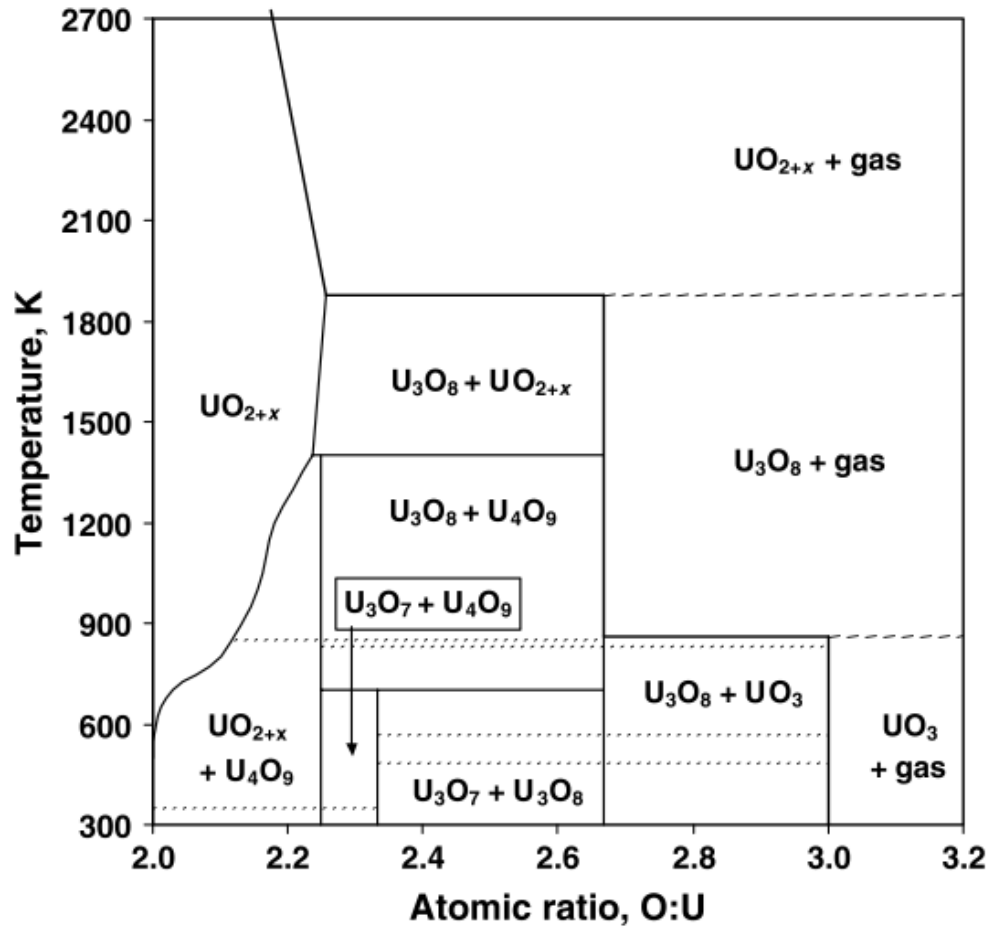


Figure 1-1. Simplified portion of the U-O phase diagram, emphasizing solid phases with compositions between  $UO_2$  and  $UO_3$ <sup>70</sup>

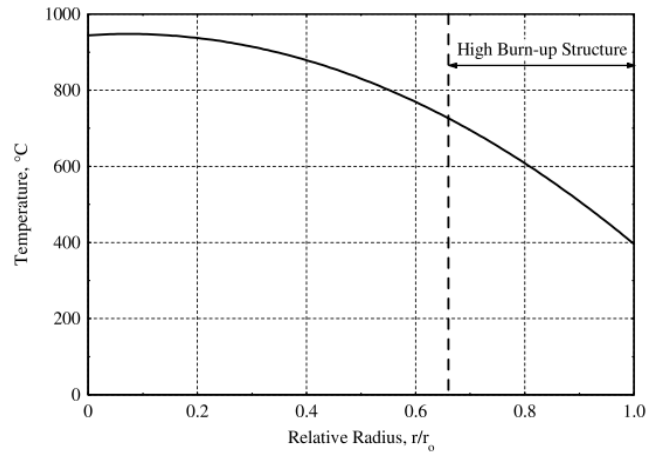
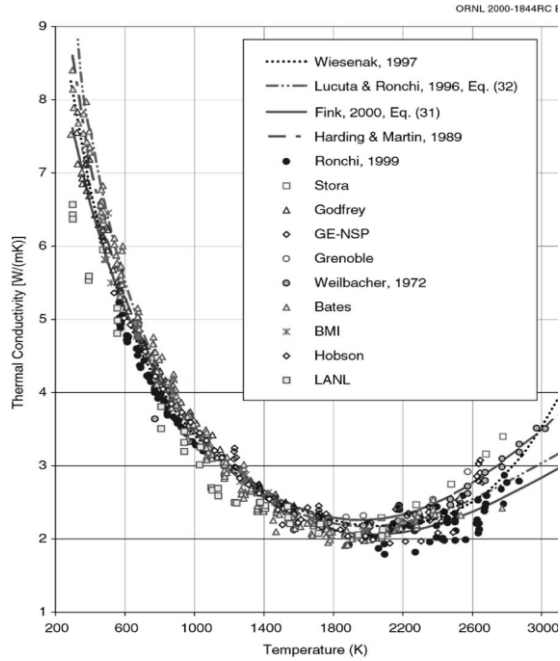


Figure 1-2. Thermal conductivity<sup>71</sup> (left) and the radial temperature distribution of UO<sub>2</sub><sup>72</sup> (right)

Type	Element	PWR UO <sub>2</sub> <sup>235</sup> U fission (mass %)	PWR MOX <sup>239</sup> Pu fission (mass %)	FR Pu fission (at./fission)
RARE GASES	Xe	12.7	13.3	0.232
	Kr	1.1	0.6	0.020
METALLIC INCLUSIONS	Ru	6.9	8.9	0.218
	Pd	3.6	7.3	0.124
	Rh	1.2	2.2	0.059
	Tc	2.3	2.4	0.057
	Ag	0.3	0.6	0.013
	Cd	0.2	0.5	0.006
	Sn	0.2	0.2	0.006
	Mo	9.6	9.0	0.215
OXIDE INCLUSIONS	Ba	4.4	4.2	0.066
	Sr	2.6	1.3	0.040
	Zr	10.4	7.4	0.197
IN SOLUTION IN THE OXIDE	Y	1.4	0.7	0.022
	Ce	7.7	6.9	0.126
	Nd	11.1	9.8	0.149
	La	3.5	3.4	
	Pr	3.2	3.0	
	Pm	0.4	0.5	0.172
	Sm	2.0	2.4	
	Eu	0.5	0.7	
	Gd	0.2	0.3	
« VOLATILES »	Cs	11.0	11.4	0.203
	Rb	1.0	0.5	0.018
	Te	1.4	1.6	0.031
	I	0.6	0.8	0.018

Figure 1-3. <sup>235</sup>U and <sup>239</sup>Pu fission product creation rates in FR(fast reactor) and PWR(pressurized water reactors)<sup>73</sup>

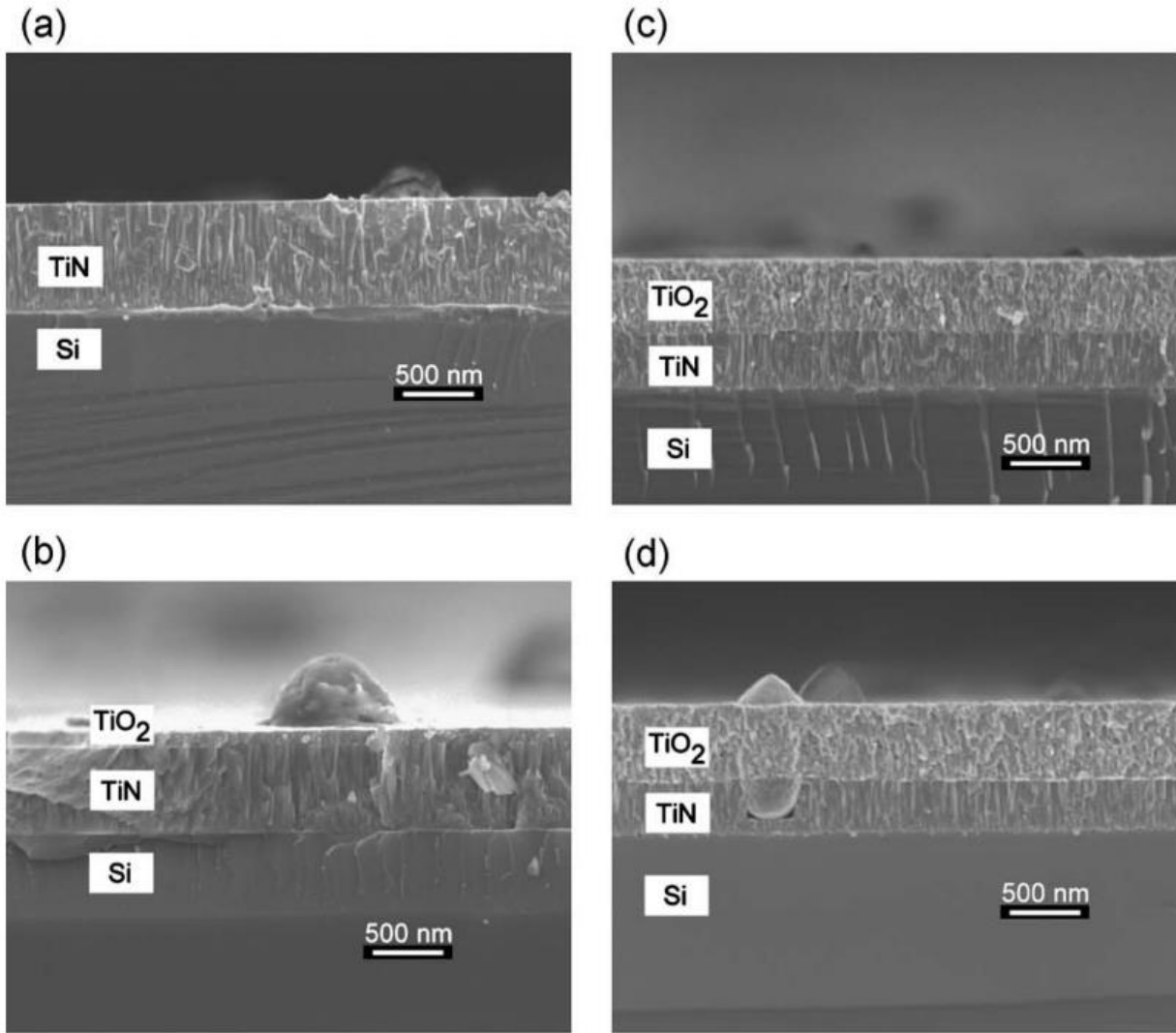


Figure 1-4. Cross-sectional micrographs of annealed TiN films at (a) 500, (b) 600, (c) 700, and (d) 800 °C for 2 h in air (adapted from Fig.4 in the ref<sup>53</sup>)

## CHAPTER 2 METHODOLOGY

Classical molecular dynamics (MD) simulations<sup>74</sup> and density functional theory (DFT) calculations<sup>75</sup> are the main computational tools used in this work. The details of these approaches are now presented.

### **Molecular Dynamics**

Molecular dynamics (MD) simulation is a computing technique for classical many-body systems based on the positions and momenta of particles in the system. The atomic movement is determined by solving Newton's equations of motion from the calculated total energy, which is given as:

$$\vec{F}_i = m_i \frac{d^2 \vec{r}_i}{dt^2} = - \frac{\partial E}{\partial \vec{r}_i} \quad (2-1)$$

where  $\vec{F}_i$  is the force vector,  $m_i$  is the mass and  $\vec{r}_i$  the position vector of atom  $i$ ;  $t$  is time and  $E$  is the total energy. The equation of motion is integrated with finite different methods<sup>74</sup>. There are many algorithms for solving the equation of motion including the Verlet, leap frog, and gear predictor-corrector algorithms. A fifth-order Gear predictor-corrector algorithm is used for this work because it is well known to be good for minimizing fluctuations in energy<sup>76</sup>.

The interactions between ions in a certain lattice are composed of two terms: (1) long-range Coulombic interactions, and (2) short range interactions. The Ewald method<sup>77</sup> is used for summation of the long range interactions, and parameterized pair potentials are used for modeling the short range interactions, which is described by the Buckingham pair potential<sup>78</sup>. The lattice energy is then given by:

$$U_L = \frac{1}{4\pi\epsilon_0} \sum_{i \neq j} \frac{q_i q_j}{r_{ij}} + A e^{-r_{ij}/\rho} - \frac{C}{r_{ij}^6} \quad (2-2)$$

where  $\mathbf{A}$ ,  $\rho$ , and  $\mathbf{C}$  are the adjustable parameters for ions  $i$  and  $j$ , and  $r_{ij}$  is the interionic distance and  $q$  is the charge of each ion.

### Density Functional Theory

DFT is a quantum mechanical based theory used to investigate the electronic structure of a many-body system. With this theory, the properties of many-body systems can be determined by a functional, i.e. functions of another function, which in this case is the ground state charge density. In order to obtain a better comprehension of DFT, it is essential to understand why it was developed and its relative merits and demerits.

Theoretically, all the material properties can be described by solving many-body Schrödinger's equation, which is given as:

$$\left\{ \sum_{i=1,N} \left[ -\frac{1}{2} \nabla_i^2 + \sum_R \frac{Z_R}{|r_i - R|} \right] + \sum_{i1,i2=1,N} \frac{1}{|r_{i1} - r_{i2}|} \right\} \Psi(r_1, \dots, r_N) = E \Psi(r_1, \dots, r_N) \quad (2-3)$$

where  $\Psi$  is the many-body wavefunction,  $N$  the number of particles in the system. What this equation implies is we need  $M^N$  data points where  $M$  is the number of grid points for the space in which the system resides. Consequently there have been lots of attempts to reduce computational load by approximating  $\Psi$  with single particle wavefunctions,  $\psi(r)$ . DFT is one of the most successful attempts. In equation (2-3), the ground state many-body wavefunction is a functional of the external potential,  $V(r)$ :

$$V(r) = \sum_R \frac{Z_R}{|r - R|} \quad (2-4)$$

The essential part of DFT is that the external potential,  $V(r)$ , can be thought as a functional of the ground state charge density,  $\rho$ :

$$\rho[r] = n \int dr_1 dr_2 dr_3 \dots dr_{n-1} |\Psi(r, r_1, r_2, r_3, \dots, r_{n-1})|^2 \quad (2-5)$$

As a result, every electronic property of the system is a functional of  $\rho$ , and subsequently all the other energy including Coulomb and the exchange-correlation energy among electrons can be accurately approximated by  $\rho$ , except the kinetic energy. In order to include the kinetic energy, the true many-body wavefunction kinetic energy is replaced with that of single particle - which is not interacting with any other particle. Finally, equation (2-3) can be rewritten as the so-called Kohn-Sham single particle equation<sup>79</sup>.

$$\left\{ -\frac{1}{2} \nabla^2 + V(r)[\rho] \right\} \Psi_i(r) = E_i \Psi_i(r) \quad (2-6)$$

The Kohn-Sham total energy functional can be written as

$$E_v[\rho] = \int dr V(r) \rho(r) + \frac{1}{2} \int dr dr' \frac{\rho(r) \rho(r')}{|r - r'|} + 2 \times \sum_i \left\langle \Psi_i \left| -\frac{\nabla^2}{2} \right| \Psi_i \right\rangle + E_{xc}[\rho] \quad (2-7)$$

The first term on the right hand side represents the interaction between the electrons and the external potential,  $V(r)$ . The second term is the Coulomb energy of density distribution. The third is the single particle kinetic energy of the non-interacting electrons. These three terms can be described without approximation, i.e., can be “exact”. However, the last term,  $E_{xc}[\rho]$ , is the exchange-correlation energy functional, for which the true, non-approximate form is unknown. Therefore, the way in which the  $E_{xc}[\rho]$  is approximated is key to implementing this theory in practical. We can define the  $E_{xc}[\rho]$  as:

$$E_{xc}[\rho] = \int dr \rho(r) \varepsilon_{xc}(r) \quad (2-8)$$

This equation implies that  $E_{xc}[\rho]$  has non-local characteristic. One possible way to approximate  $E_{xc}[\rho]$  is to assume that it is a functional of local electron density. This approach is called the local density approximation (LDA)<sup>79</sup>.

$$\varepsilon_{xc}^{LDA}(r) = \varepsilon_{xc}^{LDA}(\rho(r)) \quad (2-9)$$

LDA has been successfully applied to many systems. However, LDA is not applicable for excited states and usually overestimates the cohesive energy between atoms. To overcome the later limitation, the generalized gradient approximation (GGA)<sup>80</sup> was introduced. In this approach, the  $E_{xc}[\rho]$  depends on not only the local density  $\rho(r)$  but also the local density gradient  $\nabla\rho(r)$ .

$$E_{xc}^{GGA}[\rho] = \int dr \rho(r) \varepsilon_{xc}^{GGA}(\rho(r), \nabla\rho(r)) \quad (2-10)$$

In general, GGA improves the cohesive energy estimation and the corresponding bond length is slightly overestimated while it is usually underestimated by LDA.

The DFT software that is used in the work reported here is the Vienna Ab-Initio Simulation Package (VASP)<sup>81, 82</sup>. Pseudo-potentials and a plane-wave basis set is used and the interaction between ions and electrons is described using the projector augmented wave method (PAW)<sup>83</sup> for all the DFT calculations in following chapters.

### **Temperature Accelerated Dynamics**

TAD takes advantage of the fact that the rate of thermally activated processes is naturally greater at higher temperatures in order to accelerate the rate of system evolution, while still preserving the correct order of transitions at some lower temperature of interest. The basic event examined during a TAD simulation is the transition from one state to another connected by a minimum energy pathway (MEP). This pathway contains a transition state at a maximum along the MEP – the saddle

point configuration. The TAD approach utilizes basin-constrained MD (BCMD), which confines the trajectory to a particular potential energy basin – or state – of the potential energy surface of the system. This BCMD is performed at a high temperature  $T_{\text{high}}$ , which is much higher than the temperature of interest,  $T_{\text{low}}$ . If the system attempts to leave the basin during the BCMD, its trajectory is reflected back to the original state and the time of the attempted escape is documented creating a list of ‘waiting times’ of attempted escapes<sup>44</sup>. The barrier for each attempted event is also calculated using the nudged elastic band (NEB) method<sup>84</sup>. As described below, the barrier for each event is used to extrapolate the waiting times of events at  $T_{\text{high}}$  to  $T_{\text{low}}$ .

TAD has three main assumptions: events of interest are infrequent or rare, harmonic transition state theory is applicable for the system of interest, and a lower bound on the rate prefactors is known ( $v_{\text{min}}$ ). Further, the algorithm also requires a predefined confidence level  $\delta$  for the simulation; for this study,  $\delta=0.05$  and  $v_{\text{min}}= 1 \times 10^{12} \text{ s}^{-1}$ .

Infrequent event systems are characterized by well-defined transitions between them<sup>45</sup>. Since harmonic transition state theory is assumed, an Arrhenius expression for the rate constant going from state A to B,  $k_{A-B}$ , can be derived<sup>44</sup>:

$$k_{A-B} = v_0 \exp\left(-\frac{1}{k_B T} E_a\right) \quad (2-11)$$

where  $E_a$  is the energy barrier between the saddle point configuration and the minimum configuration (State A) and  $v_0$  is a pre-exponential factor calculated using the Vineyard formula<sup>85</sup>:

$$v_0 = \frac{\prod_{i=1}^{3N} v_i}{\prod_{j=1}^{3N-1} v_j} \quad (2-12)$$

Here,  $v_i$  is the set of vibrational frequencies at the minimum (State A) and  $v_j$  are the set of real frequencies at the saddle point configuration<sup>86</sup>. This relationship follows directly from the assumption that the potential is harmonic, i.e., that the potential at both the minimum and saddle configurations can be approximated by a harmonic oscillator. It is a measure of the width of the harmonic oscillators at the saddle versus the minimum that captures the difference in vibrational entropy between the two. By assuming a minimum prefactor, the computational cost associated with calculating  $v_0$  is avoided in TAD.

Using the energy barrier between the initial state and saddle configuration, each event time observed at  $T_{high}$  ( $t_{high}$ ) is extrapolated to corresponding waiting times at  $T_{low}$  ( $t_{low}$ ), by:

$$t_{low} = t_{high} \exp\left(E_a \left( \frac{1}{k_B T_{low}} - \frac{1}{k_B T_{high}} \right)\right) \quad (2-13)$$

The BCMD is continued at  $T_{high}$  until a stopping criterion  $t_{high,stop}$ , which depends on  $v_{min}$  and  $\delta$ , is met (equation (2-14)). At that point, the event with the lowest time at  $T_{low}$  is accepted, the system placed in the corresponding state, and the procedure repeated.

$$t_{high,stop} \equiv \frac{\ln\left(\frac{1}{\delta}\right)}{v_{min}} \left( \frac{v_{min} t_{low,stop}}{\ln\left(\frac{1}{\delta}\right)} \right)^{\frac{T_{low}}{T_{high}}} \quad (2-14)$$

## CHAPTER 3 DEFECT BEHAVIOR IN URANIUM DIOXIDE

In this chapter, the solution and clustering of a selected fission element, ruthenium (Ru), and the segregation of various fission species to a grain boundary in  $\text{UO}_2$  is investigated using several computational methods. Additionally, the electronic structure near the  $\text{UO}_2$  grain boundary with a typical grain enlarger, chromium (Cr), is examined in order to provide some practical insights for manufacturing  $\text{UO}_2$  pellet as the nuclear fuel.

### **Solubility and Clustering of Ruthenium**

Fission reactions in a nuclear fuel are complex, as they involve the release of products and the generation of defects, such as voids and fission-gas filled bubbles, and lead to the generation of dislocations and stacking faults, which affect the structural and mechanical properties of the fuel material<sup>4, 20</sup>. Therefore, the chemical stability of fission products (FPs) in  $\text{UO}_2$  based nuclear fuels is critical to both the performance and the integrity of the fuel. There is, therefore, tremendous interest in understanding the microscopic behavior of FPs under the operating conditions of the fuel, including high temperature and irradiation. For decades, atomic scale calculation and simulation methods have been used to quantify this chemical stability<sup>87-89</sup>. A typical starting point is the calculation of the solution energy of fission products as point defects in the  $\text{UO}_2$  matrix<sup>89</sup>. Among the various computational approaches that can be used to calculate these energies, density functional theory (DFT) is one of the most widely employed today because of its ability to produce relatively high-fidelity results for both a wide range of fission products and for  $\text{UO}_2$ , as well as to account for the complexities associated with different bonding environments within one system. However, the conditions of typical DFT calculations (zero Kelvin and perfect vacuum) are inconsistent

with the conditions in actual reactors (high temperatures and oxygen partial pressures). An approach that addresses this limitation while retaining the strengths of the DFT approach is to combine the results of DFT calculations with thermodynamics calculations<sup>90-93</sup>.

In the past, DFT calculations have most commonly been applied to examine the accommodation of fission products as point defects, which is most relevant to the very earliest stages of fission product formation and accommodation. An improved description of fission product formation and incorporation over longer times, however, requires consideration of more complicated defect structures, such as fission product clusters, bubbles, inclusions, and precipitates. These types of extended defects have been most commonly examined using less computationally intensive empirical methods than DFT, which limits the types of aggregates that can be studied<sup>94, 95</sup>. Recently, however, it becomes possible to apply DFT to examine small-scale defect clusters in  $\text{UO}_2$  that may form the nuclei of larger fission product aggregates.

The solution energy of Kr, a gaseous fission product which has high yield, was among the first to be considered in DFT calculations<sup>96</sup>. The resulting energies at several intrinsic defects predicted that Kr is insoluble in  $\text{UO}_2$ , in agreement with experimental findings<sup>20</sup> and pair potential calculations<sup>89, 97</sup>. This insolubility was also predicted by a subsequent computational study<sup>98</sup> which presented the dependence of the solubility of fission products on the thermodynamic conditions of the fuel such as stoichiometry, defect concentration, and temperature. In addition, over the last decade, the chemical stability of various fission products that exist in gaseous or oxide form in  $\text{UO}_2$  – including He, I, Cs, Sr, Ba, Zr, Mo, and Xe – have been determined using DFT<sup>98-102</sup>. More

recently, the stabilities of selected metallic fission products were also examined<sup>103</sup>. In most cases these studies focused on a single fission product atom and its solution or oxide formation at trap sites, the stabilities of which were also evaluated using DFT<sup>104-108</sup>. Because these studies focused on individual FPs within the UO<sub>2</sub> host, the FP was typically in an oxidized state, and not representative of metallic precipitation.

Here, the focus is on the solubility of metallic Ru fission products, examined using a combination of DFT and classical thermodynamics in a manner similar to that taken in Refs<sup>91, 92, 109, 110</sup>. Ru can typically be found in the form of metallic (or “white”) inclusions within the fuel, normally an alloy of metallic FPs: Ru, Mo, Pd, Rh, Tc and Te<sup>20</sup>. There is little information, however, about the atomic scale accommodation of these metallic fission products and their influence on fuel performance. We first consider the chemical stability of various Ru complexes of different sizes to quantify how the very initial stages of metallic fission product clustering influences solution energies and the electronic structure of the fuel.

## **Computational Details**

### **Electronic Structure Calculations**

The DFT calculations for total energies are carried out with the valence electrons considered are as follows: U  $6s^2 6p^6 5f^3 6d^1 7s^2$ , O  $2s^2 2p^4$ , and Ru  $4s^1 3d^7$ . The outermost core radii are 2.80, 1.52, and 2.60 in a.u. for U, O, and Ru, respectively. Slight overlaps are found only for Ru-O bonds in Ru cluster systems, as discussed later. These overlaps are less than those that occur in ruthenium oxides using the same core radii and for which PAW calculations provide good agreement with experiment<sup>111, 112</sup>. Thus the effect of overlap is expected to be negligible. While in most cases the LDA and the GGA to the exchange and correlation energies within DFT provide reasonably accurate

descriptions of the electronic structure of most materials, it is now established that these approximations have difficulties in describing the ground-state behavior of highly correlated materials, including actinide oxides<sup>113</sup>. The suggested reason for this shortcoming is the partial filling of the  $5f$  orbitals and the resulting strong correlation, which means that electrons tend to be localized rather than dispersed over the entire system<sup>114</sup>. As a result, DFT calculations using the LDA or GGA, which delocalize electrons too strongly, incorrectly predict that insulating  $\text{UO}_2$  is metallic. Several attempts have been made to address this shortcoming including the Hubbard+ $U$  approach<sup>115-117</sup>, self-interaction correction (SIC)<sup>118</sup>, and hybrid functionals for exchange and correlation<sup>119</sup>. Here, we use the GGA+ $U$  framework to capture the strong correlated nature of the  $5f$  electrons of uranium. The  $U_{\text{eff}}$  ( $U$ - $J$ ) value is chosen as 3.96 eV, as was the case in other studies<sup>102, 104, 107, 120</sup>. Recently, metastable states of pure  $\text{UO}_2$  have been explored by modifying occupation matrices<sup>121, 122</sup>. However, it has been established that the degeneracy associated with metastable states is broken in systems with low symmetry, such as the defect configurations studied here. Therefore metastable states are unlikely and their exploration is left for future work.

To model the bulk  $\text{UO}_2$  system we use a  $2\times 2\times 2$  supercell with 96 atoms for the structural optimizations, and the cell volume is kept constant during the determination of Ru atomic, dimer, and trimer solution energies in order to better mimic their incorporation within an actual extended  $\text{UO}_2$  lattice. This is admittedly a small supercell and thus it is necessary to check that our results are converged against Brillouin zone sampling. For all of the calculations reported here we sample the Brillouin zone with a  $2\times 2\times 2$  Monkhorst–Pack  $k$ -point mesh<sup>123</sup>. We considered the effect of  $k$ -mesh density on

the defect formation energy in  $\text{UO}_2$  in a manner that is similar to a previous study<sup>124</sup>; the results are given in Table 3-1. We also implemented a similar  $k$ -mesh test for the Ru- $\text{UO}_2$  system that is discussed in the next section and confirmed that the difference in solution energy between  $2 \times 2 \times 2$  and  $4 \times 4 \times 4$  sampling was in the range of sub-meV. This indicates that a  $2 \times 2 \times 2$  mesh is sufficient to avoid significant numerical errors in the calculations. The cutoff energy for the plane-waves is 400 eV for all the calculations reported here. The convergence criteria for the energy difference is  $10^{-5}$  eV and for the residual forces less than  $10^{-2}$  eV/Å.

### Thermodynamic Calculations

The solution energy  $E_{\text{solution}}$  of a fission product is defined as<sup>89</sup>

$$E_{\text{solution}} = E_{\text{inc}} + E_{\text{trap}}, \quad (3-1)$$

where  $E_{\text{inc}}$  is the incorporation energy of a given fission product at a pre-existed trap site, and  $E_{\text{trap}}$  is the trap site formation energy, the energy required to form the trap site for the incorporation of the fission product. Detailed definitions of these energies are discussed elsewhere<sup>102</sup>. We can calculate the incorporation energy using total energies from DFT calculations as:

$$E_{\text{inc}} = E^{\text{total}}(i) - E^{\text{total}}(\text{trap site}) - E_i. \quad (3-2)$$

where  $E^{\text{total}}(i)$  is the total energy of the system with a fission product  $i$  at a specific trap site,  $E^{\text{total}}(\text{trap site})$  is the total energy of the system with the trap site only, and  $E_i$  is the total energy of a single atom  $i$ , i.e., the chemical potential of  $i$ ; this is discussed in detail in following section. Because the incorporation energy applies to a situation where the trap sites already exist in the fuel and that they greatly outnumber the fission products generated, the actual fuel condition after a certain amount of burn up is not accounted

for properly. In other words, the concentration of a given trap site within the fuel, which is a function of a variety of experimental factors including burn-up, temperature, and stoichiometry of the fuel, can then be used to calculate the solution energy for arbitrary conditions. Therefore, the energy needed to form trap sites is determined by combining the results of DFT with classical thermodynamics calculations. A common approach for considering thermodynamics is to use the point defect model (PDM)<sup>109, 125</sup> to evaluate the effect of fuel stoichiometry and temperature on the trap site formation energy, which can be expressed as:

$$E_{trap} = -kT \ln([x]). \quad (3-3)$$

Here  $[X]$  is the concentration of the defect considered and is found by solving self-consistently the coupled reactions for all of the relevant defects in the material. Analytical expressions for  $E_{trap}$  for various trap sites within the low temperature limit where only one trap site dominates the incorporation of a given fission product can be derived and are tabulated in Table 3-2<sup>87, 101</sup>. They can be seen to depend on the deviation of the fuel from stoichiometry ( $x$ ), the formation energies of oxygen Frenkel pairs ( $E_{FPO}$ ) and Schottky defects ( $E_{Sch}$ ), and the binding energies of divacancies and trivacancies ( $B_{DV}, B_{Sch}$ )<sup>89, 99</sup>.

### **Allowed Chemical Potential**

To calculate the energies discussed in the last section, the energy of a single atom must be defined. One of the most commonly used ways of doing this is to take an isolated atom which is infinitely far from the system as a reference. Under those conditions, the total energy of a single atom is calculated by the self-interaction energy of DFT. An alternative approach is to use the atom in its standard state as the reference

instead of the isolated atom. In this case, the total energy of a single atom is defined as the energy per atom in each of the reference systems. These different approaches essentially define different chemical potentials for the relevant species. For  $\text{UO}_2$ , we use the later approach, taking the reference state of oxygen as an oxygen molecule ( $\text{O}_2$ ) in the gas phase and the reference state of uranium as bulk metal ( $\alpha\text{-U}$ ). For the fission product (Ru), both approaches are considered to determine the single atom energy (see details in following section). The GGA+ $U$  approach is used because of its ability to reproduce the electronic structure of  $\text{UO}_2$ . However, while GGA+ $U$  does not accurately describe the structure of  $\alpha\text{-U}$  (see Table 3-3) due to the weak electron correlations present in the metal<sup>126</sup>, we nevertheless apply the + $U$  scheme to  $\alpha\text{-U}$  in order to maintain consistency with the calculations for the  $\text{UO}_2$  system; this constraint does not alter the energetic trends. We note that + $U$  still predicts  $\alpha\text{-U}$  to be metallic.

The total internal energy at zero temperature calculated in DFT does not include zero-point vibrations. Therefore, the chemical potential of an atom can be written as

$$\mu(T, P) = E^{total} + \Delta\mu(T, P), \quad (3-4)$$

where  $E^{total}$  is the total energy of the atom and  $\Delta\mu(T, P)$  includes the zero-point vibrational energy and the temperature and pressure dependence of the chemical potential<sup>105, 127</sup>. This term can be simplified by neglecting the zero-point vibrations and the pressure effects. These are reasonable approximations, particularly for defect energy calculations at zero temperature<sup>92, 127</sup>. The resulting chemical potential of an atom is thus its energy as calculated by DFT according to:

$$\mu(T = 0) \approx E^{total}. \quad (3-5)$$

Thus the chemical potentials of uranium and oxygen are related by the Gibbs free energy of UO<sub>2</sub> bulk:

$$\mu_{U[UO_2]} + 2\mu_{O[UO_2]} = g_{UO_2}^{bulk} \approx E_{UO_2}^{total} \quad (3-6)$$

where  $g^{bulk}$  is the Gibbs free energy per formula unit and  $E^{total}$  is the total energy.

Equation (3-6) applies at equilibrium thus if one of these chemical potentials becomes very low, the oxide would decompose into  $\alpha$ -U and oxygen molecules, which are the reference states used for each element. To maintain the oxide form, therefore, the range of chemical potentials is limited. For example, when  $\alpha$ -U starts to form as a result of decomposition, its chemical potential reaches a maximum, which is the chemical potential at the reference state:

$$\mu_{U[UO_2]}^{max} = \mu_{U[\alpha-U]} \approx E_{\alpha-U}^{total} \quad (3-7)$$

This is called the “uranium-rich limit” of the system and the calculated  $E_{\alpha-U}^{total}$  using GGA+ $U$  is -8.08 eV. Together with equation (3-6), the minimum of the oxygen chemical potential in UO<sub>2</sub> can be set as:

$$\mu_{O[UO_2]}^{min} = \frac{1}{2} [g_{UO_2}^{bulk} - \mu_{U[UO_2]}^{max}] = \frac{1}{2} [g_{UO_2}^{bulk} - \mu_{U[\alpha-U]}] \approx \frac{1}{2} [E_{UO_2}^{total} - E_{\alpha-U}^{total}] \quad (3-8)$$

Similarly we can obtain the maximum of the oxygen chemical potential, which we denote the “oxygen-rich limit”:

$$\mu_{O[UO_2]}^{max} = \mu_{O[O_2]} \approx \frac{1}{2} E_{O_2}^{total} \quad (3-9)$$

where the calculated  $\frac{1}{2} E_{O_2}^{total}$  is -4.89 eV.

Using these upper and lower bounds of oxygen chemical potential, we can set a range of allowed oxygen chemical potentials as originally suggested by Reuter *et al.* for the RuO<sub>2</sub> system<sup>92</sup> and applied to UO<sub>2</sub> by Yu *et al.*<sup>128</sup>:

$$\mu_{O[UO_2]}^{\min} < \mu_{O[UO_2]} < \mu_{O[UO_2]}^{\max},$$

$$\frac{1}{2} \left[ g_{UO_2}^{bulk} - \mu_{U[\alpha-U]} \right] < \mu_{O[UO_2]} < \mu_{O[O_2]}, \quad (3-10)$$

$$\frac{1}{2} \left[ E_{UO_2}^{total} - E_{\alpha-U}^{total} \right] \lesssim \mu_{O[UO_2]} \lesssim \frac{1}{2} E_{O_2}^{total}.$$

Although UO<sub>2</sub> is the dominant phase in the actual fuel, highly oxidized phases such as U<sub>3</sub>O<sub>8</sub> and UO<sub>3</sub> begin to form as the burn-up proceeds and an anion-excess condition consequently develops. Thus, we can set equilibriums similar to the equation (3-6) for these phases:

$$3\mu_{U[U_3O_8]} + 8\mu_{O[U_3O_8]} = g_{U_3O_8}^{bulk} \approx E_{U_3O_8}^{total}, \quad (3-11)$$

$$\mu_{U[UO_3]} + 3\mu_{O[UO_3]} = g_{UO_3}^{bulk} \approx E_{UO_3}^{total}. \quad (3-12)$$

By assuming the allowed range in the chemical potential for oxygen in UO<sub>2</sub> as a global bound over all phases, the uranium chemical potential range, which varies with the phase considered, can be determined as shown in Figure 3-1. The oxide with lowest uranium chemical potential varies from UO<sub>2</sub> to UO<sub>3</sub> within this oxygen potential range and this may imply the gradual transition to highly oxidized phases as the oxygen chemical potential increases even though these phases are only available near the oxygen-rich limit. This phase variation corresponds well with the experimental phase diagram of UO<sub>2</sub>, which shows a very narrow region of UO<sub>2-x</sub> while a wide variety of UO<sub>2+x</sub> is present. Thus, the chemical potential of each atom must be carefully chosen

with regard to both environmental conditions and possible phases in order to determine energies related to defects in  $\text{UO}_2$ . The defect formation energies of U and O vacancies using different chemical potentials are given in Table 3-4 to illustrate this point.

### Stability of Ru in $\text{UO}_2$

Determining the chemical potential of Ru,  $\mu_{\text{Ru}}$ , is more complicated than determining  $\mu_{\text{U}}$  and  $\mu_{\text{O}}$ . This is because during the fission reaction, Ru is generated as a single atom with high kinetic energy and is eventually incorporated into  $\text{UO}_2$  along with defects produced during the collision or other fission products around it. Therefore we might need to apply different  $\mu_{\text{Ru}}$  depending of the form Ru takes within the matrix (atomic clusters, compounds, oxides, and so on). The easiest approach is to use either gas phase or bulk metal for all case and so we take both references into account for all calculations. The chemical potentials of Ru under different reference states are presented in Table 3-5. For a better assessment of the chemical potential of Ru, however, we may need to consider other possible phases in which Ru can reside in  $\text{UO}_2$  rather than Ru metal, such as U-Ru compounds and ruthenium oxides. To enable this, we can expand the allowed chemical potential scheme for  $\text{UO}_2$  to these various fission products and thus correlate  $\mu_{\text{Ru}}$  with  $\mu_{\text{U}}$  and  $\mu_{\text{O}}$ . Here, several compounds and oxides are taken into account via their equilibrium equations:

$$2\mu_{\text{U}[\text{U}_2\text{Ru}]} + \mu_{\text{Ru}[\text{U}_2\text{Ru}]} = g_{\text{U}_2\text{Ru}}^{\text{bulk}} \approx E_{\text{U}_2\text{Ru}}^{\text{total}} \quad (3-13)$$

$$\mu_{\text{U}[\text{URu}_3]} + 3\mu_{\text{Ru}[\text{URu}_3]} = g_{\text{URu}_3}^{\text{bulk}} \approx E_{\text{URu}_3}^{\text{total}} \quad (3-14)$$

$$\mu_{\text{Ru}[\text{RuO}_2]} + 2\mu_{\text{O}[\text{RuO}_2]} = g_{\text{RuO}_2}^{\text{bulk}} \approx E_{\text{RuO}_2}^{\text{total}} \quad (3-15)$$

$$\mu_{Ru[RuO_4]} + 4\mu_{O[RuO_4]} = g_{RuO_4}^{bulk} \approx E_{RuO_4}^{total} \quad (3-16)$$

The maximum of  $\mu_{Ru}$  is the total energy per atom of Ru, which is -9.20 eV (see Table 3-5). By using this maximum and the equations above, we can obtain the possible chemical potential range of Ru in  $UO_2$  within the allowed range of oxygen discussed in the last section (see Figure 3-2). Note that  $\mu_{Ru}$  already reaches its maximum over a wide range of  $\mu_O$  and this is consistent with the fact that Ru mostly exists as metallic inclusions in  $UO_2$ .  $\mu_{Ru}$  can be considerably reduced by forming oxides; however,  $RuO_x$  is only stable in  $UO_2$  at very high  $\mu_O$  as shown in Figure 3-2 and elsewhere<sup>103, 129</sup>.

Therefore, we can reasonably presume that Ru exists in a metallic form rather than a compound or oxide in  $UO_2$  unless the oxygen chemical potential reaches both limits. Hence, it seems reasonable to expect the metal bulk to be the appropriate reference state of Ru in  $UO_2$ , even though the actual Ru may not have the metallic properties. However, for completeness, both reference states are considered for comparison.

The incorporation energies of Ru at various trap sites are presented in Table 3-6 using the reference states given in Table 3-5. Using isolated Ru atom as the reference, the results indicate that Ru incorporates into  $UO_2$  at all trap sites considered. However, as the reference state is adjusted to the bulk metal, the signs of the incorporation energies become positive. Regardless of the reference state, the U vacancy is the most energetically favorable trap-site for Ru incorporation, as it is for several other fission products<sup>102, 103</sup>.

The calculated solution energies of Ru are given in Table 3-7. Trap-site formation energies are determined using PDM at 0K (as described in Table 3-2). The

stoichiometric deviation is fixed at 0.02 which is within the stoichiometry range where oxygen clustering is negligible, consistent with the assumptions of PDM<sup>108, 130</sup>. The trend for solution energies with respect to reference states is quite similar to that of incorporation energies. If we choose the isolated atom as the reference, the Ru atoms are soluble in  $\text{UO}_{2\pm x}$  for most cases. On the other hand, using the bulk metal as the reference indicates that Ru is insoluble in  $\text{UO}_{2\pm x}$  unless the Ru is trapped at a U vacancy in  $\text{UO}_{2+x}$ . These quantities were also calculated by Brillant *et al.*<sup>103</sup> and Busker *et al.*<sup>131</sup> using DFT and empirical potentials respectively; their results are given in Table 3-7 for comparison. The calculation criteria Brillant used are different from ours and the empirical potential inherently lacks the capability of calculating single atom energy with proper reference state thus the magnitude of the solution energies from both the DFT and the empirical potentials is quite different. However, the physical trends are similar to each other (as has been shown to the case for other comparisons of FP solution energy between DFT and pair potentials<sup>102</sup>).

### **Clustering Behavior of Ru**

In the previous section, we focused on the solution of individual Ru atoms within  $\text{UO}_2$ . In the actual fuel, Ru tends to form metallic clusters in the  $\text{UO}_2$  pellet rather than exist as dispersed atoms<sup>20</sup>. Therefore, understanding the clustering behavior of Ru atoms in  $\text{UO}_2$  is important for achieving improved predictions of fuel evolution. First of all, it is necessary to validate that the clustering of Ru is energetically favored in  $\text{UO}_2$  and a simple Ru dimer would be the first step of clustering. We considered three possible dimers consisting of two Ru atoms in points defect configurations ( $\text{Ru}_I+\text{Ru}_O$ ,  $\text{Ru}_I+\text{Ru}_U$ , and  $\text{Ru}_U+\text{Ru}_O$ ) and then found that  $\text{Ru}_I+\text{Ru}_U$  is the most energetically favored configuration among them (see Table 3-8). Thus we selected this configuration to

assess the stability of the dimer relative to dispersed Ru atoms in  $\text{UO}_2$ . In order to do this, a separated dimer, which has a longer Ru-Ru distance (4.88 Å) than that of the bound dimer (2.51 Å), is examined (see Figure 3-3). The total energy of the  $\text{UO}_2$  supercell containing the separated dimer is 0.98 eV higher than that of the bound dimer case. This indicates that the total energy of Ru-bearing  $\text{UO}_2$  can be lowered by the agglomeration of Ru fission products.

As presented in Figure 3-3, however, a bound dimer induces large distortions in the surrounding oxygen sub-lattice (maximum displacement of matrix elements,  $\Delta d_{\text{max}}$ , is 0.48 Å), which possibly implies interactions between Ru and surrounding oxygen atoms, or an oxidation of the Ru atoms. This might not best represent the case in which we are interested (metallic inclusion). In addition, it is experimentally more likely that fission products reside in existing defects with free volume when they agglomerate, which are generated in a great amount during the irradiation of the fuel, rather than substitute host elements. Hence a bound Schottky defect in  $\text{UO}_2$  is chosen as the nucleus of a nanovoid in which the fission products can easily reside. A Ru atom, dimer and trimer are then each placed in this Schottky defect and examined to understand how they evolve to a cluster. The final configurations depicted in Figure 3-4 indicate that even three Ru atoms are easily accommodated into the Schottky defect without significant lattice distortion ( $\Delta d_{\text{max}} = 0.14 \text{Å}$ ). This is because the Schottky defect has more free volume to contain Ru atoms than point defects (vacancies), as one would expect.

The solution and binding energies of clustered Ru are given in Table 3-9. The binding energy is the energy needed to bring Ru atoms in separated Schottky defects

into one Schottky defect, with the remaining empty Schottky defects spaced far apart. While the binding energies indicate that it is favorable to bring two Ru atoms together into one Schottky, there is an abrupt increase in energy in going from the dimer to the trimer configuration, which implies that the dimer is the most stable Ru cluster in a Schottky defect. In fact, while dimers are bound within the Schottky, trimers are actually repelled. Therefore it is reasonable to conclude that Ru clustering occurs where there is enough empty space in the lattice, but that only a few Ru atoms can be accommodated into one Schottky, suggesting that the nucleus of the metallic inclusions may be metal dimers incorporated within Schottky defects.

As metallic inclusions precipitate in the matrix, they will have profound effects on the fuel, modifying properties such as thermal conductivity and mechanical properties. To assess the influence of metallic aggregates on the electrical properties of the fuel, the electronic density of states (DOS) of all three cases of Ru-bearing Schottky defects are analyzed. The total DOS of Ru-bearing  $\text{UO}_2$  shows that more electronic states are introduced within the gap of  $\text{UO}_2$  as the Ru atoms agglomerate. Further, the partial DOS of Ru clusters confirm that even a cluster as small as the dimer or trimer shows a DOS very similar to that of metallic Ru (Figure 3-5). Therefore Ru clusters in  $\text{UO}_2$  become metallic at the very earliest stage of clustering – even trimers exhibit some metallic character. This also demonstrates that current empirical potentials of FPs in  $\text{UO}_2$ , which can only describe ionic bonding, are expected to describe even the simplest of metallic clusters poorly.

### **Fission Product Segregation to Grain Boundaries in $\text{UO}_2$**

Grain boundaries are important for controlling many properties in oxides, including the nucleation of new phases and the segregation and transport of ions,

including impurity ions<sup>132</sup>. This is especially true in  $\text{UO}_2$  because the fuel pellets of  $\text{UO}_2$  typically consists of micron-sized grains<sup>4</sup>. Consequently, grain boundaries are the most abundant structural defects in  $\text{UO}_2$  pellets and they play an important role in the accommodation of fission products, serving as nucleation sites for fission gas bubbles and metallic precipitates<sup>4</sup>. In addition, numerous fission products of different elements, charges, and sizes are generated throughout the fuel matrix during the operation. Therefore, quantifying the interactions of fission products with  $\text{UO}_2$  grain boundaries is thus important for both understanding and predicting the behavior of the fuel under service. Here, the interactions of a range of fission products with a model grain boundary in  $\text{UO}_2$  are examined at the atomic scale with empirical potentials, with selected results involving Xe and Ru examined further with density functional theory (DFT) calculations. The results provide insight into the roles of fission product charge and ionic radius on the propensity of fission products to segregate to grain boundaries in  $\text{UO}_2$ .

### **Computational Details**

The  $\Sigma 5(310)/[001]$   $\theta=36.9^\circ$  symmetric tilt grain boundary is the model system selected for this work, which is one of the low energy boundaries in  $\text{UO}_2$ <sup>133</sup>. The initial structure constructed using GBstudio<sup>134</sup> contains uranium-uranium and oxygen-oxygen pairs at the boundary plane that are spatially very close and thus experience large repulsions; therefore a modification of the boundary is needed to achieve a more reasonable configuration. This can be done via two approaches: minimizing the boundary energy with respect to the relative translation of the two grains (mapping the  $\gamma$  surface)<sup>135</sup> or removing atoms systematically, resulting in a reduced density of atoms at the grain boundary<sup>136, 137</sup>. While in principle both degrees of freedom should be

minimized concurrently to obtain the global energy minimum, typically only one of the two methods is applied to minimize computational cost. In this work, we chose the latter approach. In particular, half of the uranium atoms near the grain boundary that were too close to other atoms, along with their corresponding oxygen pairs, were removed followed by a full relaxation of all ions using the General Utility Lattice Program (GULP)<sup>138</sup>. We have tested several geometries where near-pairs were removed and used the lowest energy structure found (Figure 3-6) for the rest of the work. While there is no guarantee that this approach will provide the global minimum energy structure of the boundary, we expect that the structure obtained is representative of that in the real material. Indeed, the atomic structure of this boundary is similar to that obtained previously by  $\gamma$  surface mapping and consistent with the Z-contrast STEM image for the  $\Sigma 5$  (310) grain boundary of yttria-stabilized  $\text{ZrO}_2$ , which has the fluorite structure, by Dickey *et al.*<sup>136, 139</sup>

To determine the dependence of the fully relaxed atomic structure of this boundary on the particular empirical potential employed, we determined the structure using three different empirical potentials (Basak<sup>140</sup>, Busker<sup>141</sup>, and Grimes<sup>89</sup>), confirming that the resulting boundary structures are almost identical to each other, although the absolute values of grain boundary energies do differ (0.116 eV/Å<sup>2</sup>, 0.155 eV/Å<sup>2</sup>, and 0.195 eV/Å<sup>2</sup>, respectively). Because Grimes<sup>89</sup> has also reported a set of empirical potentials which encompasses a wide variety of fission products, we used the Grimes potential to investigate the segregation of fission products. Particularly, potentials for Ru of various charge states are from Busker *et al.*<sup>142</sup>

## Segregation Energy Calculations by Empirical Potentials

The segregation energy of each fission product is defined as the total energy difference of placing the fission product at the grain boundary relative to placing it in a perfect  $\text{UO}_2$  lattice (or, equivalently, as the difference in chemical potential in the bulk compared to at the grain boundary). However, the atomic configuration of the grain boundary is complex and thus the segregation energies depend on the specific segregation sites as determined by the atomic structure of the boundary, as Nerikar *et al.*<sup>143</sup> reported for Xe segregation in  $\text{UO}_2$ . Therefore it is necessary to construct a segregation energy profile across the grain boundary that considers all possible segregation sites. To obtain this profile, we substituted the fission product for one of the uranium ions, one at a time, for all the uranium ions in the system. We performed this set of calculations for all of the fission products, spanning different ionic charges and radii, which are available in the Grimes potential set (a total of thirteen fission products), and constructed segregation profiles for all of them. The charge of the system caused by aliovalent cations has been compensated by a uniform background charge as implemented in the GULP. Figure 3-7 illustrates typical energy profiles for alio- and isovalent fission products. Segregation profiles for other fission products are very similar (exceptions are discussed below).

It is notable that the segregation profiles in Figure 3-7 do not exhibit an electrostatic dipole (observed for the same grain boundary type with an atomic structure determined by  $\gamma$  surface mapping<sup>143</sup>) resulting in segregation profiles that are symmetric. In addition, there are two sites that are especially preferred, depending on the species in question, labeled the *a*- and *b*-site for Xe and  $\text{Ru}^{4+}$ , respectively (see also Figure 3-6). It is interesting to note that for nearly all of the other fission products considered, a

similar segregation site preference is observed, i.e., the lowest energy site for aliovalent ions is the *a*-site, while that for isovalent ions is the *b* site. Segregation energies at these two sites for all the fission products are tabulated in Table 3-10. Clearly, there is gradual change in segregation energy which seems to be related to charge and/or size of segregates for both sites. This is discussed in detail below.

The primary difference between the two low-energy sites is the configuration of surrounding oxygen ions and resulting free volume. The *a*-site, which is in the uranium layer with the half-filled column formed as a consequence of the removal of atoms in constructing the boundary, is adjacent to the free volume formed by the removal of two oxygen ions. The remaining six neighboring oxygen ions tend to maintain their original positions within the fluorite structure (see the left-most inset within Figure 3-7) so that the *a*-site has significant free volume associated with it. When lower valence ions, which do not interact nearly as strongly with oxygen ions, segregate to this *a*-site, they are able to relax into the free volume – the surrounding constitutional or structural vacancies<sup>144</sup> – and so are able to maximize their separation from the surrounding oxygen ions. For instance, the fully relaxed structure of Xe in *a*-site confirms that the final Xe position is near the center of the free volume and its average separation from its neighbors is over 3 Å (the average U-O bond length at the *a*-site is 2.22 Å). On the other hand, the *b*-site, which is in the uranium layer without the half-filled column, is more closely packed with surrounding oxygen ions. Therefore, only higher valence ions have any tendency to segregate to the *b*-site, maximizing their interaction with those oxygen ions. In the case of Ru<sup>4+</sup> in the *b*-site, the resulting Ru-O configuration is similar to that of rutile RuO<sub>2</sub> with an average Ru-O bond length of 1.99 Å, which is even smaller

than that of the original U-O at *b*-site (2.20 Å). Thus the segregation tendency of Ru<sup>4+</sup> into the *b*-site is significant, when compared to other isovalent ions.

These results suggest that the charge of the segregates and the preferred oxide coordination of the segregate are significant factors in determining segregation behavior. Ba<sup>2+</sup> and Ce<sup>4+</sup> are slightly off this trend and their lowest energy sites are the nearest neighboring sites of the *a*-site, sites which maintain the fluorite structure and coordination but with elongated U-O bond lengths. The fact that Ce<sup>4+</sup> – one of the isovalent ions – prefers this fluorite-like site over the *b*-site supports the idea of oxide formation tendencies being a determiner for what sites are preferred. This will be discussed later in detail.

### **Effect of Charge on FP Segregation**

To understand the dependence of the segregation behavior of fission products on the bonding environment of the segregation site in further detail, DFT calculations are performed for both Xe and Ru. Details of the calculations are the same as in the previous section. For efficiency, only the two lowest energy sites discussed above were examined in a supercell containing a grain boundary structure that was reduced in size by half along both the *y*- and *z*-axes indicated in Figure 3-6, but which maintains the essential geometrical features of the  $\Sigma 5$  grain boundary. Despite the small system size, the fully relaxed structure is quite similar to that found using the potential. The segregation energies of Xe in the *a*- and *b*-site are predicted to be -4.44 eV and -2.17 eV and the average Xe-O bond length in the lowest energy site is 3.15 Å (in *a*-site). The corresponding values for Ru are -3.14 eV, -3.22 eV and 2.04 Å (in *b*-site), respectively.

These values agree well with the trends predicted using the Grimes potential (Table 3-10). Further, spin density analysis indicates that Xe substituted for U oxidizes

four neighboring  $U^{4+}$  ions into  $U^{5+}$ , which is expected for the inert impurity substituted at a cation site, while Ru does not affect neighboring U ions. That is, because the replacement of  $U^{4+}$  with Xe results in the “loss” of 4 electrons that the neighboring oxygen normally accept from the original U, the remaining U ions donate an extra electron to stabilize the system. Bader charge analysis<sup>145</sup> confirms that Xe alters the effective charge of oxygen ions over a wide spatial extent while Ru transfers charges locally, to neighboring O ions, as illustrated in Figure 3-8. This is a direct consequence of the number and distribution of U ions which are oxidized to  $U^{5+}$  in each case. We note that, while the potential does not account for this charge transfer, it still predicts the correct trend in terms of which site, *a* or *b*, is preferred. This is because the charge transfer is more or less independent of where the Xe is inserted and thus cancels when comparing different sites.

### **Effect of Ionic Radius on FP Segregation**

Because the size mismatch of segregates has been considered the primary factor determining segregation, especially in metals<sup>146</sup>, it is reasonable to think that the size of the impurity ion may also influence its segregation in an oxide<sup>147-150</sup>. The segregation energies for the *a*-site listed in Table 3-10 show that the absolute segregation energy tends to decrease as the valence increases, which correlates with decreasing ionic radius. Hence, in Figure 3-9, we have plotted segregation energies of several cations in Table 3-10 as a function of the ionic radii reported by Shannon *et al.*<sup>151</sup>

While the dataset is not large, one may draw several conclusions. First, the segregation energies of isovalent ions which have similar radii with  $U^{4+}$  are relatively small. This is consistent with the segregation behavior of fission products on  $UO_2$

surfaces.<sup>152</sup> The fact that  $Zr^{4+}$  and  $Ce^{4+}$  have relatively weak tendencies to segregate to the boundary while  $Ru^{4+}$  does not is also consistent with the types of oxides these cations form. Zr and Ce form fluorite or fluorite-like compounds, similar to U, while Ru does not, forming rutile instead. Second, the segregation becomes more site-sensitive as the ionic radius increases, especially for aliovalent ions. This clearly indicates preferential segregation of larger aliovalent impurities to free spaces, which also can be rationalized by the types of oxides they form. The aliovalent ions do not form fluorite-like oxides and thus will strongly prefer non-fluorite oxygen environments at the grain boundary. This suggests a connection between solubility and segregation tendency, as insoluble species will have a stronger tendency to segregate to non-fluorite sites.

### Factors that Affect FP Segregation

Finally, to better deconvolute the roles that charge and size play in fission product segregation to the boundary, we calculate segregation energies of an artificial U cation to both the *a*- and *b*-sites as a function of valence (*q*) and one of the adjustable parameters for the cation-anion short range interaction ( $\rho$ ), which is most related to the ionic radius as indicated in the Buckingham pair potential described in Chapter 2.

$$U_L = \frac{1}{4\pi\epsilon_0} \sum_{i \neq j} \frac{q_i q_j}{r_{ij}} + A e^{-r_{ij}/\rho} - \frac{C}{r_{ij}^6} \quad (2-2)$$

The result, given in Figure 3-10, is consistent with the trend found in Figure 3-9. First, *a*-site is preferred for the vast majority of the parameter space while *b*-site is not largely favored. Second, the change in segregation energy associated with ionic radius becomes more dramatic as the valence of species becomes closer to 4+ for both *a*- and *b*-site. Third, for large species, the dependence on valence is negligible for the *b*-site but is strong for the *a*-site. For small species, however, the overall trend is quite similar

for both sites. All these results lead to a more general conclusion. Segregates in  $\text{UO}_2$  will find free space first regardless of their charges or sizes though the segregation tendency is governed by both, simultaneously. When the segregates are small and have a valence similar to that of uranium, however, they might prefer a more closed-packed site (*b*-site), possibly making bonds with surrounding oxygen ions.

## Discussion

These results have interesting implications for the evolution of fission product segregation in  $\text{UO}_2$ . Aliovalent ions will diffuse to sites with greater free volume while isovalent ions diffuse to sites with greater oxygen coordination. However, in particular for aliovalent ions, their incorporation is accompanied by changes in the uranium valence. Thus, there will be a limit to the number of aliovalent ions that can be placed near a given site as there will be, at some point, no  $\text{U}^{4+}$  to oxidize to  $\text{U}^{5+}$ ; it will all be  $\text{U}^{5+}$ . This means that, at some point, the incorporation of these ions must be accompanied by the removal of further oxygen ions to stabilize the local charge. Further, these results provide insight into how doping might be used to control fission product segregation and precipitation. If the fuel is fabricated with isovalent dopant ions that have strong interactions with oxygen, they may fill the *b*-type sites in the boundaries, eliminating sites for isovalent fission product segregation, suppressing that segregation. How multiple impurities/dopants interact to change the overall segregation tendencies requires further work, but these results suggest that there may be opportunities for exploiting these interactions in fuel design.

There are a few limitations to this study. First, due to the nature of the potential used, it is not possible to consider the interaction between multiple fission products at one time. Nor is it possible to study how the charge state of the fission product changes

with spatial location near the grain boundary. This is a consequence of the fixed charge on the ions within this potential. When multiple fission products interact, their charge state might change dramatically, as we have indeed seen in the clustering of Ru within the  $\text{UO}_2$  matrix<sup>153</sup>. Some of these limitations can be circumvented by using DFT, as we have done for Xe and Ru, but new limitations related to system size and computational efficiency arise. Even so, at least for the cases of Xe and Ru, we find that the charge state of the substitutional species is relatively constant regardless of where it is placed within the system, suggesting that the fixed charge assumption of the potential is physically reasonable, at least for this scenario. This is true even though Ru is very flexible in its charge state. However, if the environments change to even greater extents than considered here, it is very possible that other valence states for the various fission products might be preferred.

### **Effect of Cr Doping in $\text{UO}_2$**

Fission gas retention and release are important phenomena of nuclear fuels that significantly influence fuel lifetime and performance. Among many proposed approaches to control the fission gas behavior of  $\text{UO}_2$ , enlarging the grain size has received great interest because large grains also improve the material's thermal conductivity especially in sub-micron regime, which is desirable because the low thermal conductivity causes a high lateral thermal gradient across the  $\text{UO}_2$  fuel pellet that leads to thermal cracks and poor heat transfer.  $\text{Cr}_2\text{O}_3$  is a standard grain growth promoter for  $\text{UO}_2$ <sup>154</sup> and improved retention fission-gas retention in  $\text{Cr}_2\text{O}_3$ -doped  $\text{UO}_2$  has been experimentally observed<sup>155</sup>. Determining the correlation between the extent of  $\text{Cr}_2\text{O}_3$  doping and the amount of grain growth along with the corresponding mechanisms

has been the objective of several studies<sup>156, 157</sup>. However, there is much that is not yet understood regarding the factors that govern grain growth.

Electronic-structure calculations have been instrumental in explaining various phenomena such as high electrical conductivity and creep resistance in oxide materials with grain boundaries modified by segregated impurities<sup>147, 158-160</sup>. In particular, these calculations have quantified the changes in local electron density and associated bond properties of the segregates with the oxide matrix. In this section, we establish the electronic structure of  $\text{UO}_2$  grain boundary with segregated Cr using DFT and quantify the effects of Cr in terms of grain growth to better understand the precise role that Cr additions have in promoting grain growth in  $\text{UO}_2$ .

### **Computational Details**

The modeled grain boundary is the same  $\Sigma 5$  grain boundary used for the DFT study in previous grain boundary section. As a preliminary study to confirm the segregation tendency of Cr to this boundary, the atomic structure is fully relaxed (keeping cell dimensions fixed) following the substitution of a single Cr for one U atom, one at a time for all the U atoms in the simulation supercell with the interatomic interactions described by the empirical potential parameterized by Busker<sup>141, 161</sup>. The relative total energy profile across the grains (see Figure 3-11, right) indicates that Cr has a strong segregation tendency to the  $\Sigma 5$  boundary, with the lowest segregation energy of  $-2.39$  eV at the center of the grain boundary. We use this result from empirical potentials as a compelling motivation for DFT studies of Cr incorporation at the grain boundary, assuming that Cr incorporation will thus occur at the center of the boundary.

To find the appropriate accommodation site for Cr, which we will use as input to the grain boundary study, the solution energies of Cr for three solution sites in bulk – uranium substitutional site, oxygen substitutional sites, and octahedral interstitial – are determined using the same supercell used in the previous Ru study. Other calculation details are also similar. The resulting solution energies (see Table 3-11) confirm that Cr prefers to reside in a U substitutional site over the octahedral interstitial and the oxygen substitutional sites under the stoichiometric and hyper-stoichiometric regimes of  $\text{UO}_2$ , which correspond to typical operating conditions in actual fuels. In the hypo-stoichiometric regime, the interstitial site is preferred although Cr is predicted to be insoluble in this site. Based on these results, we focus on the two cases of Cr in the U substitutional site ( $\text{Cr}_\text{U}$ ) and the interstitial site ( $\text{Cr}_\text{i}$ ) at the grain boundary. For all DFT calculations of grain boundary structures, the Brillouin Zone is sampled with just the gamma point.

### **Cr Segregation to the $\Sigma 5$ Grain Boundary: DFT Confirmation**

First, the segregation tendency toward the grain boundary is confirmed by DFT: we replace the U atom which exhibits the lowest energy in the segregation profile (Figure 3-11) with Cr for the  $\text{Cr}_\text{U}$  case and place Cr in the large free space at the center of the grain boundary for the  $\text{Cr}_\text{i}$  case. Energetics at these grain boundary sites are compared to Cr in the bulk region of the supercell, replacing a U atom and occupying octahedral interstitial, respectively. The segregation energy is calculated as the corresponding energy differences between the grain boundary and the bulk cases (the classical Langmuir-McLean approach).

It is notable that the atomic configuration around Cr near the grain boundary is far from the original fluorite structure of  $\text{UO}_2$  for both  $\text{Cr}_\text{U}$  and  $\text{Cr}_\text{i}$  cases. In particular,  $\text{Cr}_\text{U}$

site is surrounded by six oxygen atoms and  $Cr_i$  site is a free space with only four adjacent oxygen atom neighbors rather than an octahedral interstitial site in bulk area. The resulting segregation energy for  $Cr_U$  is  $-2.28$  eV, which agrees semi-quantitatively with the predictions of the empirical potential ( $-2.39$  eV). Interestingly, a very similar segregation energy ( $-2.28$  eV) is predicted for  $Cr_i$ ; the segregation energy difference between  $Cr_U$  and  $Cr_i$  is just a few meVs (we note that this depends on the selected site and it is possible that lower energy interstitial sites may exist). Thus, whether Cr at the boundary is incorporated as substitutional or interstitial depends on the bulk solubility of each form which in turn depends on the stoichiometry. Together with the Table 3-11, we can reasonably predict that U substitutional sites will be the dominant segregation site for Cr under the hyper-stoichiometric regime (typical operation condition) while interstitial sites will be preferred under the hypo-stoichiometric regime.

Figure 3-12 illustrates the atomic configurations of the grain boundary when Cr is added. In the case of  $Cr_U$ , the six O atoms that neighbor Cr relax inward, resulting in an average bond length for Cr-O that is shorter ( $2.05$  Å) than that of the original U-O bonds ( $2.26$  Å). In fact, the average bond length after Cr substitution is quite close to the Cr-O bond length of bulk  $Cr_2O_3$  ( $2.01$  Å) predicted by DFT which has a corundum structure with a coordination number of six. This implies that Cr forms a strong bond with O atoms near the grain boundary, where it is less coordinated than in the bulk. In the case of  $Cr_i$ , Cr relaxes towards the O atoms, increasing the distance from neighboring U atoms. The Cr has only four O atoms with which to form bonds: the resulting average bond length is longer ( $2.16$  Å) than that of  $Cr_U$ . These imply weaker bonds as well as less charge transfer from Cr to O atoms.

## Electronic Structure at the Grain Boundary

To analyze the electronic structure near the boundary, we use Bader charge analysis<sup>145</sup> for both Cr solution sites (see Figure 3-13). The less coordinated character of the grain boundary is well reflected in the effective charges of both U and O. That is, the absolute values of the effective charges for both U and O atoms are smaller than those of bulk  $\text{UO}_2$ . For the  $\text{Cr}_\text{U}$  case, the effective charges of several O atoms at the boundary are similar to those in bulk of  $\text{Cr}_2\text{O}_3$  ( $-1.27e$ ) which supports the conclusion that Cr-O bonds form; such  $\text{Cr}_2\text{O}_3$ -like charges are hardly observed in the  $\text{Cr}_\text{i}$  case. In addition, the Cr segregation changes the effective charges of O atoms over a greater spatial range in the  $\text{Cr}_\text{U}$  case while its effect is rather localized in the  $\text{Cr}_\text{i}$  case. In particular, the relaxation of six O atoms towards Cr modifies the character of adjacent U-O bonds. Interestingly, in the case of  $\text{Cr}_\text{U}$ , there is one U atom which exhibits a particularly high effective charge, significantly higher than those atoms in the bulk region; spin density analysis confirms that this U atom has a higher valence (5+) than U atoms in the bulk (4+).

This is consistent with the experiments by Leenaers *et al.*<sup>157</sup> that reported a decrease in  $\text{UO}_2$  lattice parameters when  $\text{Cr}_2\text{O}_3$  was introduced, which they assumed to be due to the oxidation of  $\text{U}^{4+}$  into  $\text{U}^{5+}$ . In contrast, there is a U atom which exhibits low effective charge with a slightly lower valence at the grain boundary than in the bulk when  $\text{Cr}_\text{i}$  is introduced. Therefore we conclude that when Cr segregates to the grain boundary as a substitutional species, it forms bonds with the surrounding O atoms, altering the charge states of many neighboring atoms and possibly the bond character of adjacent U-O bonds. When Cr segregates as an interstitial species, however, it only donates approximately one electron to the neighboring atoms without further effects.

For comparison, the effective charges for the case where Cr is added to the bulk area are also examined (see Figure 3-14). The oxidation of a U atom and the alteration of O charges near the Cr site are observed when Cr replaces U in the bulk region while those changes are not present when Cr occupies the octahedral interstitial site. Unlike the  $Cr_i$  case at the grain boundary that exhibits a particularly low charge of one U atom, there are several U atoms with smaller charges because of the rigidity of the bulk region<sup>162</sup>. That is, the relaxation of cation atoms is limited in the bulk and therefore the effect of Cr incorporation is slightly extended, though the valence changes are found to be negligible by the spin density analysis.

The charge density difference with and without Cr segregation is analyzed to assess the modification of bond character near the grain boundary; the results are depicted in Figure 3-15. For the  $Cr_U$  case (upper five images), an increase of the electron density at the bond between U and O is clearly predicted. This implies that the segregated Cr forms Cr-O bonds and accordingly weakens the ionic character (i.e., increases the covalent character) of U-O bonds around the newly formed Cr-O bonds. A similar effect has been reported for Ge dopants in tetragonal zirconia polycrystal (TZP) by Yoshida *et al.*<sup>163</sup> and the enhanced covalent character was considered as the origin of its superplasticity which requires large amount of atomistic rearrangement. In addition, enhance grain boundary diffusion in the 3 mol% yttria-stabilized TZP (3Y-TZP) has been reported by Boniecki *et al.*, which is mainly attribute to the reduction of ionic bond strength between cation and anion by various dopants<sup>164</sup>. For a dopant to facilitate grain growth in an oxide, the ionic nature of the bonds within the oxide must be weakened so that the cations can be more easily rearranged within the material<sup>165</sup>; if cations are

immobile, grain growth will not easily occur. Therefore, the capability of Cr to weaken the ionic nature of the bonds within  $\text{UO}_2$  can be one of the relevant signatures of its ability to promote enhanced cation mobility, and eventually grain growth. In the case of  $\text{Cr}_i$ , in contrast, no evidence of a change in the nature of the U-O bond is found and a localized charge near the segregated Cr is predicted, as expected.

### **Conclusions**

The behavior of impurities in  $\text{UO}_2$  fuel was examined using computational methods especially in terms of their interactions with defect structures within the  $\text{UO}_2$ .

Firstly, the solubility of Ru in  $\text{UO}_2$  and its clustering behavior was explored using DFT. The results demonstrate that the solubility of the Ru atom is very sensitive to the reference state chosen, so two possible reference states are considered in the calculations. The uranium vacancy ( $V_U$ ) site is predicted to be the most energetically favored solution site for the Ru atom, which is actually soluble at  $V_U$  under hyperstoichiometric ( $\text{UO}_{2+x}$ ) conditions, particularly when the reference state is bulk metal; otherwise Ru is insoluble in  $\text{UO}_2$ .

Further calculations for Ru dimers and trimers demonstrate that the system is stabilized when Ru atoms agglomerate together. Defect clusters in  $\text{UO}_2$ , such as a bound Schottky, can promote Ru clustering by providing the necessary free volume in which to accommodate the Ru atoms. Binding energy calculations indicate that the size of the Ru cluster itself seems to be limited by the free volume of the defect structure where the cluster forms. In particular, the Ru dimer is the most stable cluster in the bound Schottky defect in  $\text{UO}_2$  while the trimer is too large to be accommodated in such site. Additionally, the partial DOS of Ru clusters in the bound Schottky confirm that even the smallest of Ru cluster – the dimer – begins to exhibit metallic characteristics. All of

these results indicate that the nucleus of the metallic inclusions in  $\text{UO}_2$  may be the Ru dimer in a bound Schottky defect and that even small agglomerates of metallic fission products will begin to modify the electronic structures of the fuel significantly. These results suggest that the growth of metallic inclusions will occur via the diffusion and aggregation of metal-bearing Schottky defects, though such diffusion would require additional vacancies to occur.

Secondly, the segregation of various fission products to a modeled symmetric  $\Sigma 5$  tilt grain boundary of  $\text{UO}_2$  was examined using empirical potentials and DFT. The segregation tendencies were determined by taking into account incorporation site, ionic radius, and charge state of the fission products. In particular, the aliovalent ions are predicted to be more sensitive to the size of the free space where they can reside, while the isovalent atoms are more sensitive to the bonding environment with surrounding oxygen ions. The unbalanced local charges due to the incorporation of those fission product ions are predicted to be compensated by introducing additional intrinsic defects in the host  $\text{UO}_2$  matrix. This suggests that fission products segregation or precipitation might be controlled by doping the  $\text{UO}_2$  fuel, although this needs to be verified by additional work.

Lastly, Cr incorporation at the  $\Sigma 5$  grain boundary was investigated using empirical potential and DFT. When Cr resides in the U substitutional site at the grain boundary, the neighboring O atoms relax towards the Cr and form Cr-O bonds with the bond length similar to that of  $\text{Cr}_2\text{O}_3$ . This induces the increased electron density in between U and O atoms around the Cr-O bonds while the absolute values of their effective charges are smaller than those of atoms in the bulk, which is mainly due to the

less coordinate configuration of the grain boundary. Therefore the ionic nature of those U-O bonds becomes weaker, which implies enhanced cation mobility that would be expected to enhance  $\text{UO}_2$  grain growth. In contrast, when Cr resides in the interstitial site in the bulk or the free space at the grain boundary, it donates charges to the surroundings without further alteration of electronic environment.

Table 3-1. Defect formation energy of uranium vacancy in UO<sub>2</sub> for different *k*-meshes

<i>k</i> -mesh	Defect formation energy of V <sub>U</sub> (eV)
1×1×1	8.598
2×2×2	9.675
4×4×4	9.761

Table 3-2. Trap site formation energies of defects in UO<sub>2</sub><sup>87, 101</sup>

Trap Site	Formation energy		
	UO <sub>2-x</sub>	UO <sub>2</sub>	UO <sub>2+x</sub>
V <sub>O</sub>	$-kT \ln\left(\frac{ x }{2}\right)$	$\frac{E_{FPO}}{2} + \frac{kT}{2} \ln(2)$	$E_{FPO} + kT \ln(x)$
V <sub>U</sub>	$2kT \ln\left(\frac{ x }{2}\right) + E_{Sch}$	$E_{Sch} - E_{FPO} - kT \ln(2)$	$E_{Sch} - 2E_{FPO} - 2kT \ln(x)$
DV	$E_{Sch} - B_{DV} + kT \ln\left(\frac{ x }{2}\right)$	$E_{Sch} - \frac{E_{FPO}}{2} - B_{DV} - \frac{kT}{2} \ln(2)$	$E_{Sch} - E_{FPO} - B_{DV} - kT \ln(x)$
Sch	$E_{Sch} - B_{Sch}$	$E_{Sch} - B_{Sch}$	$E_{Sch} - B_{Sch}$

Table 3-3. Lattice parameters of α-U

Lattice parameter(Å)	GGA	GGA+U	Exp. <sup>166</sup>
<i>a</i>	2.739	3.338	2.836
<i>b</i>	5.852	5.956	5.866
<i>c</i>	4.965	5.715	4.935

Table 3-4. Defect formation energies (eV) of uranium and oxygen vacancies; it is assumed that UO<sub>2</sub> phase is maintained under O-rich conditions.

Defect	U-rich	Intermediate	O-rich
		$\mu_O = -10.48$ $\mu_U = -8.08$	$\mu_O = -7.5$ $\mu_U = -14.05$
V <sub>O</sub>	-0.74	2.25	4.86
V <sub>U</sub>	9.67	3.71	-1.52

Table 3-5. The chemical potentials of Ru ( $\mu_{Ru}$ ) for different reference states

Reference state	$\mu_{Ru}$	Cohesive energy (eV)
Isolated atom	-1.39	-
Bulk metal	-9.20	-7.81

Table 3-6. Incorporation energies of Ru at various trap-sites using different reference states; the lowest energies are denoted in bold.

Trap site	Incorporation energy (eV)	
	Ref. state: isolated atom	Ref. state: bulk metal
Interstitial	-1.11 (-2.46 <sup>*</sup> )	6.69
V <sub>O</sub>	-2.90 (-4.87 <sup>*</sup> )	4.90
V <sub>U</sub>	<b>-7.29 (-7.63<sup>*</sup>)</b>	<b>0.51</b>
DV	-4.84 (-7.42 <sup>*</sup> )	2.96
Sch	-5.48 (-5.85 <sup>*</sup> )	2.33

<sup>\*</sup>ref<sup>103</sup>

Table 3-7. Solution energies of Ru at various trap-sites using different reference states; the lowest energies are denoted in bold.

Trap site	Solution energy (eV)					
	Isolated atom			Bulk metal		
	UO <sub>1.98</sub>	UO <sub>2</sub>	UO <sub>2.02</sub>	UO <sub>1.98</sub>	UO <sub>2</sub>	UO <sub>2.02</sub>
Interstitial	-1.11 (-2.46 <sup>*</sup> )	-1.11 (-2.46 <sup>*</sup> )	-1.11 (-2.46 <sup>*</sup> )	6.69 (20.71 <sup>**</sup> )	6.69 (17.26 <sup>**</sup> )	6.69 (13.81 <sup>**</sup> )
V <sub>O</sub>	<b>-2.90 (-4.87<sup>*</sup>)</b>	-0.41 (-2.87 <sup>*</sup> )	2.09 (-0.87 <sup>*</sup> )	<b>4.90</b> (24.94 <sup>**</sup> )	7.40 (24.90 <sup>**</sup> )	9.90 (24.85 <sup>**</sup> )
V <sub>U</sub>	0.91 (-0.43 <sup>*</sup> )	<b>-4.08</b> (-4.43 <sup>*</sup> )	<b>-9.08 (-8.43<sup>*</sup>)</b>	8.72 ( <b>15.85<sup>**</sup></b> )	<b>3.72 (5.59<sup>**</sup>)</b>	<b>-1.27 (-4.66<sup>**</sup>)</b>
DV	-1.28 (-4.12 <sup>*</sup> )	-3.78 ( <b>-6.12<sup>*</sup></b> )	-6.27 (-8.12 <sup>*</sup> )	6.53 (14.99 <sup>**</sup> )	4.03 (8.14 <sup>**</sup> )	1.53 (1.28 <sup>**</sup> )
Sch	-2.76 (-4.35 <sup>*</sup> )	-2.76 (-4.35 <sup>*</sup> )	-2.76 (-4.35 <sup>*</sup> )	5.05 (16.09 <sup>**</sup> )	5.05 (12.64 <sup>**</sup> )	5.05 (9.19 <sup>**</sup> )

<sup>\*</sup>DFT calculations in ref.<sup>103</sup>

<sup>\*\*</sup>Atomistic calculations in ref.<sup>131</sup>

Table 3-8. Solution energies of Ru dimers in various configurations using different reference states; the lowest energies are denoted in bold.

Dimer Configuration	Solution energy (eV)					
	Isolated atom			bulk metal		
	UO <sub>1.98</sub>	UO <sub>2</sub>	UO <sub>2.02</sub>	UO <sub>1.98</sub>	UO <sub>2</sub>	UO <sub>2.02</sub>
Ru <sub>i</sub> + Ru <sub>O</sub>	<b>-6.50</b>	-4.01	-1.51	<b>9.10</b>	11.60	14.10
Ru <sub>i</sub> + Ru <sub>U</sub>	-4.08	<b>-9.07</b>	<b>-14.07</b>	11.53	<b>6.53</b>	<b>1.54</b>
Ru <sub>O</sub> + Ru <sub>U</sub>	-5.14	-7.64	-10.14	10.47	7.97	5.47

Table 3-9. Solution and Binding energies of Ru atoms in Schottky defect in UO<sub>2</sub> relative to different states (a reference state of the same cluster in the vacuum (“their own reference”) or metallic Ru)

Configuration	Solution Energy (eV)		Binding Energy (eV)
	their own reference	bulk metal	
Ru atom	-2.76	5.05	-
Ru dimer	-2.87	6.86	-0.51
Ru trimer	-1.63	11.27	1.34

Table 3-10. Segregation energies of fission products to both the *a*- and *b*-sites.

Fission product	Segregation energy (eV)	
	<i>a</i> -site	<i>b</i> -site
Br <sup>-</sup>	-6.82	-0.61
I <sup>-</sup>	-7.17	-0.55
Kr	-4.80	0.86
Br	-4.77	0.85
Xe	-5.13	0.55
I	-4.99	0.68
Te	-4.73	0.75
Br <sup>+</sup>	-2.54	0.61
Rb <sup>+</sup>	-2.66	0.62
Xe <sup>+</sup>	-3.12	0.46
I <sup>+</sup>	-3.11	0.39
Te <sup>+</sup>	-3.01	0.34
Cs <sup>+</sup>	-3.05	0.38
Ba <sup>2+</sup>	-1.89 (-1.99*)	0.33
Sr <sup>2+</sup>	-1.34	0.31
Te <sup>2+</sup>	-1.53	0.13
Y <sup>3+</sup>	-1.03	-0.52
La <sup>3+</sup>	-0.88	-0.21
†Ru <sup>3+</sup>	-1.22	-0.89
Ce <sup>4+</sup>	0.37 (-0.23*)	0.57
Zr <sup>4+</sup>	-0.36	-0.48
†Ru <sup>4+</sup>	-2.29	-2.99

\* The lowest energy site is the nearest neighbor of *a*-site.

† The pair potentials for Ru are fitted by Busker *et al.*<sup>131</sup> based on the Grimes' U-O potential.

Table 3-11. Solution energies (eV) of Cr in UO<sub>2+x</sub>; the negative sign is indicative of Cr solubility.

Solution Site	<i>x</i> = -0.02	<i>x</i> = 0	<i>x</i> = 0.02
Interstitial	5.61	5.61	5.61
V <sub>O</sub>	6.74	9.23	11.73
V <sub>U</sub>	6.30	1.30	-3.69

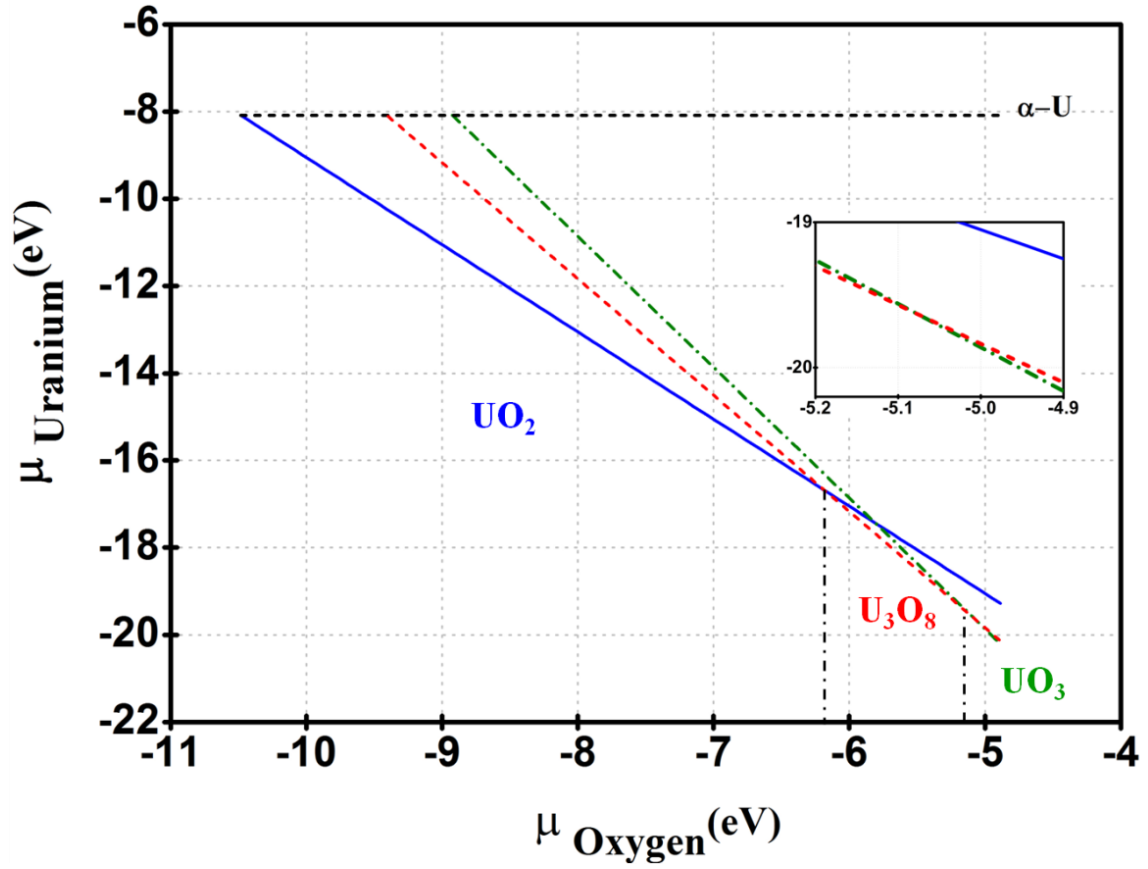


Figure 3-1. The allowed chemical potentials in various uranium oxides

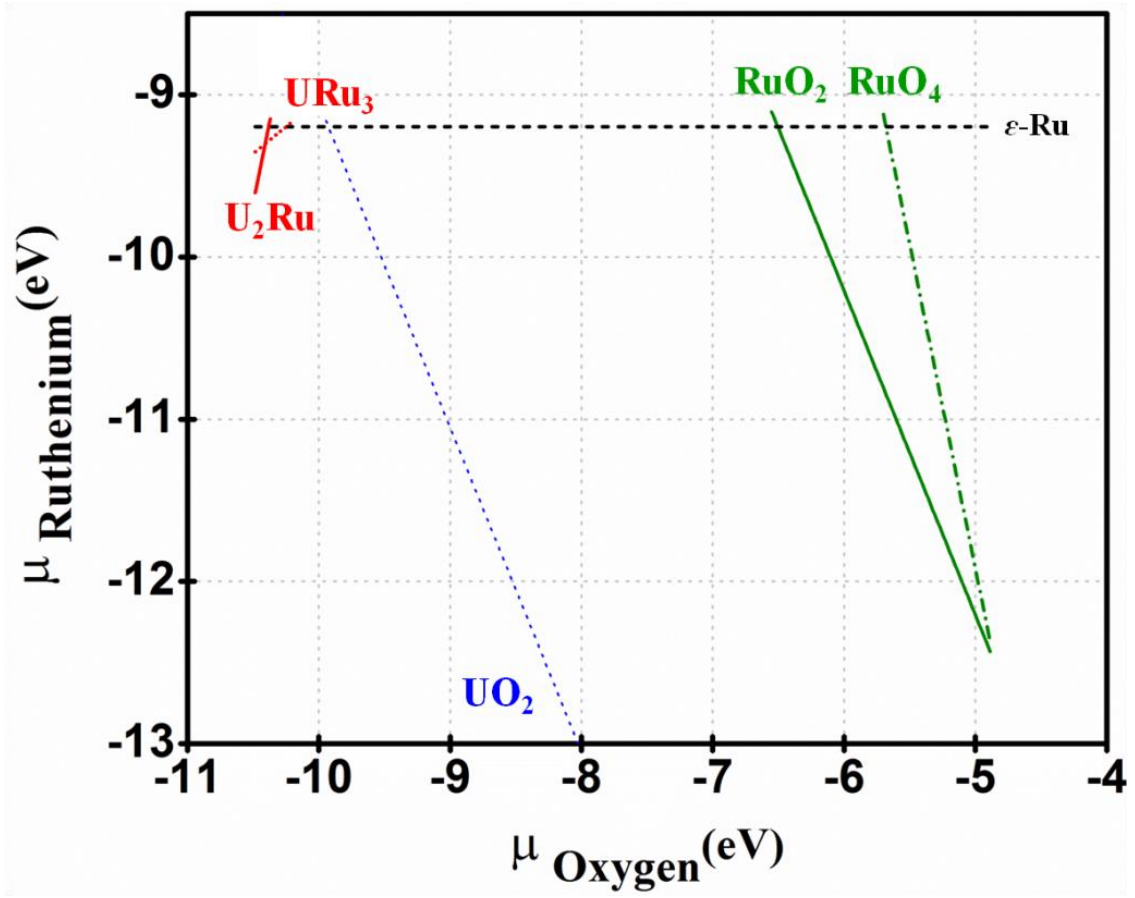


Figure 3-2. The chemical potential of Ru in  $\text{UO}_2$  within the allowed oxygen chemical potential

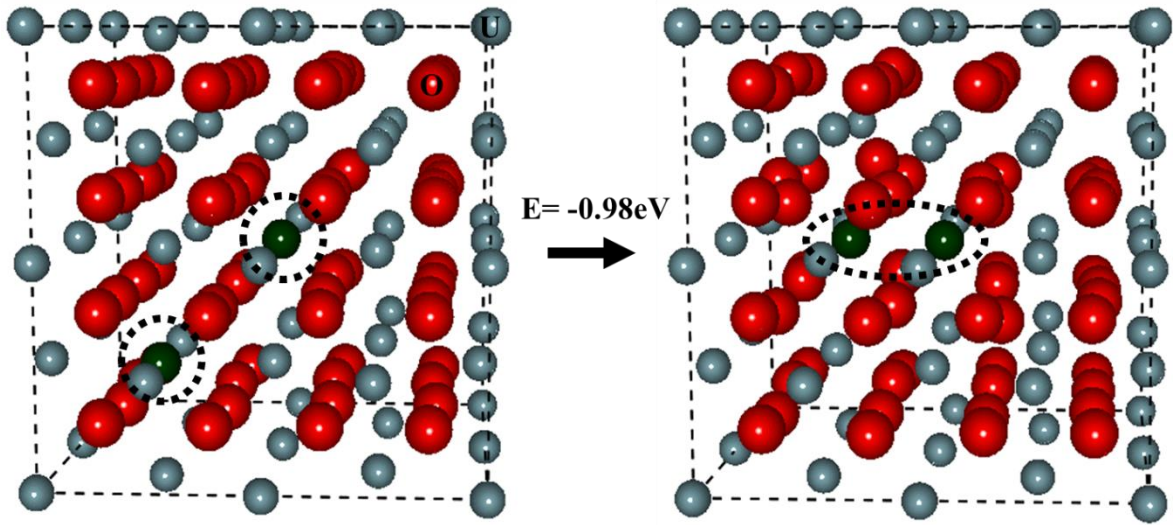


Figure 3-3. The separated  $\text{Ru}_7+\text{Ru}_U$  dimer (left) and the bound dimer (right) in  $\text{UO}_2$ : Ru atoms are circled.

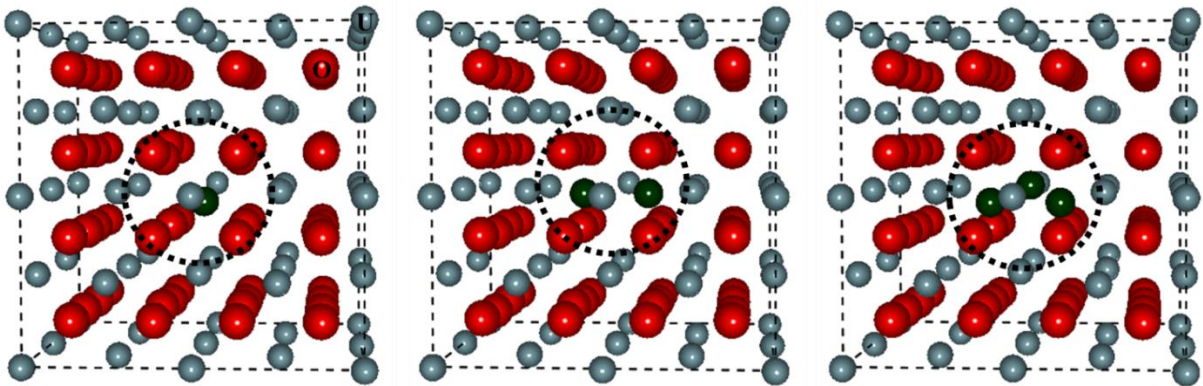


Figure 3-4. Ru atom, dimer, and trimer in the Schottky defect in  $\text{UO}_2$  (circled)

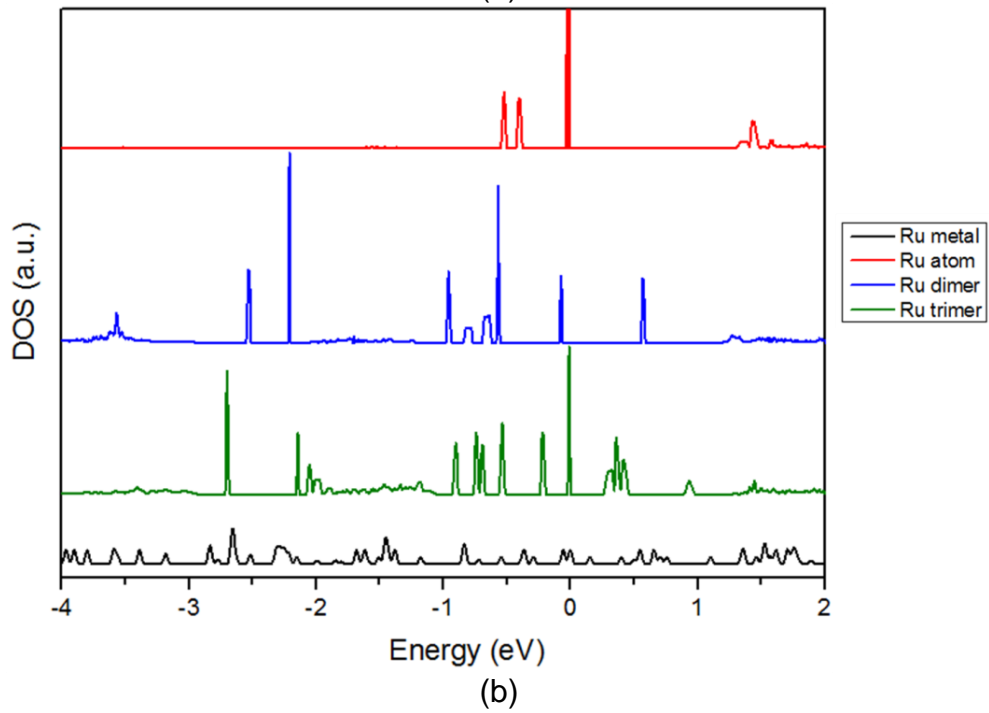
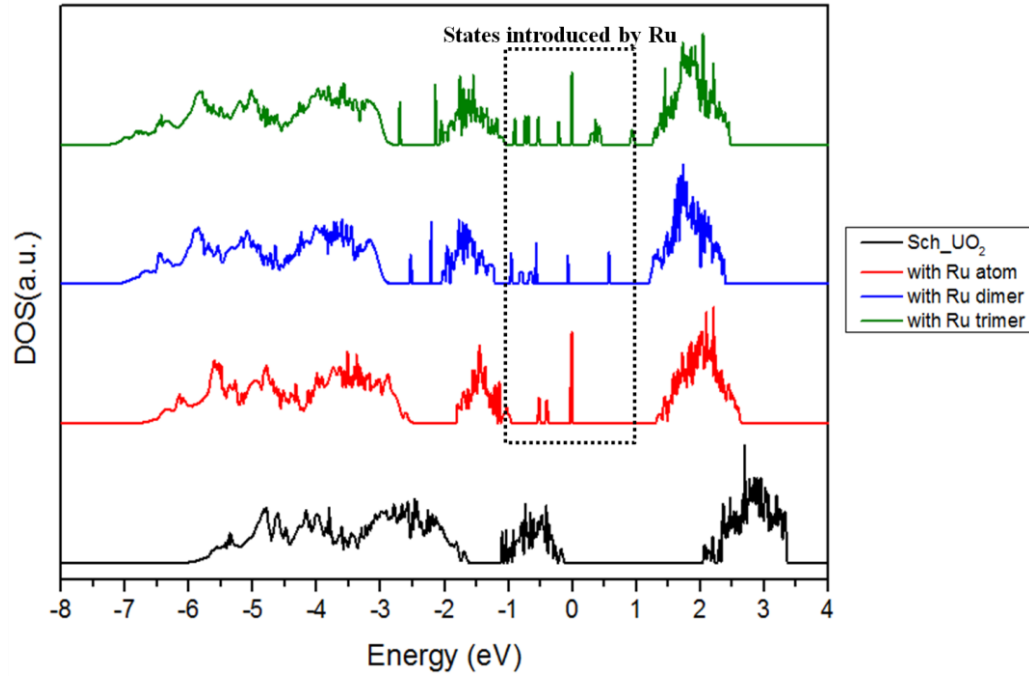


Figure 3-5. (a) DOS plots of the  $\text{UO}_2$  with Ru atoms in the Schottky defect (the Fermi energies are aligned at  $E=0$ ; that is, all states below  $E=0$  are filled while those above are empty). (b) DOS plot of the Ru metal and partial DOS plots of Ru atoms in the Schottky defect

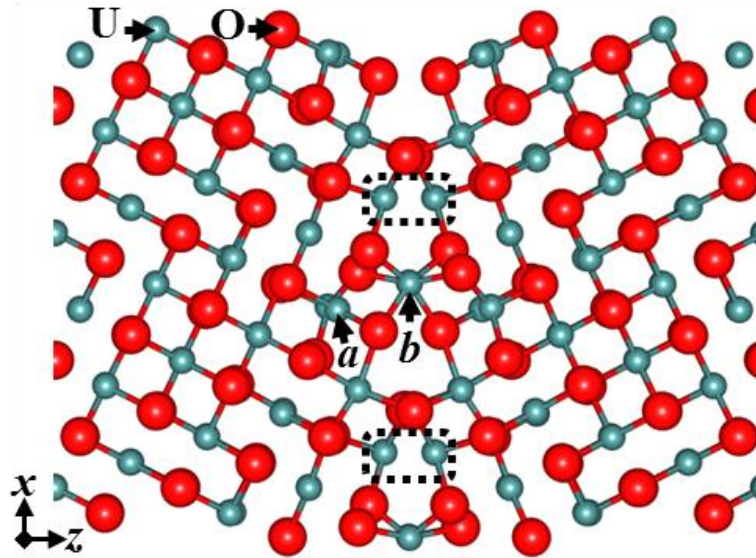


Figure 3-6.  $\Sigma 5$  (310)/[001] tilt grain boundary in  $\text{UO}_2$ ; the half-filled uranium columns resulting from removing atoms are indicated by the dotted outlines. Some segregation sites which are particularly preferred are labeled (*a* and *b*).

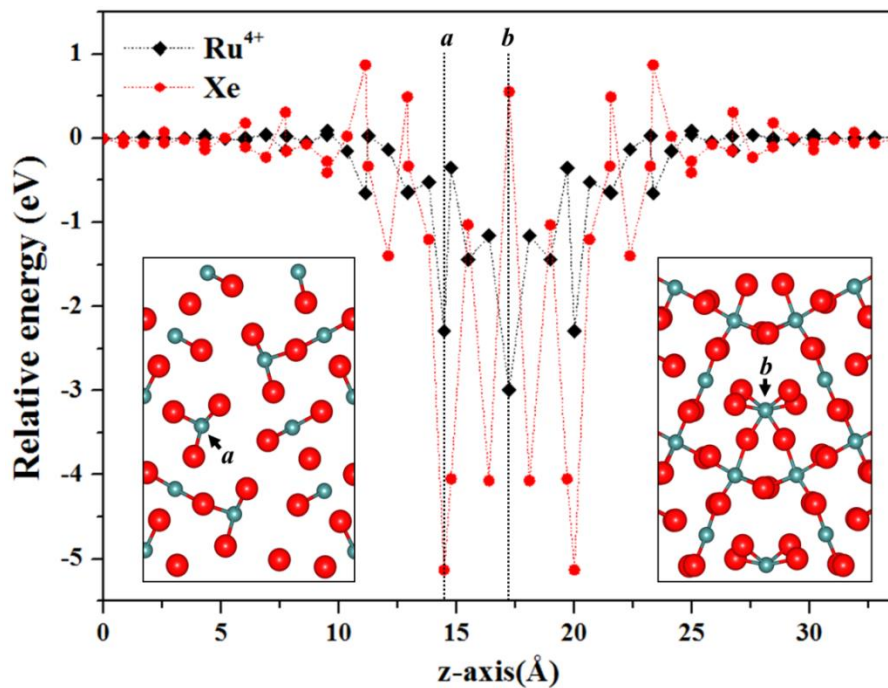


Figure 3-7. The energy profiles of Xe and  $\text{Ru}^{4+}$  across the grain boundary; the inset images are the projections of the uranium layer of the *a*- and *b*-site, with the neighboring two oxygen layers.

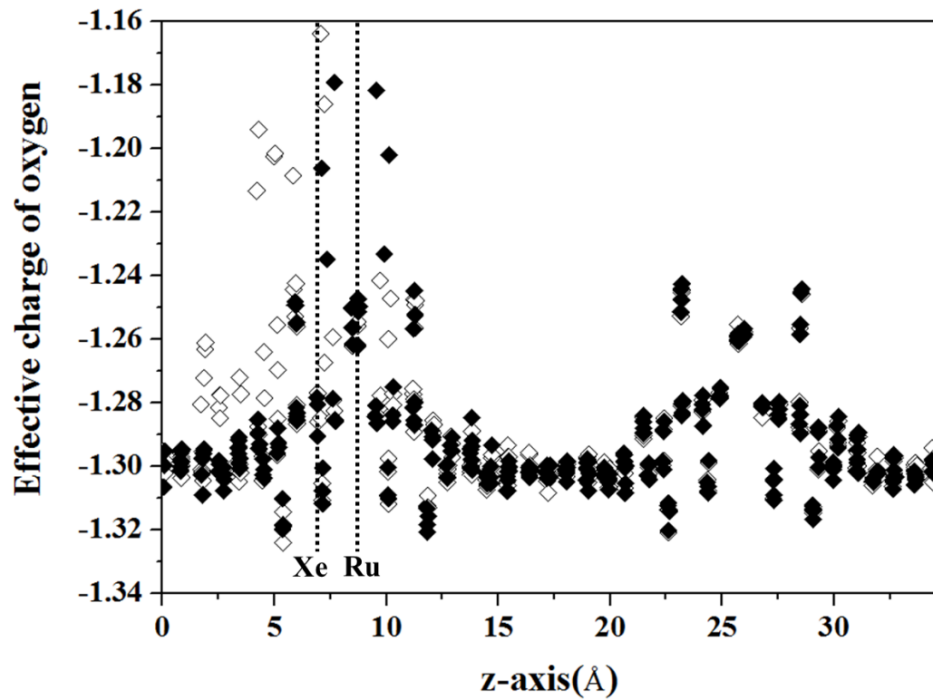


Figure 3-8. Effective charges of all oxygen ions for both Xe (open) and Ru (closed) cases; the positions of segregates are indicated with dashed lines.

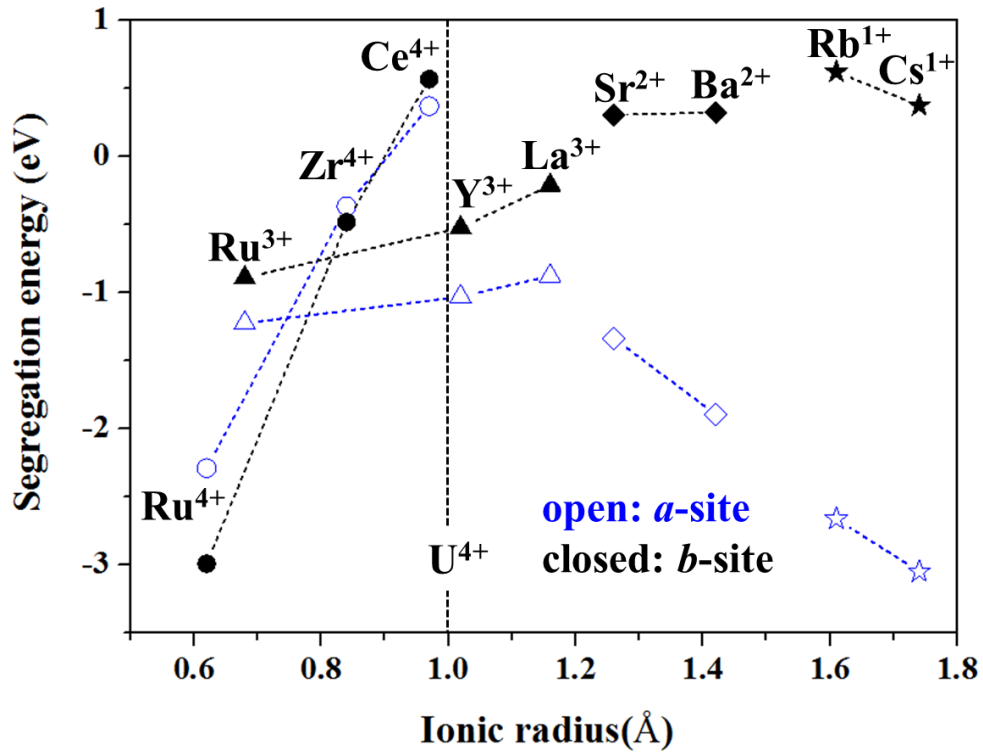


Figure 3-9. Segregation energies of cation fission products at *a*- and *b*-site

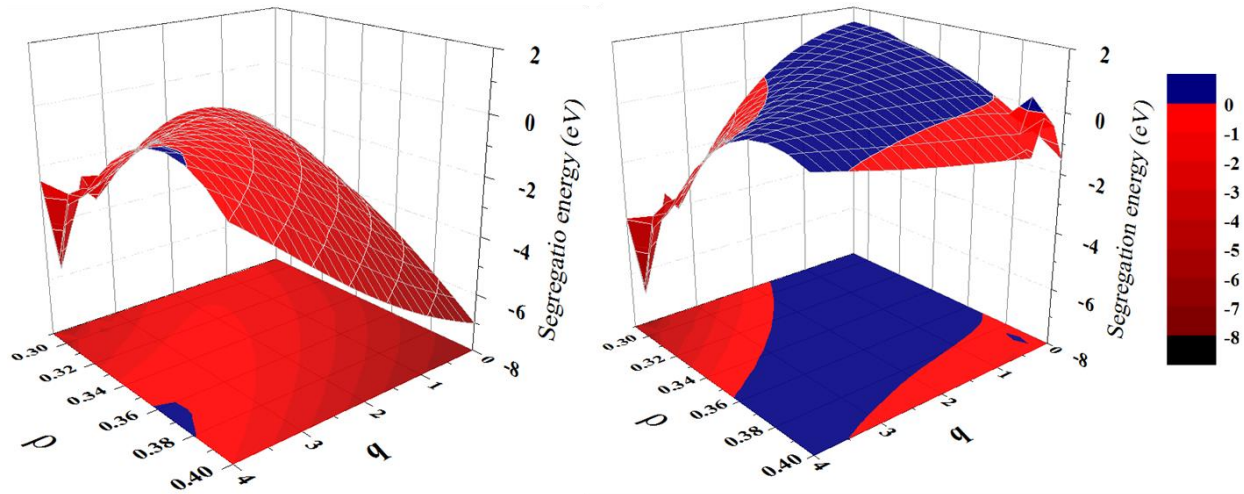


Figure 3-10. Segregation energy contour for the *a*-site (left; a singularity found using the GULP has been replaced by the value from other in-house codes) and the *b*-site (right); blue indicates where segregation is unfavored.

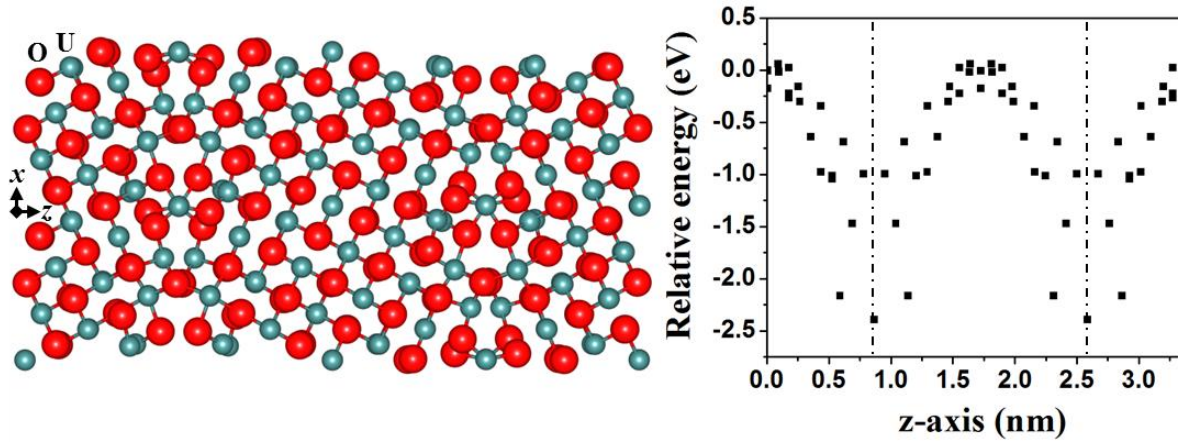


Figure 3-11.  $\Sigma 5(310)/[001]$  tilt grain boundary of  $\text{UO}_2$ : the relative energy profile of Cr obtained by empirical potentials along the direction perpendicular to the grain boundary (dashed lines indicate where the grain boundaries are). U is the small blue-gray atom and O is large red atom.

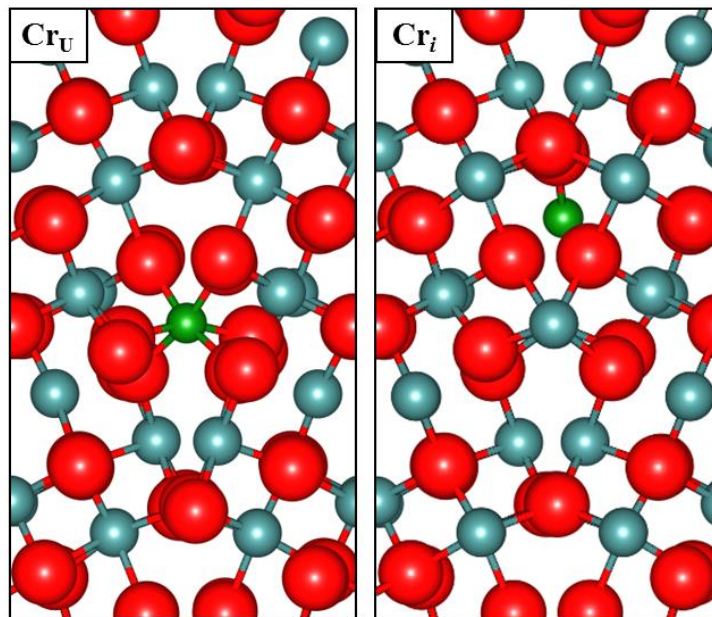


Figure 3-12. Cr-doped grain boundary: Cr at uranium site (left) and Cr at interstitial site (right). Cr is the small green atom.

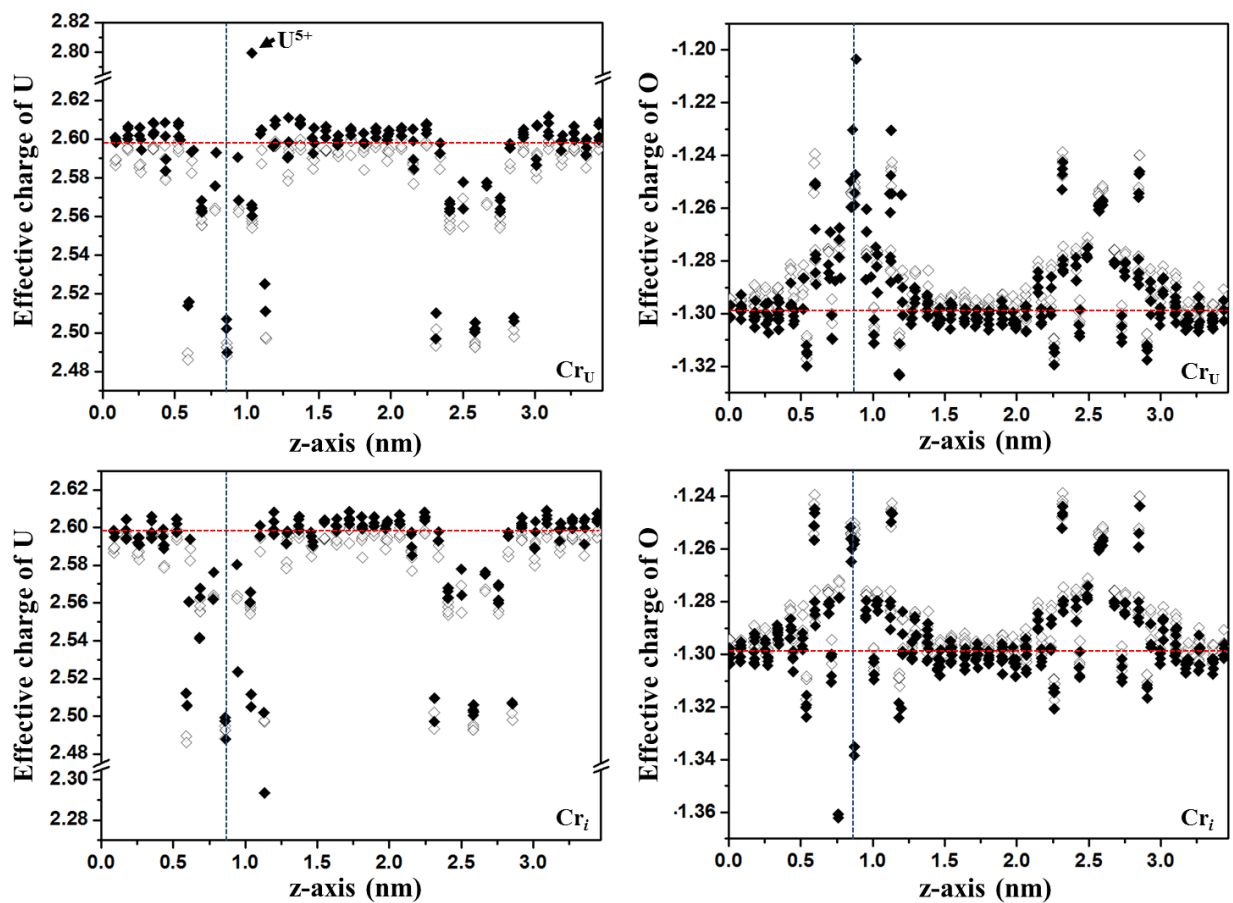


Figure 3-13. Bader charges of uranium and oxygen for  $Cr_U$  (upper) and  $Cr_i$  cases (lower). The blue vertical line indicates the position of the Cr segregation site while the red horizontal line indicates values of the Bader charges for atoms in bulk  $UO_2$ ; open data points correspond to the pristine grain boundary with no added Cr.

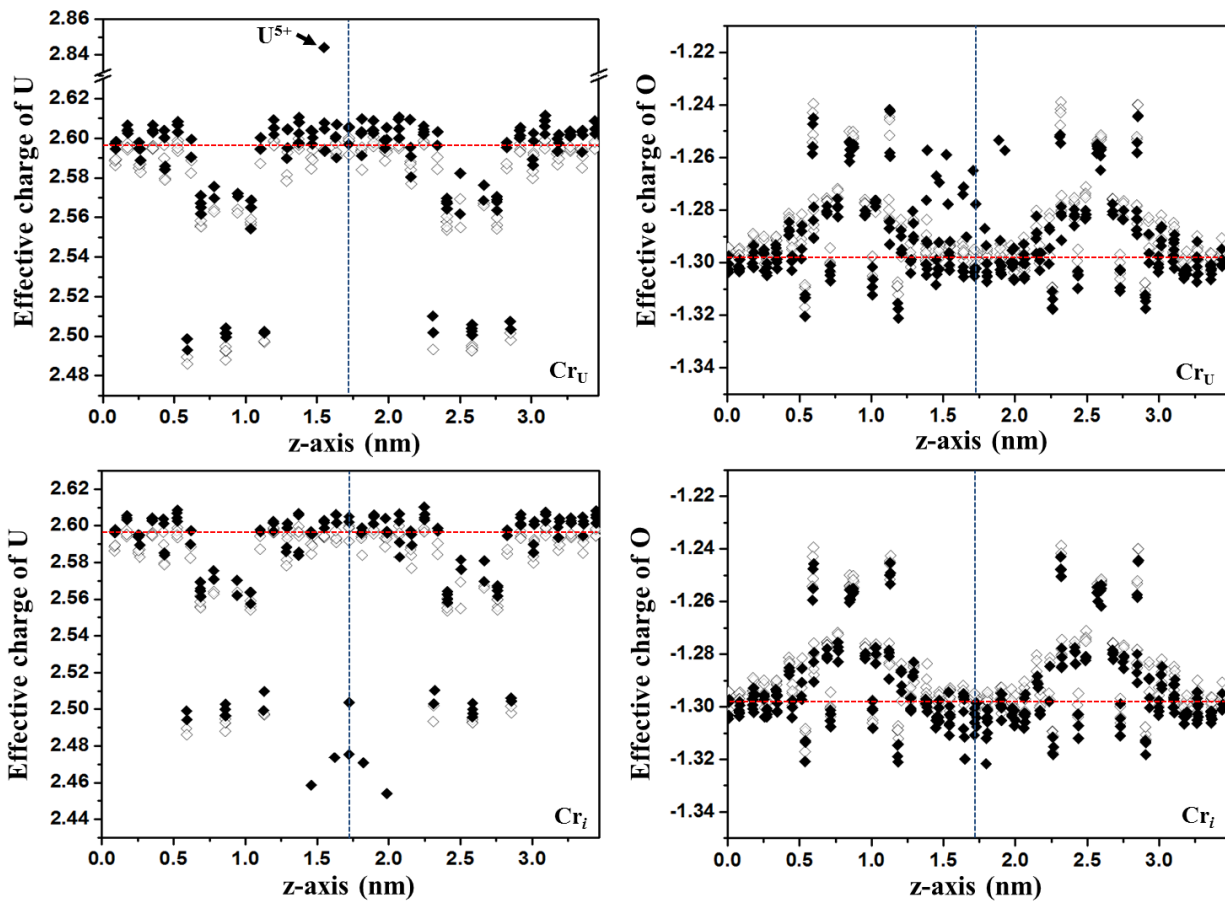


Figure 3-14. Bader charges of uranium and oxygen for the case that Cr is added in the bulk region. Details are the same with Figure 3-13.

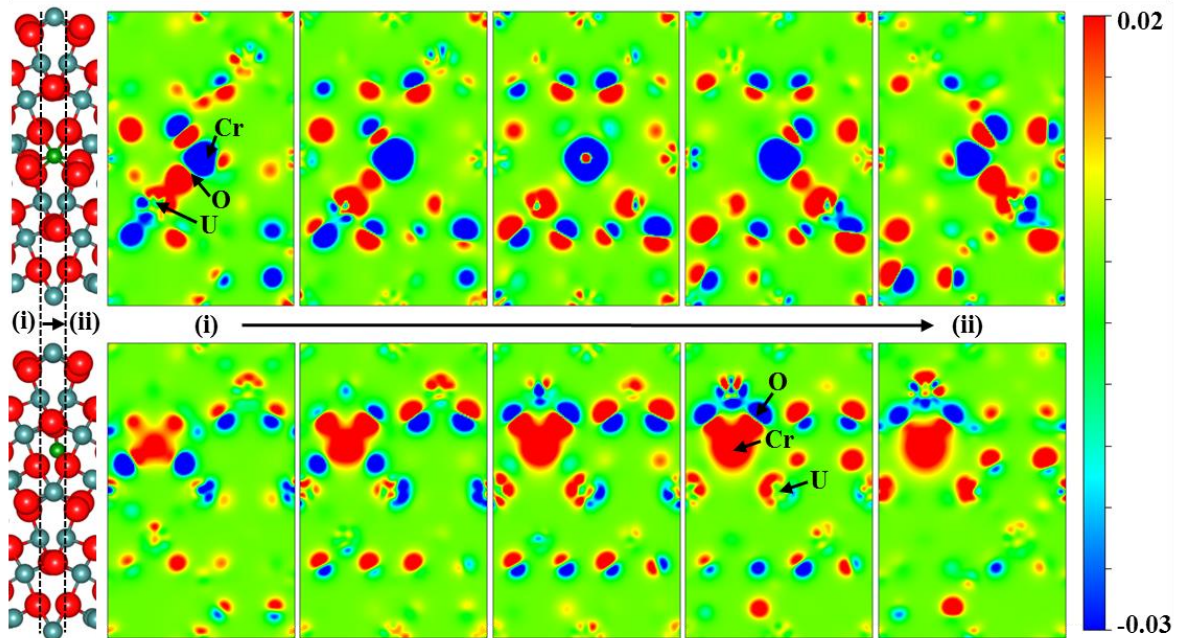


Figure 3-15. Charge density difference for  $Cr_U$  (upper images) and  $Cr_I$  (bottom images); the images are equally bisected from (i) to (ii) to illustrate the 2-D projections within the plane of the grain boundary.

## CHAPTER 4 SURFACE DIFFUSION ON SrTiO<sub>3</sub> (100)

Temperature accelerated dynamics (TAD)<sup>44</sup> is used to predict the mechanisms involved in the surface diffusion of different adatoms and vacancies associated with the growth of STO on the (100) STO surface. The results are complementary to the predictions of traditional MD methods<sup>35-37</sup> and offer additional insight into the growth modes of STO thin films. They are also in qualitative agreement with density functional theory (DFT) calculations, though significant charge transfer effects occur in some cases that result in behavior not describable with the empirical potential.

### Computational Details

The atomic interactions within the system are described using a traditional pair potential described in the previous chapter. The potential parameters used in this study are from Sekiguchi *et al.*<sup>167</sup> The Ewald<sup>168</sup> method was used for the Coulombic summation though tests with the Wolf<sup>169</sup> and the Parry<sup>170</sup> methods resulted in similar behavior.

STO (100) has two equilibrium terminations: SrO and TiO<sub>2</sub>. Therefore both of these surfaces are considered in this work. Each STO substrate consists of 6 planes (3 SrO and 3 TiO<sub>2</sub>) with the bottom 2 (DFT) or 3 (TAD) planes frozen and with a vacuum spacing in the slab geometry of ~17.4 Å (see Figure 4-1), containing 135 (DFT) and 540 (TAD) atoms. We examined both adatoms and surface vacancies. While surface vacancies in the film (not in the substrate) are less important at the initial stages of growth, when the growth of full monolayers nears completion the system is best viewed as containing surface vacancies. Thus, for completeness, we evaluate the migration behavior of these species as well. To determine the mechanisms involved in adatom

surface diffusion, one Sr/O/Ti atom was placed atop each STO (001) surface. Multiple adsorption sites were used as the starting position but this was found to be unimportant for the observed behavior, since each possible adsorption site was either the lowest energy state or an intermediate state (IS) found during the TAD simulations; that is, all possible states were visited during the course of a given TAD simulation. To examine surface vacancy diffusion, a single Sr/O/Ti atom was removed from the surface. For an improved assessment of the energetics found by TAD (and thus described by an empirical potential), Sr and O adsorption on SrO-terminated surface was examined by density functional theory (DFT) calculations. All DFT calculations, as implemented in the VASP code, were carried out using the PAW method with the GGA functional revised by Perdew, Burke, and Ernzerhof (PBE)<sup>171</sup>. The cutoff energy for plane waves was set to 550 eV and a 3×3×1 *k*-mesh was used.

## **Results and Discussion**

### **Diffusion Mechanism Predicted by TAD Simulations**

The diffusion behavior and barriers predicted with TAD using the empirical potential for all the species considered are given in Table 4-1. The results provide insight into the behavior of individual deposited adatoms or surface vacancies on both SrO- and TiO<sub>2</sub>-terminated STO surfaces.

On both terminations, Sr and O diffusion occurred via a simple hopping of those adatoms between the minimum energy sites, although the detailed configurations and the associated diffusion barriers varied with the surface termination. For the SrO termination, the minimum energy site for Sr and O was the bridge site, Br<sub>O,Sr</sub>. It was found that Sr and O diffused from a minimum energy site along the [100] direction towards an atop-site (T<sub>Sr</sub> and T<sub>O</sub> respectively) which is an intermediate state, with a

barrier of 0.28 and 0.53 eV, respectively. Therefore, in order to complete a full diffusive event, the Sr and O adatoms need to overcome a second barrier of 0.03 and 0.01 eV, respectively, from the intermediate state back to the ground state absorption site (see Figure 4-2). It is interesting to note that in both of these cases the barrier to leave the higher energy intermediate state is very small and that the intermediate state itself is a good estimate of the migration energy. We will return to this point later.

On the  $\text{TiO}_2$  termination, the minimum energy site for Sr is a hollow four-fold site,  $F_{\text{O}}$ , where Sr can maximize the distance between itself and other surface cations. Sr also diffused along the [100] direction via a hopping mechanism on this surface but the  $T_{\text{O}}$  site was a saddle point with no intermediate minimum; the associated barrier is 1.43 eV, which is relatively high compared to the SrO termination case (see Figure 4-3). This implies that Sr can form stronger bonds with surface O atoms at  $F_{\text{O}}$  on the  $\text{TiO}_2$  termination and become immobile as a consequence. Additionally, Sr can pass through  $T_{\text{Ti}}$  along the [110] direction; however, this occurs with an even higher barrier of 1.92 eV. Similarly, O diffusion occurred from one  $T_{\text{Ti}}$  to another  $T_{\text{Ti}}$  with  $T_{\text{O}}$  as a saddle point and a barrier of 2.27 eV. Therefore one can conclude that Sr and O easily diffuse on the SrO termination while they are essentially immobile on the  $\text{TiO}_2$  terminated surface.

Sr and O vacancy diffusion was also investigated on both terminations and their diffusion barriers determined with the potential. It was found that on the SrO termination, Sr vacancy diffusion occurred via a surface Sr moving in the [100] direction to fill the vacancy with a barrier of 1.11 eV. The O vacancy diffused by first filling the surface vacancy with a sub-surface O (O in sub-surface  $\text{TiO}_2$  plane) overcoming a barrier of 0.90 eV – leading to an intermediate minima with the vacancy in the second layer –

followed by an adjacent surface oxygen filling the newly created sub-surface vacancy, overcoming a second barrier of 0.30 eV (see Figure 4-4). For O vacancy migration on the TiO<sub>2</sub> termination, the lowest energy diffusion mechanism involves an adjacent surface oxygen passing through the surface ([110] direction) to fill the vacancy with a barrier of 0.84 eV.

In contrast to Sr and O species, Ti-containing surface defects – the Ti adatom and the Ti surface vacancy – did not exhibit any net diffusion over the time scales simulated. On the SrO termination, Ti-O bonds were formed by the Ti adatom essentially pulling three surface oxygen ions out of the surface, leaving behind surface vacancies, at least one of which was repelled by the Ti-O complex and diffused away. Thus, the deposition of Ti on the SrO termination leads to the creation of surface oxygen vacancies. This behavior can be compared to a theoretical study of Ni<sup>3+</sup> on NiO which examined the role of the difference in oxidation state of the adatom with the surface cation. In that case, as with our study, Ni<sup>3+</sup> pulls oxygen atoms from the surface and, compared to a Ni<sup>2+</sup> adatom on NiO, has a stronger interaction with the surface<sup>172</sup>. On the TiO<sub>2</sub> termination, the Ti adatom reconstructs the surface by pulling two oxygen atoms out, similar to the SrO termination. The consequent Ti-O complex exhibited a rotating motion associated with oxygen pair exchange, i.e., changing its relative direction against the surface, a mechanism which did not result in net diffusion of species. In the case of the Ti vacancy, complex rearrangements of the surface were observed, but no mobility of the complexes was observed.

These results give insight into the cause of the different growth modes predicted in the previous MD thin film deposition simulations<sup>37</sup>. Layer-by-layer growth is achieved

because deposited species are able to move about the surface in order to complete each layer without in-plane vacancies; this was seen in the MD simulations for SrO thin films as well as the initial STO layer when deposited on the SrO termination. Consistently, the barriers for the diffusion of adatoms on the SrO termination are much lower than on the TiO<sub>2</sub> termination and therefore adatoms are typically mobile on that termination, with the exception of the Ti adatom. The overall immobility of the Ti-containing defects also explains the growth mode observed in previous MD simulations<sup>37</sup> where the TiO<sub>2</sub> incident particles hit the substrate and remained stuck where they landed; such immobility is indicative of a three-dimensional growth mode. Although more evidence is required to obtain a definitive explanation, one possible reason for the difference in adatom mobility between the two terminations is the difference in cation/anion ratio of the two planes. The TiO<sub>2</sub> terminated surface is more anion-rich, containing twice the oxygen present on the SrO termination; therefore cations on the TiO<sub>2</sub> termination can be effectively pinned by surface oxygen atoms. This conclusion is supported by the fact that Ti adatoms interact strongly with surface oxygen on both terminations and are effectively pinned in both cases. Thus, the interaction of cation adatoms with surface oxygen is an important factor governing their mobility.

### **DFT Verification**

The shallow intermediate minimum along the diffusion path on SrO termination discussed above is comparable to Henkelman *et al.*'s findings for MgO ad-dimer diffusion on MgO (001)<sup>173</sup>. In their study, the Mg and O from the ad-dimer were predicted to hop in a manner similar to the Sr and O adatoms on the SrO terminated surface. They also pointed out that the energy state predicted using empirical potentials can be qualitatively different from those found with higher accuracy calculations, such

as density functional theory (DFT). We therefore performed DFT calculations to investigate the predicted diffusion pathways for Sr and O adatoms obtained from the TAD simulations. The total energies of the Sr and O adatoms on both the atop- and bridge-sites on the SrO termination were calculated and the results are given in Table 4-2. It is notable that these adsorption calculations were performed with charge-modified systems instead of neutral systems, i.e., a system with two electrons added for O adatom and with two electrons subtracted for Sr adatom in order to make the charge states of adatoms similar to those in the potential description. The migration energies associated with the diffusion of Sr and O from the higher to the lower energy site were also investigated using the NEB method in order to confirm the second small barrier predicted by TAD.

The DFT saddle points are very close in energy to the higher energy intermediate sites with almost no barriers, in agreement with the predictions from the TAD simulations, and therefore we could appropriately assume the intermediate energy is an estimate of the saddle energy for the entire hopping mechanism from a lower energy site to another lower energy site. The minimum energy site was the bridge-site for both Sr and O adatoms, consistent with the TAD simulations, and the migration energy for the entire hopping event is qualitatively similar to those predicted by the potential. Bader analysis<sup>145, 174</sup> (see Table 4-3) confirmed that the effective charges of the adatoms within the charge-modified systems were quite close to those of atoms in the surface and more importantly, those charges remained invariant to the adsorption site as the fixed charge potential utilized in the TAD simulations. Consequently, the energy trends calculated with DFT for charge-modified systems agree with the fixed-charge potential

simulations. When we used neutral systems, the O migration energy agreed more closely with the prediction of the potential. However, when the effective charge of the Sr adatom was changed from 2+ to 0, the minimum energy site for the Sr adatom changed to  $T_O$ , with  $Br_O$  being an intermediate state with a migration barrier that increased compared to the charged case. In this case, there is also a significant difference in the Bader charge of the Sr adatom with adsorption site, with very little charge transfer occurring in the atop geometry. These results imply that the charge transfer effects must be considered for certain species and that the overall growth mode will depend on the charge state of the adatoms on the surface.

### **Generalization: Other Metal Adatoms**

The results discussed above suggest that, for diffusion on the SrO-terminated surface, the migration energy is, to a high degree of accuracy, simply the difference in energy between the two adsorption sites. Motivated by these conclusions, the adsorption energetics for selected metal elements are examined by DFT; all calculations described here are for neutral species. Specifically, Ti, Ba, La, and Al were placed at both the  $Br_O$  and  $T_O$  sites and the total energy differences were calculated (see Table 4-4). These species were chosen because their diffusion behaviors are important for the growth of other oxide heterostructures on STO surface, such as  $LaAlO_3/SrTiO_3$  and  $BaTiO_3/SrTiO_3$ , that have received significant attention<sup>175-179</sup>. The calculated migration energies of La and Al are significantly smaller than the others studied and this suggests that  $LaAlO_3$  will grow epitaxially at much lower temperatures compared to  $BaTiO_3$  or  $SrTiO_3$ , at least during the very earliest stages of growth. That is, the migration energy calculation can provide a good predictor of the ability to grow epitaxial films on the STO surface, though many other factors are also very important.

However, determining the minimum energy site is not straightforward. The minimum energy adsorption site for Ba and Sr is  $T_O$  and this is related to their electronic configurations; their outermost s-orbital, which is spherical, is fully filled so that the bonding with two O ions at  $Br_O$  is not favorable. On the other hand, Ti, La, and Al have partially filled 3d- or 3p-orbitals which are more directional than the s-orbitals and thus these adatoms tend to form dioxide species by transferring charges to O ions, resulting in  $Br_O$  being the minimum energy site. The resulting surface oxide configuration indicates that the two O ions were pulled out of the surface much more for these ions than the Sr case. In particular, the large migration energy of the Ti adatom ( $\sim 1\text{eV}$ ) implies that the resulting Ti-O bond is strong and thus Ti is immobile on the SrO termination; this is consistent with the observation for the Ti adatom from the TAD simulations discussed above. Therefore charge transfer can be important for the migration of metal adatoms and particularly for determining the minimum energy site within the diffusion path. That is, when charge transfer is small (such as for the O adatom), the empirical potential can predict the lowest energy site properly; however, when charge transfer is large and, especially, variable (metal adatoms), the electronic structure becomes more important and the potentials less reliable.

### **Conclusions**

TAD simulations using the potential of Sekiguchi *et al.* predict that Sr and O adatoms diffuse via a hopping mechanism with a significantly lower barrier on the SrO termination than on the  $TiO_2$  termination of the (100) STO surface, resulting in higher mobility on this surface. However, the Ti defects form Ti-O complexes on both terminations, effectively becoming immobile. These findings are in agreement with a previous molecular dynamics study of SrO and  $TiO_2$  particulate mobility on each

termination<sup>37</sup>, where it was shown that SrO particles are more mobile overall and that mobility was higher on SrO termination compared to TiO<sub>2</sub> termination. The TAD simulations can be effectively used to find candidate mechanisms to be further investigated with DFT to assess charge transfer effects on the mechanism predicted. The DFT calculations reveal that the migration mechanisms are sensitive to the charge state of the adatoms. Finally, these mechanisms can be used as input for additional simulation techniques which model thin film growth on longer time scales.

An important conclusion of this work is that the migration energy for adatoms on the SrO termination is well estimated by the energy differences between the two absorption sites. This allows for a relatively easy evaluation of the mobility of many species on this surface and thus a method for screening compounds that may grow epitaxially on this surface.

Table 4-1. The diffusion mechanisms and barriers (eV) observed during TAD simulations with the Sekiguchi potential

Termination	Species	Mechanism	Primary Barrier (Saddle Point)	Secondary Barrier (Intermediate State)
SrO	Sr	Hopping	0.28	0.03
	O	Hopping	0.53	0.01
	Ti	Ti-O complex	-	-
	V <sub>Sr</sub>	Hopping	1.11	-
	V <sub>O</sub>	Subsurface exchange	0.90	0.30
TiO <sub>2</sub>	Sr	Hopping	1.43 (1.91)	-
	O	Hopping	2.27	-
	Ti	Ti-O complex	-	-
	V <sub>O</sub>	Hopping	0.84	-
	V <sub>Ti</sub>	Surface reconstruction	-	-

Table 4-2. DFT results for Sr and O adsorptions on SrO terminated STO surface compared with the empirical potential results. As discussed in the text, the migration energy (eV) is assumed to be the difference in energy of the species in the two absorption sites; the DFT results with the neutral systems are shown in parenthesis.

Adsorption species	Minimum energy site		Migration energy	
	potential	DFT	potential	DFT
Sr	Br <sub>O</sub>	Br <sub>O</sub> (T <sub>O</sub> )	0.28	0.77 (0.83)
O	Br <sub>Sr</sub>	Br <sub>Sr</sub> (Br <sub>Sr</sub> )	0.53	0.95 (0.64)

Table 4-3. Effective charges of Sr and O adatoms at atop- and bridge-site on SrO terminated STO surface.

System	Sr		O	
	T <sub>O</sub>	Br <sub>O</sub>	T <sub>Sr</sub>	Br <sub>Sr</sub>
charge modified	1.256	1.485	-1.335	-1.433
neutral	0.179	0.704	-0.822	-1.007

Table 4-4. DFT results for selected species on SrO terminated STO surface.

Adsorption species	Minimum energy site	Estimated migration energy (eV)
Ti	Br <sub>O</sub>	1.07
La	Br <sub>O</sub>	0.39
Al	Br <sub>O</sub>	0.06
Ba	T <sub>O</sub>	0.47
Sr	T <sub>O</sub>	0.83

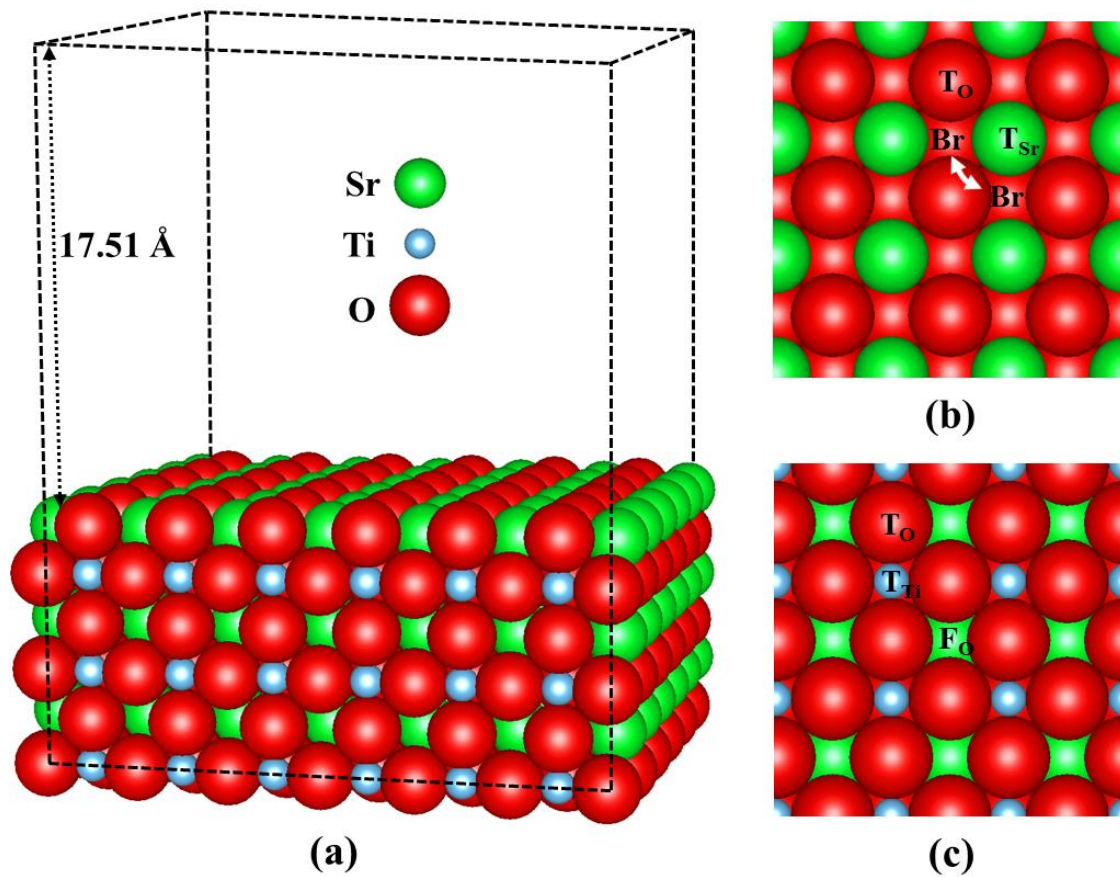


Figure 4-1. (a) A model SrO-terminated STO surface (for TAD) and adsorption sites on both (b) SrO- and (c) TiO<sub>2</sub>-terminations; T, Br, F denote atop, bridge, and hollow four-fold site, respectively. For example, T<sub>O</sub> indicates an atop-oxygen site.

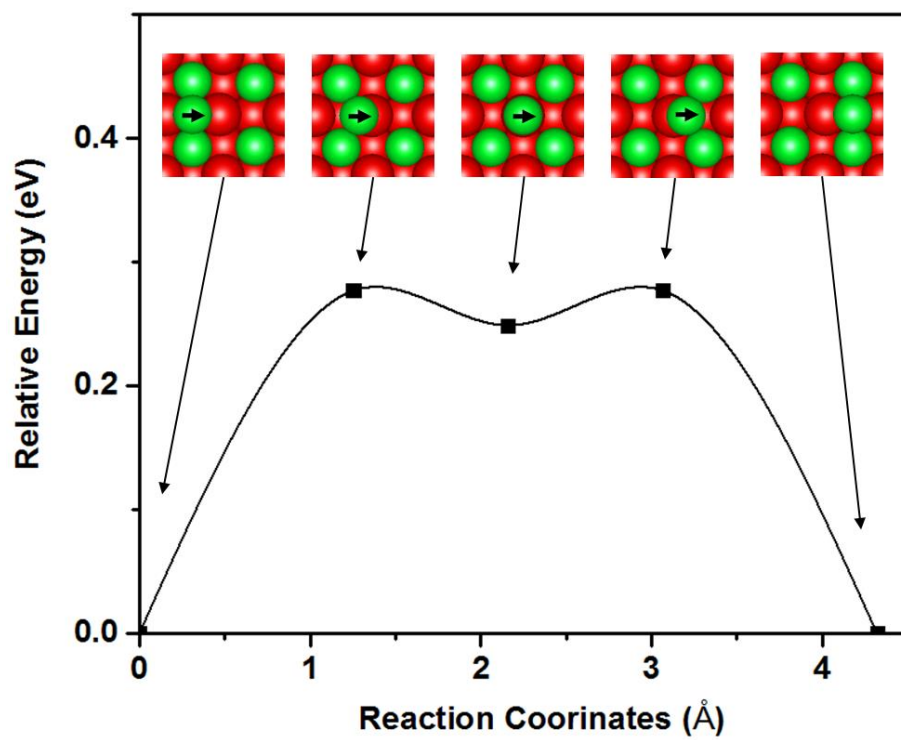


Figure 4-2. The mechanism for Sr migration on the SrO-terminated STO(100) surface.

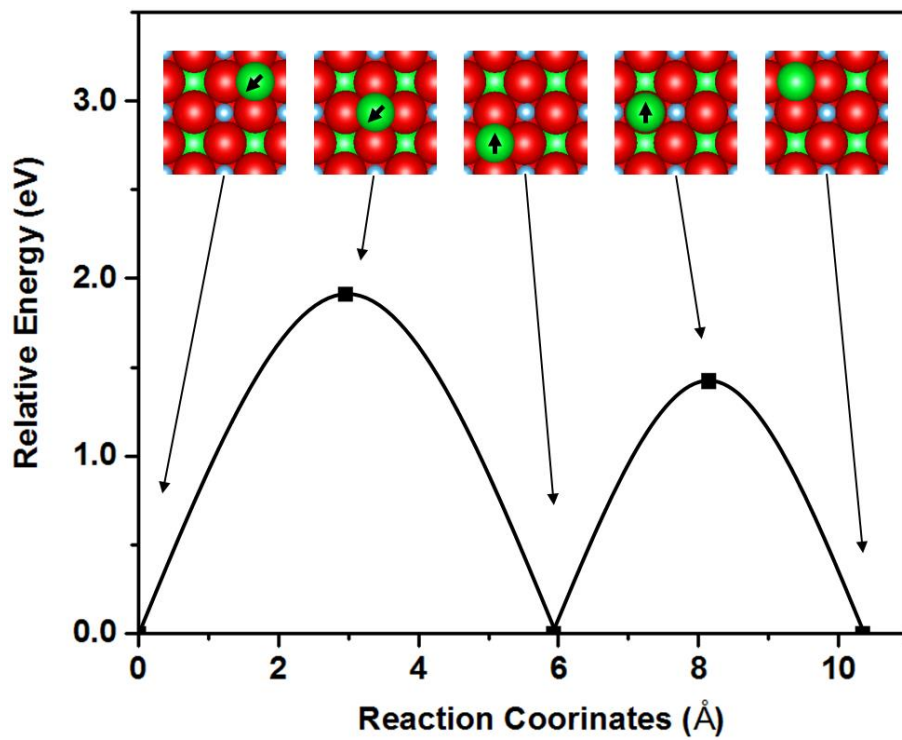


Figure 4-3. The mechanism for Sr migration on the TiO<sub>2</sub>-terminated STO(100) surface.

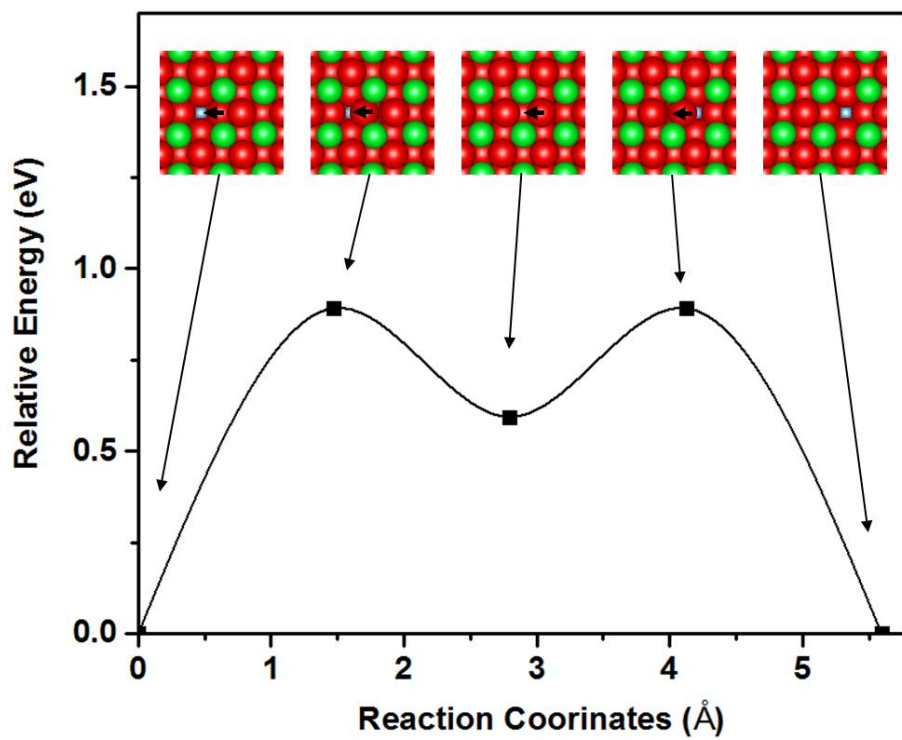


Figure 4-4 O vacancy diffusion on the SrO-terminated STO surface.

## CHAPTER 5 OXIDATION OF TiN (001) STEPPED SURFACE

First principles, DFT calculations are used to investigate O<sub>2</sub> adsorption and dissociation as well as the initial formation of TiO<sub>2</sub> layers on a TiN (001) surface with a monatomic step, which is the most commonly observed stepped structure in thin films<sup>64, 180, 181</sup>. The calculations quantify the energetics associated with O<sub>2</sub> adsorption on and around the step and the results are compared to the energetics associated with the flat surface; two distinct O<sub>2</sub> dissociation paths around the step are explored. Finally, TiO<sub>2</sub> formation along the step edge is explored, which is predicted to take place concurrently with O<sub>2</sub> dissociation.

### Computational Details

Titanium nitride has the rocksalt crystal structure with  $Fm\bar{3}m$  symmetry and a lattice constant of 4.235 Å. The calculations consider two different surfaces: a (2×2) flat TiN (001) surface and a (2×2) TiN (001) surface with a monatomic step. The flat surface is modeled by a plain slab with 64 atoms and two identical (001) surfaces on both top and bottom sides. The stepped surface is modeled by a slab with 168 atoms and is comprised of two identical (310) facets on both sides where the step was along the [001] direction, as illustrated in Figure 5-1. For calculations with oxygen on those surfaces, only the top two layers of either slab are allowed to relax while the other layers are held fixed. The vacuum spacing between slabs imposed by the periodic boundary conditions is 10.63 Å for the flat surface and 13.39 Å for the stepped surface.

The DFT calculations are carried out with the PAW method as implemented in the VASP. Ti3p<sup>6</sup>3d<sup>3</sup>4s<sup>1</sup>, N2s<sup>2</sup>2p<sup>3</sup>, and O2s<sup>2</sup>2p<sup>4</sup> are taken as the valence electrons. The exchange and correlation energies are described with the GGA-PBE. The kinetic energy

cutoff is 400 eV and the Brillouin zone is sampled by a 4×4×1 *k*-mesh. The convergence criterion for the total energy is 1×10<sup>-5</sup> eV and the ionic relaxations are performed until the forces on the atoms became less than 1×10<sup>-2</sup> eV/Å<sup>-1</sup>.

## Results and Discussion

### Adsorption of Atomic and Molecular Oxygen

A preliminary potential energy surface (PES) scan with a single oxygen atom over the flat TiN surface finds that O prefers to adsorb on the near-atop Ti site, while the N atop sites are always predicted to be unfavorable. The adsorption energy calculations for atomic O on both the flat and the stepped surface (see Table 5-1) identify stable adsorption sites; the adsorption energy  $E_a$  is calculated as,

$$E_a = E_{O/TiN\ slab} - E_{TiN\ slab} - \frac{1}{2} E_{O_2(gas)} \quad (5-1)$$

where  $E$  is the total energy of a given system as determined by the DFT calculations;  $E_{O_2/TiN\ slab}$  is the energy of the TiN slab with the adsorbed O atom,  $E_{TiN\ slab}$  is the energy of the bare TiN slab, and  $E_{O_2}$  is the energy of a single O<sub>2</sub> molecule. According to this definition, a negative  $E_a$  indicates that the adsorption reaction is endothermic. The flat surface has two adsorption site, atop Ti and Ti-Ti bridge, while the stepped surface three, denoted as **b**, **t**, and **e**, respectively, in Figure 5-1. Unlike the flat surface, the Ti-Ti bridge site on the terrace of the stepped surface is not stable.

Previous O<sub>2</sub> adsorption studies on a flat TiN (001) surface with first-principles molecular dynamics (FPMD) reported that the O<sub>2</sub> molecule prefers to interact in a parallel manner with the surface<sup>50, 56</sup> and this was also confirmed in our preliminary tests. Consequently, only the horizontal O<sub>2</sub> configuration is considered here. Many initial

configurations are investigated and the results indicate that O<sub>2</sub> prefers adsorption sites that are similar to those preferred by atomic O. Specifically, the four most favorable adsorption sites are **b**, **t**, **e**, and **t-e** and the adsorption energies at each site are shown in Figure 5-2.

Among the four adsorption sites on the stepped surface, the lowest energy configuration is for the **b** site, where O<sub>2</sub> adsorbs parallel to the step edge and shares two Ti atoms. It is notable that the adsorption energy of O<sub>2</sub> at the **t-e** site, which is equivalent to the Ti-Ti bridge site on the flat surface, is smaller than that of O<sub>2</sub> at the **t** and **e** site (atop Ti site) while the opposite trend is predicted on the flat surface. On the flat surface, the adsorption energy of O<sub>2</sub> at the Ti-Ti bridge site (-3.31 eV) is larger than that of the atop Ti site (-3.14 eV), i.e., the Ti-Ti bridge site is more favored. This is possibly due to a geometric constraint, because even when O<sub>2</sub> is adsorbed at the **t** and **e** sites, which can be thought of as atop single Ti atom sites that are not quite at the very edge of the step, it is always aligned parallel to the step [001] direction as it was at **b** site. It is interesting that this geometric molecular alignment occurs regardless of the initial orientation of the molecule and is a unique feature of the stepped surface. A similar effect was reported for O<sub>2</sub> on a Pt (111) stepped surface<sup>67</sup> using scanning tunneling microscopy and DFT calculations.

Several first principles studies predict that when O<sub>2</sub> adsorbs on a metal surface, it transforms into a nonmagnetic “peroxo” state, or O<sub>2</sub><sup>2-</sup>. This change is mainly attributed to charge transfer from the surface to the adsorbed O<sub>2</sub> that fills the π\* anti-bonding orbitals of O<sub>2</sub>, i.e., the O<sub>2</sub> can be thought of as being chemisorbed to the surface<sup>182</sup>. To

investigate if O<sub>2</sub> adsorption on the stepped TiN surface occurs via a similar process, we analyze charge transfer via the differential charge density, which is defined as,

$$\Delta\rho(\mathbf{r}) = \rho_{O_2/TiN\ slab}(\mathbf{r}) - \rho_{O_2}(\mathbf{r}) - \rho_{TiN\ slab}(\mathbf{r}) \quad (5-2)$$

for the adsorbed O<sub>2</sub> molecules. The isosurface, which is illustrated in Figure 5-3, clearly indicates charge transfer from the surface to O<sub>2</sub>. In particular, the ring shape of the yellow region in the figure confirms that the  $\pi^*$  orbital of the adsorbed O<sub>2</sub> molecule is fully filled, i.e., the magnetic moment is fully quenched (O<sub>2</sub><sup>2-</sup>) during the adsorption. Consequently, the O-O bond length ( $d_{O-O}$ ) increases to about 1.45 Å, as shown in Figure 5-2, which is similar to the behavior of adsorbed O<sub>2</sub> on several metal surfaces<sup>182, 183</sup>. For example, Gross *et al.* reported that this O<sub>2</sub> “peroxo” state is a necessary step, or a precursor, for further O<sub>2</sub> dissociation<sup>184</sup>. If more electrons start to fill the  $\sigma^*$  anti-bonding O<sub>2</sub> orbital, the O-O bond length quickly increases further until the molecule dissociates.

## O<sub>2</sub> Dissociation

Two distinct O<sub>2</sub> precursors, O<sub>2</sub> at the **b** and **t** site, are chosen as the initial stage for further dissociation to the lowest energy configuration for the dissociated O atoms to fully explore the energetics and barriers associated with dissociation. These are determined using DFT and the climbing nudge elastic band (cNEB)<sup>185</sup> method. The O<sub>2</sub> precursor at the **e** site was excluded because the calculations predict that O<sub>2</sub> at the **e** site relaxes into molecular adsorption at the **b** site with a small barrier of 0.14 eV. Once the O<sub>2</sub> precursor dissociates, the resulting two oxygen atoms are predicted to spontaneously separate from one another and interact more strongly with the surface. As discussed in the previous section, the **b** site is the most favored and stable

adsorption site for atomic O on the stepped TiN surface and thus it is reasonable to assume that the dissociated O atom will be preferentially adsorbed at these sites. Total energy calculations for several different configurations of two dissociated O atoms were carried out and the results confirmed that the lowest energy configuration was found when the two dissociated O atoms adsorbed at equivalent **b** sites that are evenly spaced along the step, as shown in Figure 5-4. Interestingly, the total energy of this configuration is around 5 eV lower than those configurations with adsorbed O<sub>2</sub> precursors, and this energy drop is almost double the decrease that is predicted to occur on O<sub>2</sub> dissociation and relaxation on a flat TiN surface<sup>57</sup>. This result is consistent with literature findings for other dissociation processes that find that surface steps are more reactive than terraces.

Taking this lowest energy configuration as the final state for the O<sub>2</sub> dissociation, the dissociation barriers for the two O<sub>2</sub> precursors, at the **b** and **t** sites, are calculated along the paths denoted in Figure 5-4. The resulting barrier for the O<sub>2</sub> precursor at site **b** is predicted to be high (1.54 eV), which is attributed to the fact that the O<sub>2</sub> precursor interacts with two Ti atoms; this makes it especially difficult to detach one of the O atoms. In contrast, the barrier for the O<sub>2</sub> precursor at **t** is predicted to be almost zero, which is indicative of spontaneous O<sub>2</sub> dissociation; the resulting energy release following dissociation is predicted to be a maximum of 5.34 eV. Similar dissociative O<sub>2</sub> adsorption has been reported in other studies on several different material surfaces, including TiN<sup>50, 182, 183</sup>.

### **TiO<sub>2</sub> Formation**

In Figure 5-2, the Ti atom under the O<sub>2</sub> precursor at **t** site protrudes slightly into the vacuum more than the other atoms around it. This Ti protrusion at the **t** site is more

obvious than at other sites, i.e., the distance between the surface and the Ti atom beneath the O<sub>2</sub> precursor,  $d_z$ , at the  $\mathbf{t}$  site is longer than other comparable distances. Moreover, during spontaneous O<sub>2</sub> dissociation at site  $\mathbf{t}$ , the calculations predict that the surface Ti atom is initially pulled out towards the step edge by the dissociating O atoms and then returns to its original position at the surface while the O atoms complete their dissociation at the step edge.

Motivated by these results, a TiO<sub>2</sub> formation reaction is investigated that accompanies a spontaneous O<sub>2</sub> dissociation reaction, as illustrated in Figure 5-5. In the proposed reaction, the Ti atom beneath the O<sub>2</sub> precursor at site  $\mathbf{t}$  is completely pulled out of the surface during the molecular dissociation and forms a linear O-Ti-O complex with dissociated O atoms at the step, leaving behind a Ti vacancy at the  $\mathbf{t}$  site. The barrier associated with this formation reaction is predicted to be 0.64 eV and the transition state is close to the initial state (O<sub>2</sub> precursor at the  $\mathbf{t}$  site). Piskanec *et al.* suggested that a linear -O-Ti-O-Ti- chain formation after the initial O<sub>2</sub> adsorption atop Ti atom on the flat TiN (001) surface is mainly attributed to the tendency of Ti to reduce its oxidation state by sharing O atoms with less coordinated neighboring Ti atoms<sup>50</sup>. Similarly, the effective charge of the Ti by Bader charge analysis<sup>145, 174</sup> confirms that the Ti charge is reduced from +1.98e (after the O<sub>2</sub> adsorption at the  $\mathbf{t}$  site) to +1.90e (after TiO<sub>2</sub> formation at the step edge), although the coordination numbers of Ti on the stepped surface are completely different from the flat surface. The total energy of the final state is quite low and only 0.55 eV slightly higher than that of the lowest energy configuration after the spontaneous O<sub>2</sub> dissociation. This implies that the TiO<sub>2</sub> formed at the step is exceptionally stable.

To further investigate the stability of  $\text{TiO}_2$  at the step, the barrier needed to return the Ti atom to the  $t$  site is calculated and predicted to be 2.27 eV. It is therefore reasonable to conclude that once  $\text{O}_2$  dissociation occurs at the step edge, it is difficult to form a  $\text{TiO}_2$  complex to further oxidize the TiN surface. However, if the  $\text{O}_2$  molecule has enough energy to overcome the barrier of 0.64 eV for pulling Ti out of the surface upon its arrival on the terrace site near the step edge, such as from thermal or kinetic energy, Ti-N debonding can occur along with  $\text{O}_2$  dissociation to form a  $\text{TiO}_2$  complex, which creates a Ti vacancy on the terrace site. This vacancy therefore might play as an exit channel for the nitrogen, which is essential for further oxidation of the TiN surface<sup>57</sup>.

### Conclusions

The adsorption and subsequent dissociation and reaction of  $\text{O}_2$  on a monoatomic TiN (001) stepped surface is investigated and compared to comparable behavior of the flat surface. When  $\text{O}_2$  molecules adsorb on or around the step, they are predicted to transition into nonmagnetic “peroxo” molecular precursors before dissociating into atomic oxygen. The energy dissipated from the adsorption and dissociation of  $\text{O}_2$  on the stepped surface is predicted to be substantially larger (~3.2 eV and ~5.3 eV, respectively) than on the flat TiN surface. In particular, when  $\text{O}_2$  adsorbed atop Ti on the terrace near the step edge, it can be either spontaneously dissociated towards the step edge by itself or form a  $\text{TiO}_2$  at the step edge with the Ti atom on which it resides. The barrier for this  $\text{TiO}_2$  formation is calculated to be 0.64 eV and the final state is predicted to be energetically stable. This implies that the oxidation of TiN surface may occur preferentially along the step edge upon  $\text{O}_2$  adsorption in a manner that is similar to the oxidation of some metal surfaces<sup>182</sup>.

Table 5-1. Predicted adsorption energies for atomic O on the flat and stepped TiN surfaces.

Adsorption site	$E_a$ (stepped)	$E_a$ (flat)
<i>Ti-Ti bridge</i>	unstable	-2.40
<i>t</i>	-3.11	-3.26
<i>e</i>	-3.30	-
<i>b</i>	-4.34	-

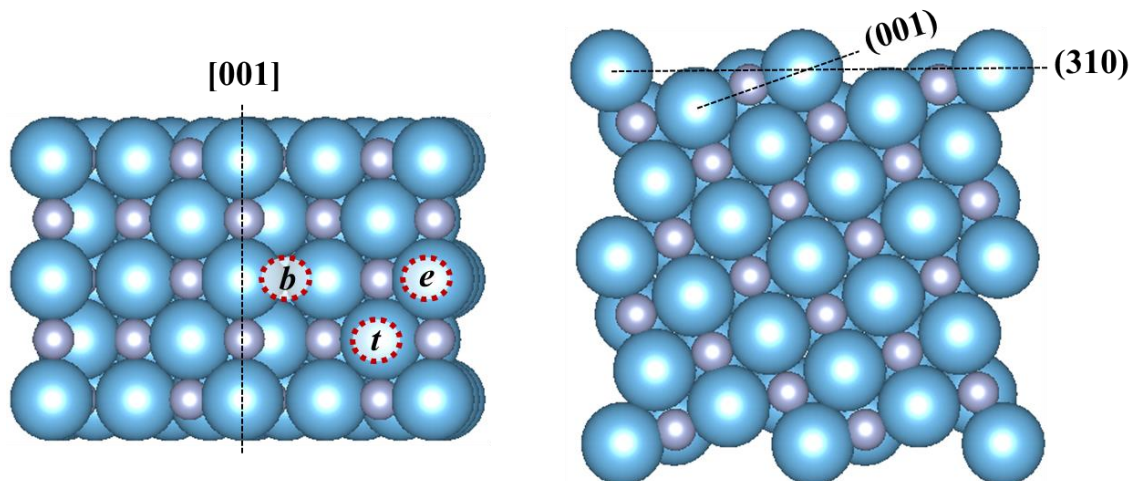


Figure 5-1. The TiN (001) surface with a monatomic step and the three stable adsorption sites (denoted as b, t, and e) for atomic O rendered in top (left) and side (right) views.

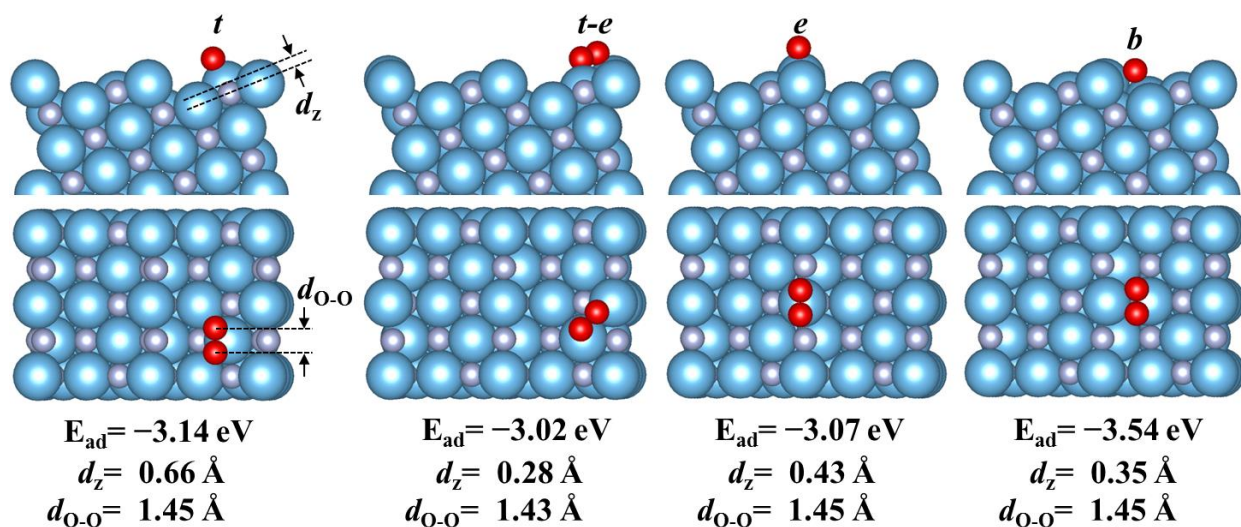


Figure 5-2. Predicted adsorption energies for molecular oxygen on the stepped TiN surfaces. Also shown are the distance between the surface and the Ti atom on which the oxygen resides,  $d_z$ , and the distance between the oxygen atoms,  $d_{O-O}$ .

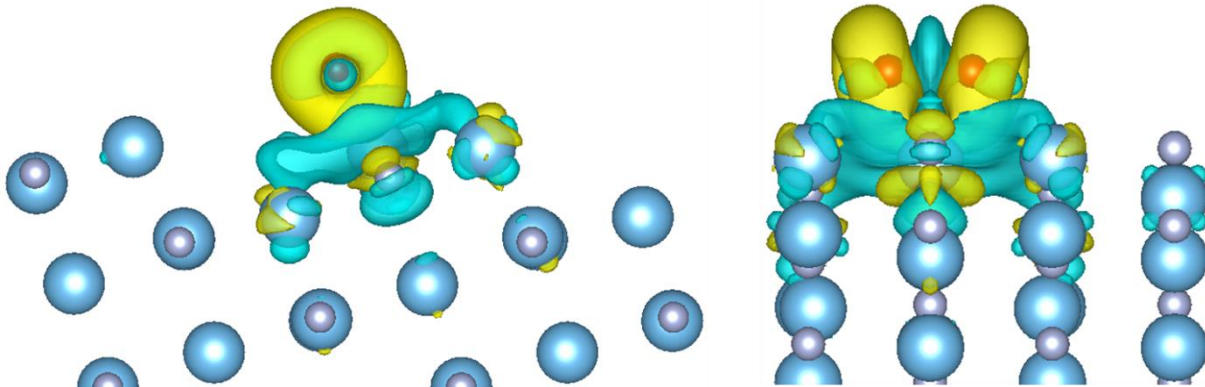


Figure 5-3. The differential charge density of the  $O_2$  precursor at the  $t$  site. The blue region on the surface under the  $O_2$  molecule indicates a decreased charge density and the yellow region around the  $O_2$  molecule indicates an increased charge density.

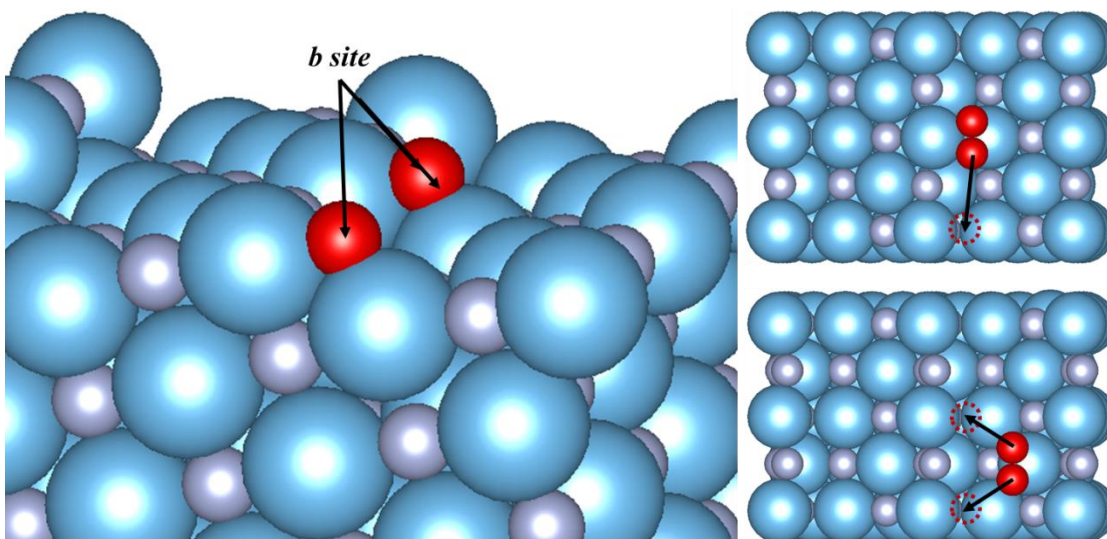


Figure 5-4. The lowest energy configuration of dissociated O atoms (left) and the estimated dissociation paths for  $O_2$  precursor at the  $b$  and  $t$  sites (right).

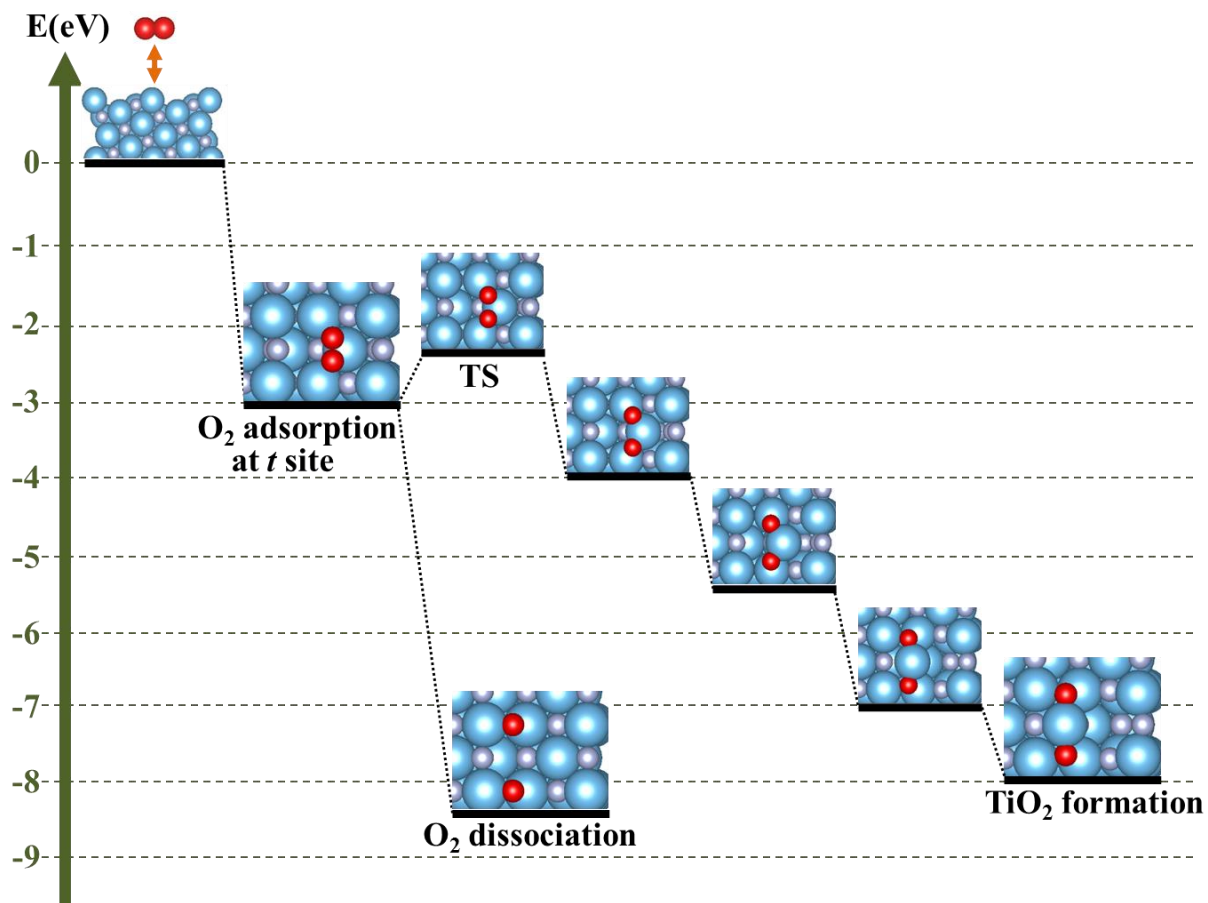


Figure 5-5.  $\text{TiO}_2$  formation associated with the dissociation of  $\text{O}_2$  precursor at  $t$  site

## CHAPTER 6 GENERAL CONCLUSIONS

Understanding the behavior of fission products has always been of utmost importance because these products directly affect the performance of the nuclear fuel. Thus numerous studies have been carried out on the accommodation of gaseous fission products using experimental and computational methods. However, the accommodation of metallic inclusions has not been as thoroughly investigated. Therefore the solubility of Ru, one of the fission products that takes the form of metallic inclusions, and its clustering behavior in  $\text{UO}_2$  were explored using DFT. The computational systems successfully modeled Ru behavior observed in experiments on  $\text{UO}_2$ . To develop this understanding on a larger scale, the interaction between fission products and structural defects in  $\text{UO}_2$  was considered. In experiments, it is known that the grain boundary of  $\text{UO}_2$  is normally decorated with many fission products. Thus the segregation energies of fission products to a model grain boundary were calculated using empirical potentials. The results confirmed that the site, ionic radius and charge state are critical to determine the segregation preference. Also, the charges of segregated fission products are predicted to affect the charge state of the host materials and consequently promote another intrinsic defect. These results provided insight into how doping might be used to control fission product segregation and precipitation in actual fuels through optimization of the microstructure of the  $\text{UO}_2$  pellets. Because Cr is used a grain enlarging dopant in  $\text{UO}_2$  pellet preparation, Cr segregation and its effects on the host material were also investigated. The results confirmed that Cr is accommodated near a model grain boundary can weaken the ionic nature of

neighboring U-O bonds. This explains how enhanced cation mobility would enhance  $\text{UO}_2$  grain growth.

Many material applications and associated properties are related to the response of materials surfaces. In this work, molecular dissociation, atomic adsorption, and atomic transport on  $\text{SrTiO}_3$  (001) and TiN (001) surfaces were considered. For  $\text{SrTiO}_3$ , obtaining an atomically smooth surface during the growth of  $\text{SrTiO}_3$  films is important. Therefore diffusion mechanisms of many ad-species were investigated using TAD. The results predicted that Sr and O adatoms diffuse via a hopping mechanism with a significantly lower barrier on the SrO termination than on the  $\text{TiO}_2$  termination of the (100) STO surface, resulting in higher mobility on this surface. However, the Ti defects form Ti-O complexes on both terminations, effectively becoming immobile. More importantly, it is found that the TAD simulations can be effectively used to find candidate migration mechanisms for ad-species with supportive DFT calculations, and these migration mechanisms can be used as input for additional longer time scale simulations on thin films.

For TiN, surface oxidation is not fully understood especially at the atomic scale despite of the fact that it is the critical degradation of the TiN film. Because only flat TiN surfaces have been investigated so far with first-principles calculations, the TiN surface with a monatomic step was examined. The adsorption and subsequent dissociation of  $\text{O}_2$  on the stepped TiN surface were predicted to release large amount of energy compared to those reactions on the flat surface. In particular, when  $\text{O}_2$  adsorbed atop Ti on the terrace near the step edge, it can be either spontaneously dissociated towards the step edge by itself or form a  $\text{TiO}_2$  at the step edge with the Ti atom on which it

resides. This implies that the oxidation of TiN surface may occur preferentially along the step edge upon O<sub>2</sub> adsorption, which has not been reported experimentally yet.

In summary, the contributions of the work reported in this dissertation to the literature provide an improved understanding of several phenomena. These include: impurity interaction with point and structural defects within UO<sub>2</sub>, a detailed description of surface diffusion for ad-species on SrTiO<sub>3</sub> (001) as well as an evaluation of methodologies for finding optimal migration paths, and a prediction of surface reactions of O<sub>2</sub> on stepped TiN (001) to produce TiO<sub>2</sub> that were not previously known. These phenomena were investigated using atomic-scale and first-principles computational methods that are able to provide insights that are complementary to experimental data.

## APPENDIX HOW TO CONSTRUCT GRAIN BOUNDARIES

The  $\Sigma 5(310)/[001]$   $\theta=36.9^\circ$  symmetric tilt grain boundary examined in Chapter 3 makes use of coincident site lattice (CSL)<sup>146</sup> theory and, is constructed according to the following procedure:

1. Obtain an initial grain boundary structure using the GBstudio software package
2. Remove atoms at the grain boundary that are spatially very close to each other while maintaining the stoichiometry (neutrality) of the structure
3. Perform energy optimization of the structure using the GULP software package
4. Calculate the grain boundary energy of the optimized structure with GULP for an atomic-scale empirical result, or the VASP software package for an electronic-structure DFT result
5. Repeat 2-4 until the grain boundary energy reaches a minimum value

Figure A-1 illustrates the initial  $\Sigma 5$  grain boundary obtained from GBstudio. It consists of 1920 atoms (640U 1280O) with two mirrored grain boundaries; an example of the spatially close U-U and O-O pair at the grain boundary is denoted as white. There are 16 U-U and 32 O-O pairs in total, which are spatially close, and the half of them must be removed prior to structural optimization. Among many ways of removal of atoms, two examples are shown in Figure A-2 and the corresponding grain boundary structures after structural optimization are given in Figure A-3. After optimization, the grain boundary energy,  $E_{GB}$ , for the optimized structure is calculated as:

$$E_{GB} = \frac{E_{total} - E_{total}^{GB}}{2A} \quad (A-1)$$

where  $E_{total}$  is the total energy of pristine bulk  $UO_2$  containing the same number of atoms as the grain boundary structure,  $E_{total}^{GB}$  is the total energy of the optimized grain

boundary structure, and  $A$  is the grain boundary area; the calculated grain boundary energies for the (a) and (b) cases are  $0.195 \text{ eV}/\text{\AA}^2$  and  $0.214 \text{ eV}/\text{\AA}^2$ , respectively. By repeating these procedures, the lowest grain boundary structure can be found, and subsequently used to examine fission product segregation and Cr incorporation, as detailed in Chapter 3.

Using the same grain boundary construction method, other CSL grain boundaries of  $\text{UO}_2$  (from  $\Sigma 3, 7, 9$  and  $11$ ) were modeled and their segregation energy profiles for a selected fission product ion,  $\text{Ru}^{4+}$ , were also obtained. The results are shown in Figures A-4-7.

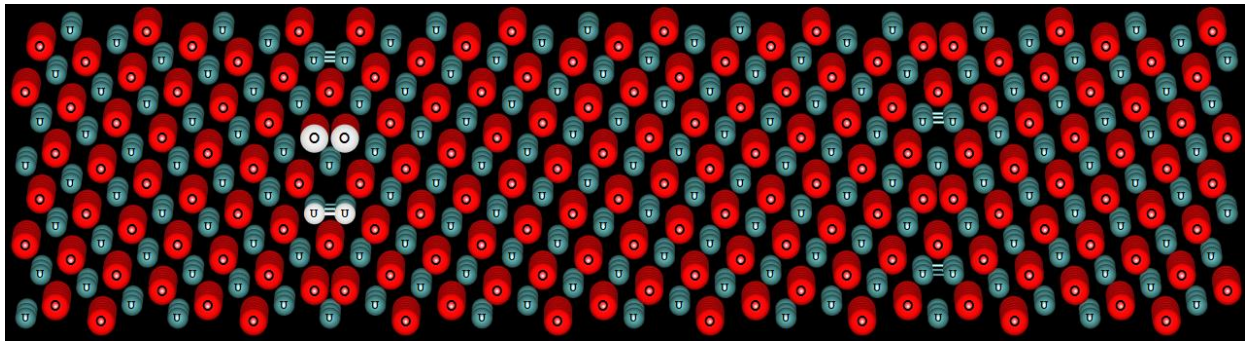


Figure A-1. The initial  $\Sigma 5$  grain boundary of  $\text{UO}_2$

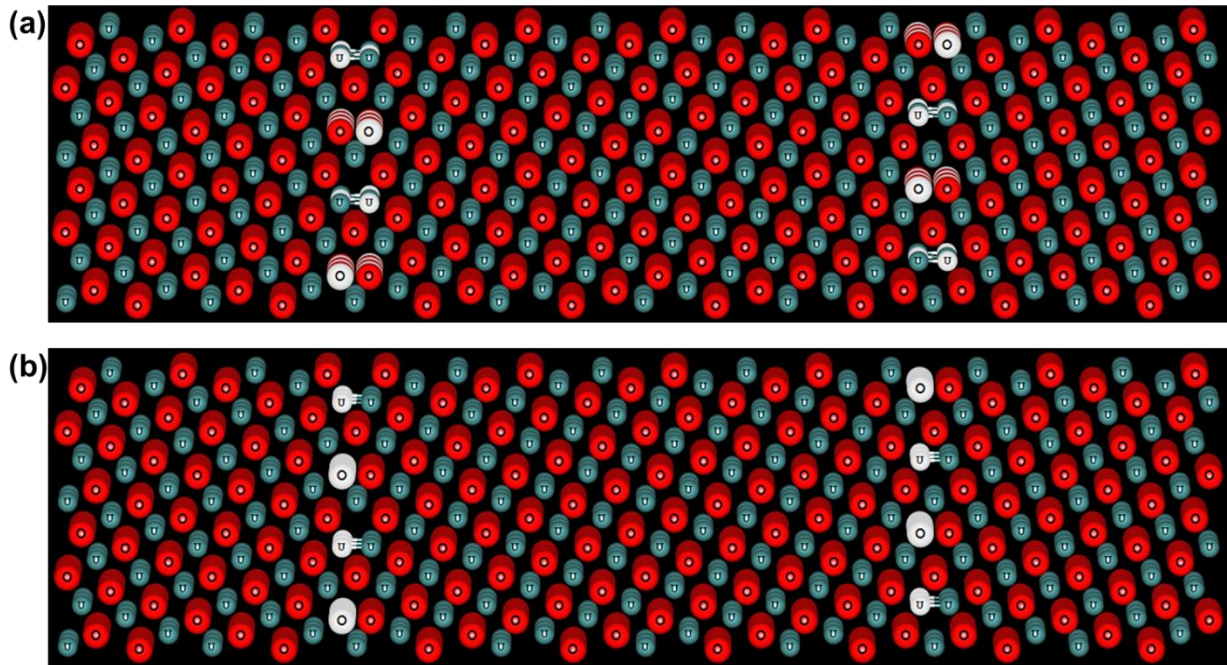


Figure A-2. Examples of selections for atoms to be removed

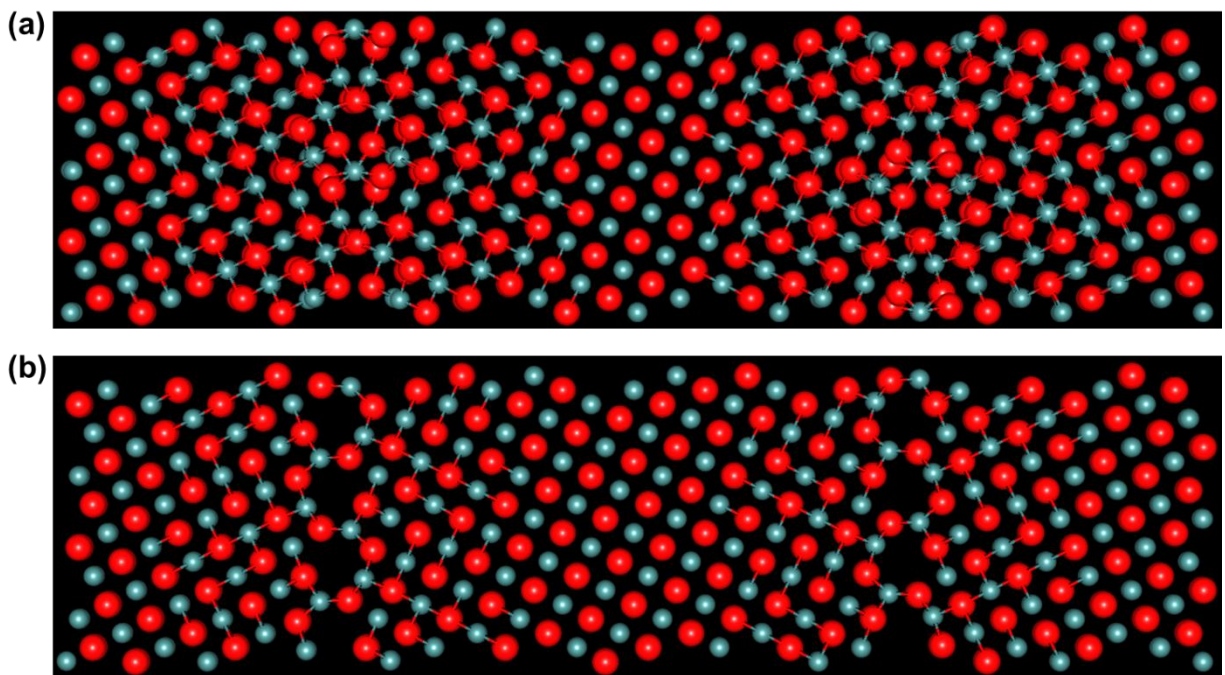


Figure A-3. Optimized  $\Sigma 5$  grain boundary structures

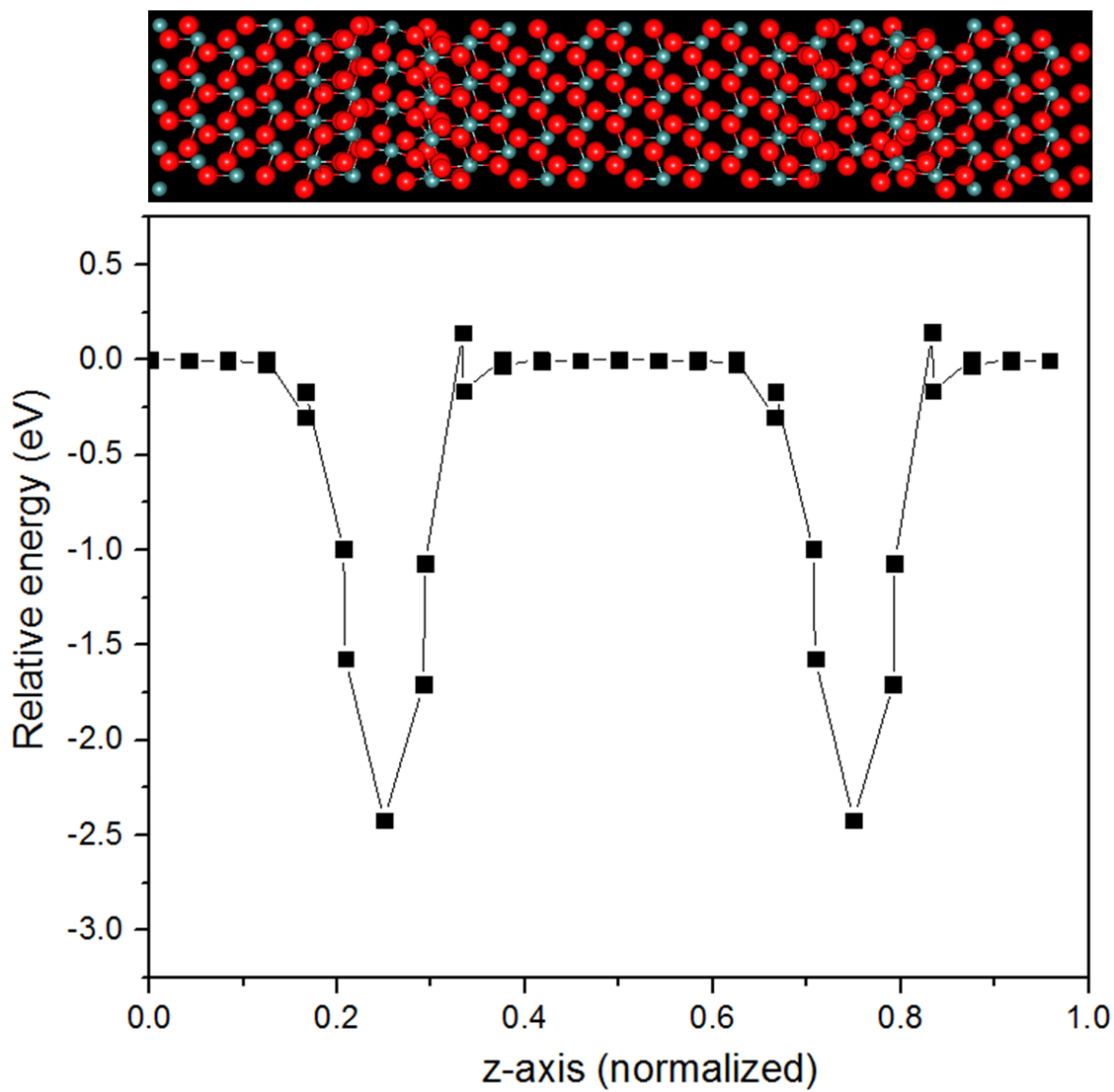


Figure A-4.  $\Sigma 3$  (111)/[111]  $\theta=60^\circ$  grain boundary and its segregation profile for Ru<sup>4+</sup>

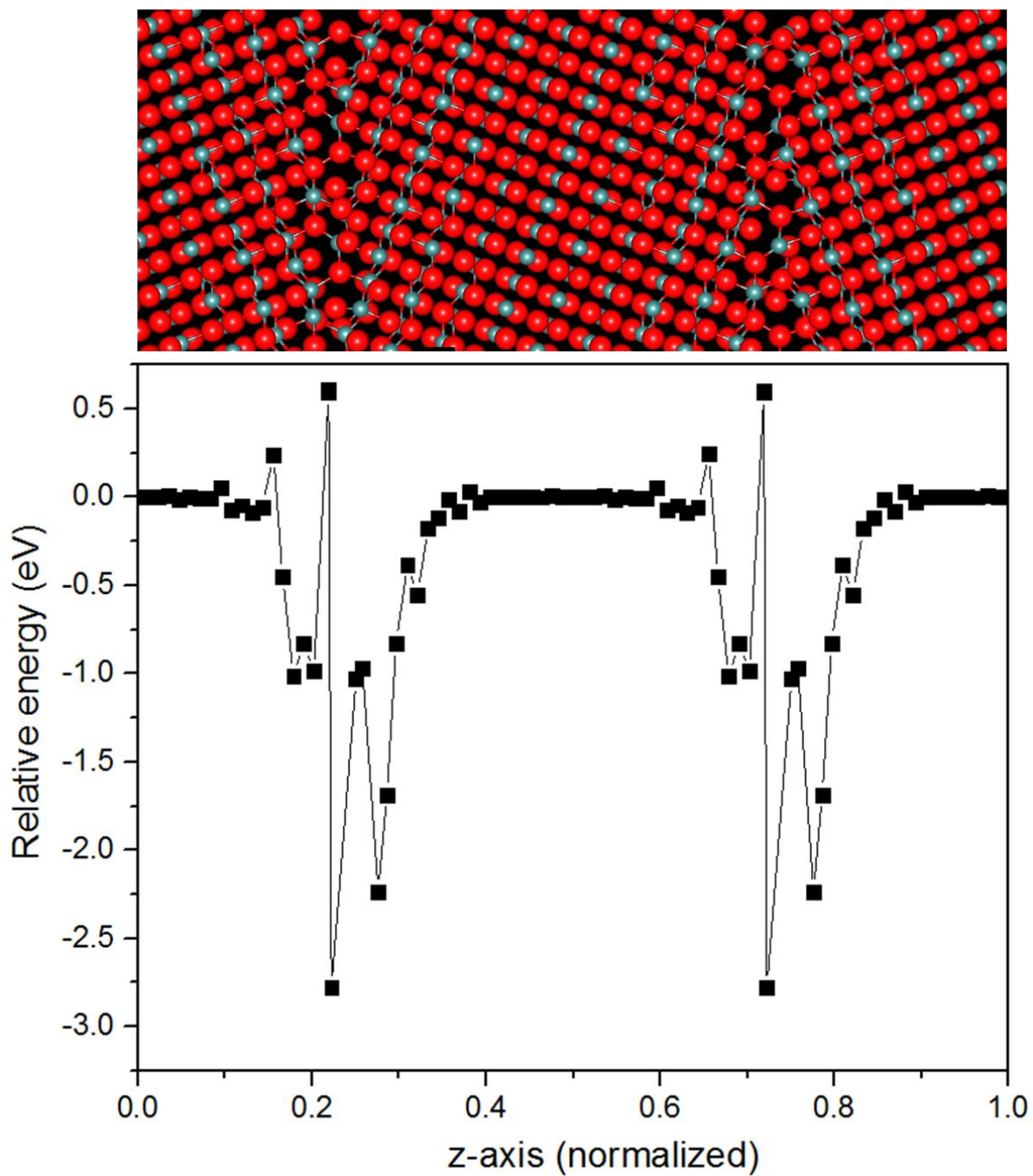


Figure A-5.  $\Sigma 7$  (3-2-1)/[111]  $\theta=38.2^\circ$  grain boundary and its segregation profile for  $\text{Ru}^{4+}$

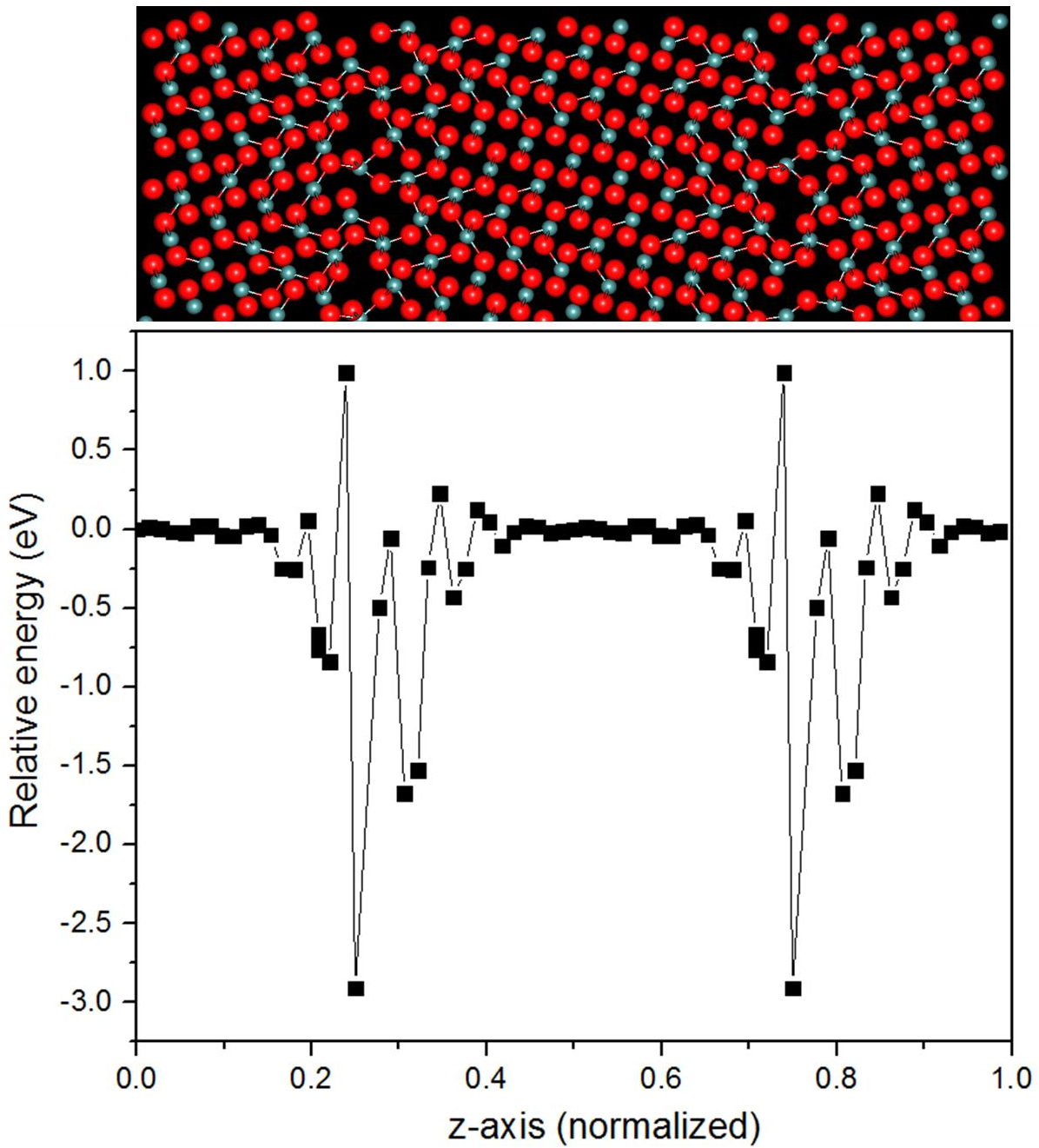


Figure A-6.  $\Sigma 9$  (2-2-1)/[110]  $\theta=38.9^\circ$  grain boundary and its segregation profile for  $\text{Ru}^{4+}$

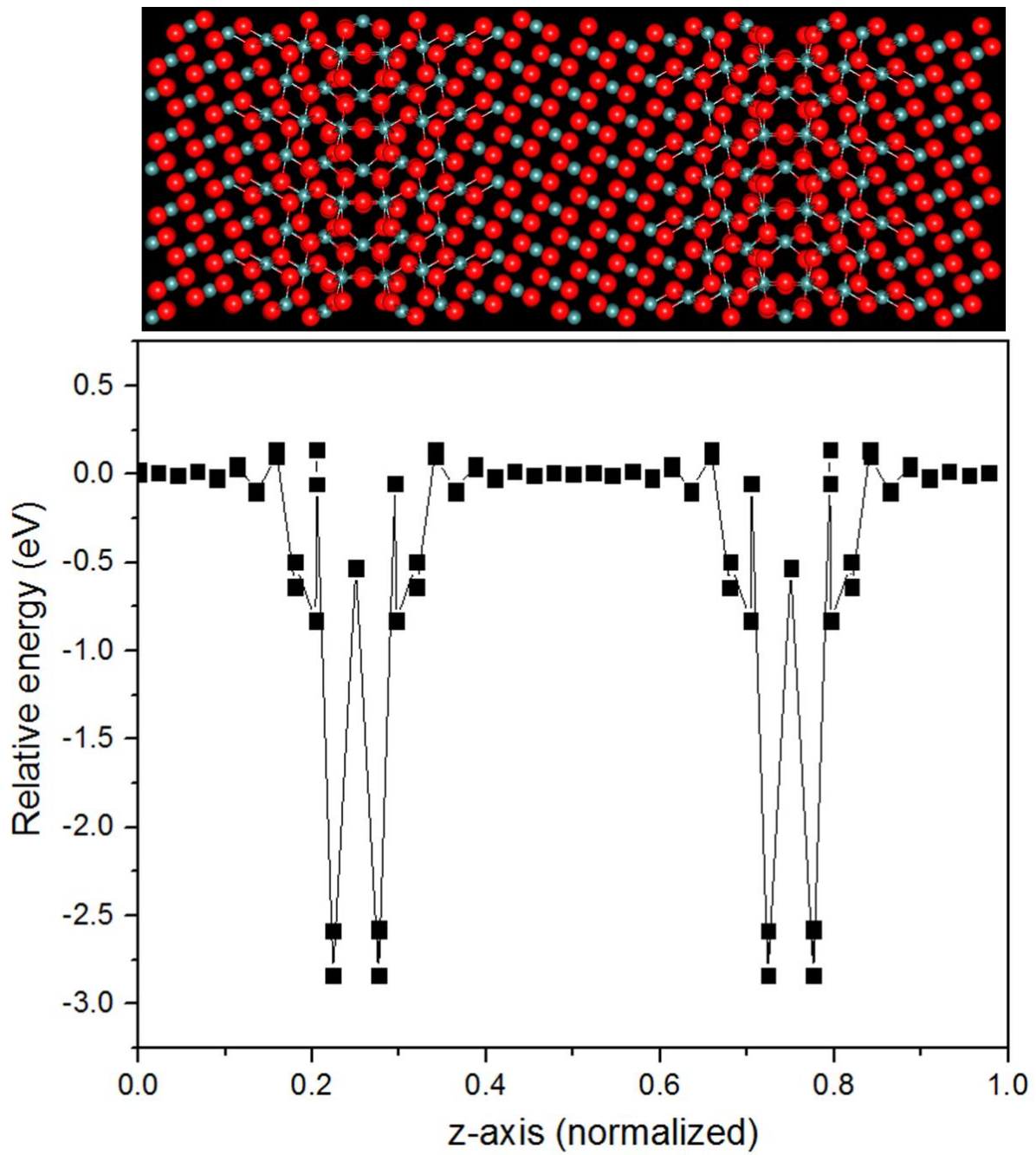


Figure A-7.  $\Sigma 11$  (1-13)/[110]  $\theta=50.5^\circ$  grain boundary and its segregation profile for Ru<sup>4+</sup>

## LIST OF REFERENCES

- 1 M. F. Lyons, R. F. Boyle, J. H. Davies, V. E. Hazel, and T. C. Rowland, *Nuclear Engineering and Design* **21**, 167 (1972).
- 2 R. E. Latta and R. E. Fryxell, *Journal of Nuclear Materials* **35**, 195 (1970).
- 3 Q. Yin and S. Y. Savrasov, *Physical Review Letters* **100** (2008).
- 4 D. R. Olander, *Fundamental Aspects of Nuclear Reactor Fuel Elements* (TID-26711-P1, 1976).
- 5 O. V. Khoruzhii, S. Y. Kourtchatov, and V. V. Likhanskii, *Journal of Nuclear Materials* **265**, 112 (1999).
- 6 H. Assmann and H. Stehle, *Nuclear Engineering and Design* **48**, 49 (1978).
- 7 M. Sugisaki, S. Sato, and H. Furuya, *Journal of Nuclear Materials* **97**, 79 (1981).
- 8 H. Hoffmann, *Journal of Nuclear Materials* **54**, 9 (1974).
- 9 R. J. Keller, T. E. Mitchell, and A. H. Heuer, *Acta Metallurgica* **36**, 1061 (1988).
- 10 J. T. A. Roberts, *Acta Metallurgica* **22**, 873 (1974).
- 11 K. C. Radeord and J. M. Pope, *Journal of Nuclear Materials* **116**, 305 (1983).
- 12 K. Kapoor, A. Ahmad, A. Lakshminarayana, and G. V. S. Hemanth Rao, *Journal of Nuclear Materials* **366**, 87 (2007).
- 13 T. R. G. Kutty, P. V. Hegde, K. B. Khan, S. Majumdar, and D. S. C. Purushotham, *Journal of Nuclear Materials* **282**, 54 (2000).
- 14 E. Zimmer, C. Ganguly, J. Borchardt, and H. Langen, *Journal of Nuclear Materials* **152**, 169 (1988).
- 15 S. Nishigaki and K. Maekawa, *Journal of Nuclear Materials* **14**, 453 (1964).
- 16 J. H. Yang, K. W. Song, K. S. Kim, and Y. H. Jung, *Journal of Nuclear Materials* **353**, 202 (2006).
- 17 B. J. Lewis, W. T. Thompson, F. Akbari, D. M. Thompson, C. Thurgood, and J. Higgs, *Journal of Nuclear Materials* **328**, 180 (2004).
- 18 S. Sunder and N. H. Miller, *Journal of Nuclear Materials* **231**, 121 (1996).
- 19 P. Taylor, D. D. Wood, D. G. Owen, and G.-I. Park, *Journal of Nuclear Materials* **183**, 105 (1991).

- 20 H. Kleykamp, Journal of Nuclear Materials **131**, 221 (1985).
- 21 N. J. Dudley, R. L. Coble, and H. L. Tuller, Journal of the American Ceramic Society **64**, 627 (1981).
- 22 J. Arborelius, et al., Journal of Nuclear Science and Technology **43**, 967 (2006).
- 23 J. C. Killeen, Journal of Nuclear Materials **88**, 177 (1980).
- 24 M. Kubo, Y. Oumi, R. Miura, A. Stirling, A. Miyamoto, M. Kawasaki, M. Yoshimoto, and H. Koinuma, Journal of Chemical Physics **109**, 8601 (1998).
- 25 G. Herranz, et al., Physical Review Letters **98**, 216803 (2007).
- 26 A. Ohtomo and H. Hwang, Nature **427**, 423 (2004).
- 27 Y. Li, et al., Applied Physics Letters **91** (2007).
- 28 E. Wieneravnear, G. L. Kerber, J. E. Mcfall, J. W. Spargo, and A. G. Toth, Applied Physics Letters **56**, 1802 (1990).
- 29 M. Kiyotoshi and K. Eguchi, Applied Physics Letters **67**, 2468 (1995).
- 30 Y. Du, M. S. Zhang, J. Wu, L. Kang, S. Yang, P. Wu, and Z. Yin, Applied Physics A **76**, 1105 (2003).
- 31 D. Bao, X. Yao, N. Wakiya, K. Shinozaki, and N. Mizutani, Applied Physics Letters **79**, 3767 (2001).
- 32 S. W. Lee, et al., Chemistry of Materials **23**, 2227 (2011).
- 33 Z. Zhang and M. G. Lagally, Science **276**, 377 (1997).
- 34 J. W. Evans, P. A. Thiel, and M. C. Bartelt, Surface Science Reports **61**, 1 (2006).
- 35 J. L. Wohlwend, C. N. Boswell, S. R. Phillpot, and S. B. Sinnott, Journal of Materials Research **24**, 1994 (2009).
- 36 J. L. Wohlwend, S. R. Phillpot, and S. B. Sinnott, Journal of Physics: Condensed Matter **22**, 045001 (2009).
- 37 J. L. Wohlwend, R. K. Behera, I. Jang, S. R. Phillpot, and S. B. Sinnott, Surface Science **603**, 873 (2009).
- 38 Z. Zhang and M. Lagally, Science **276**, 377 (1997).
- 39 C. H. Grein, R. Benedek, and T. d. I. Rubia, Computational Materials Science **6**, 123 (1996).

- 40 B. P. Uberuaga and A. F. Voter, in *Radiation Effects in Solids*, edited by K. E. Sickafus and E. A. Kotomin (Springer, 2007), p. 25.
- 41 A. F. Voter, *Journal of Chemical Physics* **106**, 4655 (1997).
- 42 S. Birner, J. Kim, D. A. Richie, J. W. Wilkins, A. F. Voter, and T. Lenosky, *Solid State Communications* **120**, 279 (2001).
- 43 E. K. Grimmelmann, J. C. Tully, and E. Helfand, *Journal of Chemical Physics* **74**, 5300 (1981).
- 44 M. R. Sorensen and A. F. Voter, *Journal of Chemical Physics* **112**, 9599 (2000).
- 45 A. F. Voter, *Physical Review B* **57**, R13985 (1998).
- 46 J. A. Sprague, F. Montalenti, B. P. Uberuaga, J. D. Kress, and A. F. Voter, *Physical Review B* **66** (2002).
- 47 Y. Shim, V. Borovikov, B. P. Uberuaga, A. F. Voter, and J. G. Amar, *Physical Review Letters* **101**, 116101 (2008).
- 48 S. PalDey and S. C. Deevi, *Materials Science and Engineering: A* **342**, 58 (2003).
- 49 M. Wittmer, *Applied Physics Letters* **36**, 456 (1980).
- 50 S. Piscanec, L. Ciacchi, E. Vesselli, G. Comelli, O. Sbaizero, S. Meriani, and A. De Vita, *Acta Materialia* **52**, 1237 (2004).
- 51 N. C. Saha and H. G. Tompkins, *Journal of Applied Physics* **72**, 3072 (1992).
- 52 L. Rebouta, F. Vaz, M. Andritschky, and M. daSilva, *Surface & Coatings Technology* **76**, 70 (1995).
- 53 H.-Y. Chen and F.-H. Lu, (AVS, 2005), p. 1006.
- 54 S. Gwo, C. Yeh, P. Chen, Y. Chou, T. Chen, T. Chao, S. Hu, and T. Huang, *Applied Physics Letters* **74**, 1090 (1999).
- 55 F. Esaka, et al., *Journal of Vacuum Science & Technology a-Vacuum Surfaces and Films* **15**, 2521 (1997).
- 56 J. Zimmermann, M. Finnis, and L. Ciacchi, *Journal of Chemical Physics* **130** (2009).
- 57 J. Graciani, J. Sanz, T. Asaki, K. Nakamura, and J. Rodriguez, *Journal of Chemical Physics* **126** (2007).
- 58 W. Göpel, G. Rocker, and R. Feierabend, *Physical Review B* **28**, 3427 (1983).

- 59 J. Segner, C. T. Campbell, G. Doyen, and G. Ertl, *Surface Science* **138**, 505 (1984).
- 60 C. A. Scamehorn, N. M. Harrison, and M. I. McCarthy, *The Journal of Chemical Physics* **101**, 1547 (1994).
- 61 U. Diebold, J. Lehman, T. Mahmoud, M. Kuhn, G. Leonardelli, W. Hebenstreit, M. Schmid, and P. Varga, *Surface Science* **411**, 137 (1998).
- 62 G. Lu, A. Linsebigler, and J. J. T. Yates, *The Journal of Chemical Physics* **102**, 4657 (1995).
- 63 T. Zambelli, J. Wintterlin, J. Trost, and G. Ertl, *Science* **273**, 1688 (1996).
- 64 Z.-P. Liu, S. J. Jenkins, and D. A. King, *Journal of the American Chemical Society* **125**, 14660 (2003).
- 65 N. B. Brookes, G. Thornton, and F. M. Quinn, *Solid State Communications* **64**, 383 (1987).
- 66 L. Giordano, J. Goniakowski, and J. Suzanne, *Physical Review Letters* **81**, 1271 (1998).
- 67 P. Gambardella, Z. Slijivancanin, B. Hammer, M. Blanc, K. Kuhnke, and K. Kern, *Physical Review Letters* **87** (2001).
- 68 Y. Xu and M. Mavrikakis, *Journal of Physical Chemistry B* **107**, 9298 (2003).
- 69 Y. Xu and M. Mavrikakis, *Surface Science* **538**, 219 (2003).
- 70 P. Taylor, *Journal of Nuclear Materials* **344**, 206 (2005).
- 71 J. J. Carbajo, G. L. Yoder, S. G. Popov, and V. K. Ivanov, *Journal of Nuclear Materials* **299**, 181 (2001).
- 72 C. T. Walker, D. Staicu, M. Sheindlin, D. Papaioannou, W. Goll, and F. Sontheimer, *Journal of Nuclear Materials* **350**, 19 (2006).
- 73 H. Bailly, *The Nuclear Fuel of Pressurized Water Reactors and Fast Reactors: design and behavior* (Lavoisier Publishing, 1999).
- 74 D. Frenkel and B. Smit, *Understanding Molecular simulation : From Algorithms to Applications* (Academic Press, San Diego, 2005).
- 75 P. Hohenberg and W. Kohn, *Physical Review B* **136**, B864 (1964).
- 76 M. P. Allen and D. J. Tildesley, *Computer Simulation of Liquids* (Oxford University Press Inc., New York, 1987).

- 77 P. P. Ewald, *Z Kristallogr* **56**, 129 (1921).
- 78 R. A. Buckingham, *Proc R Soc Lon Ser-A* **168**, 264 (1938).
- 79 W. Kohn and L. J. Sham, *Phys Rev* **140**, 1133 (1965).
- 80 J. P. Perdew, K. Burke, and M. Ernzerhof, *Physical Review Letters* **78**, 1396 (1997).
- 81 G. Kresse and J. Hafner, *Physical Review B* **47**, 558 (1993).
- 82 G. Kresse and J. Furthmüller, *Physical Review B* **54**, 11169 (1996).
- 83 P. E. Blochl, *Physical Review B* **50**, 17953 (1994).
- 84 G. Henkelman, B. P. Uberuaga, and H. Jonsson, *Journal of Chemical Physics* **113**, 9901 (2000).
- 85 L. T. Kong and L. J. Lewis, *Physical Review B* **74**, 073412 (2006).
- 86 H. Yildirim, A. Kara, S. Durukanoglu, and T. S. Rahman, *Surface Science* **600**, 484 (2006).
- 87 C. R. A. Catlow, *Radiation Effects and Defects in Solids* **53**, 127 (1980).
- 88 C. R. A. Catlow, *Journal of Nuclear Materials* **79**, 432 (1979).
- 89 R. W. Grimes and C. R. A. Catlow, *Philos T Roy Soc A* **335**, 609 (1991).
- 90 W. Zhang, J. R. Smith, and X. G. Wang, *Physical Review B* **70**, 024103 (2004).
- 91 M. W. Finnis, A. Y. Lozovoi, and A. Alavi, *Annual Review of Materials Research* **35**, 167 (2005).
- 92 K. Reuter and M. Scheffler, *Physical Review B* **65**, 035406 (2001).
- 93 J. He, R. K. Behera, M. W. Finnis, X. Li, E. C. Dickey, S. R. Phillpot, and S. B. Sinnott, *Acta Materialia* **55**, 4325 (2007).
- 94 H. Y. Geng, Y. Chen, Y. Kaneta, and M. Kinoshita, *Journal of Alloys and Compounds* **457**, 465 (2008).
- 95 A. Jelea, M. Colbert, F. Ribeiro, G. Treglia, and R. J. M. Pellenq, *Journal of Nuclear Materials* **415**, 210 (2011).
- 96 T. Petit, G. Jomard, C. Lemaignan, B. Bigot, and A. Pasturel, *Journal of Nuclear Materials* **275**, 119 (1999).
- 97 C. R. Stanek and R. W. Grimes, *Journal of Nuclear Materials* **282**, 265 (2000).

- 98 J. P. Crocombette, Journal of Nuclear Materials **305**, 29 (2002).
- 99 G. Brillant and A. Pasturel, Physical Review B **77** (2008).
- 100 B. Dorado, M. Freyss, and G. Martin, Eur Phys J B **69**, 203 (2009).
- 101 G. Brillant, F. Gupta, and A. Pasturel, J Phys-Condens Mat **21** (2009).
- 102 P. V. Nerikar, X. Y. Liu, B. P. Uberuaga, C. R. Stanek, S. R. Phillpot, and S. B. Sinnott, J Phys-Condens Mat **21** (2009).
- 103 G. Brillant, F. Gupta, and A. Pasturel, Journal of Nuclear Materials **412**, 170 (2011).
- 104 F. Gupta, G. Brillant, and A. Pasturel, Philos Mag **87**, 2561 (2007).
- 105 J. P. Crocombette, F. Jollet, L. N. Nga, and T. Petit, Physical Review B **6410** (2001).
- 106 M. Freyss, T. Petit, and J. P. Crocombette, Journal of Nuclear Materials **347**, 44 (2005).
- 107 M. Iwasawa, Y. Chen, Y. Kaneta, T. Ohnuma, H.-Y. Geng, and M. Kinoshita, MATERIALS TRANSACTIONS **47**, 2651 (2006).
- 108 H. Y. Geng, Y. Chen, Y. Kaneta, M. Iwasawa, T. Ohnuma, and M. Kinoshita, Physical Review B **77** (2008).
- 109 H. Matzke, J Chem Soc Farad T 2 **83**, 1121 (1987).
- 110 C. G. Van de Walle and J. Neugebauer, J Appl Phys **95**, 3851 (2004).
- 111 H. Wang and W. F. Schneider, The Journal of Chemical Physics **127**, 064706 (2007).
- 112 D. Lide, *CRC Handbook of Chemistry and Physics, 88th Edition (CRC Handbook of Chemistry & Physics)* (CRC Press, 2007).
- 113 P. J. Kelly and M. S. S. Brooks, J Chem Soc Farad T 2 **83**, 1189 (1987).
- 114 T. Petit, C. Lemaignan, F. Jollet, B. Bigot, and A. Pasturel, Philos Mag B **77**, 779 (1998).
- 115 V. I. Anisimov and O. Gunnarsson, Physical Review B **43**, 7570 (1991).
- 116 A. I. Liechtenstein, V. I. Anisimov, and J. Zaanen, Physical Review B **52**, R5467 (1995).

- 117 V. I. Anisimov, F. Aryasetiawan, and A. I. Lichtenstein, *J Phys-Condens Mat* **9**, 767 (1997).
- 118 L. Petit, A. Svane, Z. Szotek, and W. M. Temmerman, *Science* **301**, 498 (2003).
- 119 I. D. Prodan, G. E. Scuseria, and R. L. Martin, *Physical Review B* **76** (2007).
- 120 S. L. Dudarev, D. N. Manh, and A. P. Sutton, *Philos Mag B* **75**, 613 (1997).
- 121 B. Dorado, G. Jomard, M. Freyss, and M. Bertolus, *Physical Review B* **82** (2010).
- 122 B. Dorado, B. Amadon, M. Freyss, and M. Bertolus, *Physical Review B* **79** (2009).
- 123 H. J. Monkhorst and J. D. Pack, *Physical Review B* **13**, 5188 (1976).
- 124 P. Nerikar, T. Watanabe, J. S. Tulenko, S. R. Phillpot, and S. B. Sinnott, *Journal of Nuclear Materials* **384**, 61 (2009).
- 125 A. B. Lidiard, *Journal of Nuclear Materials* **19**, 106 (1966).
- 126 G. H. Lander, E. S. Fisher, and S. D. Bader, *Advances in Physics* **43**, 1 (1994).
- 127 H. Zhu, C. Tang, and R. Ramprasad, *Physical Review B* **82** (2010).
- 128 J. G. Yu, R. Devanathan, and W. J. Weber, *J Phys-Condens Mat* **21** (2009).
- 129 C. Mun, L. Cantrel, and C. Madic, *Nuclear Technology* **156**, 332 (2006).
- 130 H. Y. Geng, Y. Chen, Y. Kaneta, and M. Kinoshita, *Physical Review B* **77**, 180101 (2008).
- 131 G. Busker, R. W. Grimes, and M. R. Bradford, *Journal of Nuclear Materials* **312**, 156 (2003).
- 132 W. D. Kingery, H. K. Bowen, and D. R. Uhlmann, *Introduction To Ceramics* (Wiley-Interscience, New York, 1976).
- 133 P. V. Nerikar, et al., *Journal of the American Ceramic Society* **94**, 1893 (2011).
- 134 H. Ogawa, *Materials Transactions* **47**, 2706 (2006).
- 135 P. Nerikar, C. R. Stanek, S. R. Phillpot, S. B. Sinnott, and B. P. Uberuaga, *Physical Review B* **81** (2010).
- 136 Z. G. Mao, S. B. Sinnott, and E. C. Dickey, *Journal of the American Ceramic Society* **85**, 1594 (2002).

- 137 Y. Lei, Y. Ito, N. Browning, and T. Mazanec, *Journal of the American Ceramic Society* **85**, 2359 (2002).
- 138 J. D. Gale, *Journal of the Chemical Society-Faraday Transactions* **93**, 629 (1997).
- 139 E. Dickey, X. Fan, and S. Pennycook, *Journal of the American Ceramic Society* **84**, 1361 (2001).
- 140 C. B. Basak, A. K. Sengupta, and H. S. Kamath, *Journal of Alloys and Compounds* **360**, 210 (2003).
- 141 M. Abramowski, R. W. Grimes, and S. Owens, *Journal of Nuclear Materials* **275**, 12 (1999).
- 142 G. Busker, R. W. Grimes, and M. R. Bradford, *Journal of Nuclear Materials* **279**, 46 (2000).
- 143 P. V. Nerikar, D. C. Parfitt, L. A. C. Trujillo, D. A. Andersson, C. Unal, S. B. Sinnott, R. W. Grimes, B. P. Uberuaga, and C. R. Stanek, *Physical Review B* **84** (2011).
- 144 M. Hagen and M. W. Finnis, *Philosophical Magazine A* **77**, 447 (1998).
- 145 G. Henkelman, A. Arnaldsson, and H. Jonsson, *Computational Materials Science* **36**, 354 (2006).
- 146 A. P. Sutton and R. W. Balluffi, *Interfaces in crystalline materials* (Oxford University Press, New York, 1995).
- 147 J. P. Buban, K. Matsunaga, J. Chen, N. Shibata, W. Y. Ching, T. Yamamoto, and Y. Ikuhara, *Science* **311**, 212 (2006).
- 148 Y. Sato, J. P. Buban, T. Mizoguchi, N. Shibata, M. Yodogawa, T. Yamamoto, and Y. Ikuhara, *Physical Review Letters* **97** (2006).
- 149 K. Nakatani, H. Nagayama, H. Yoshida, T. Yamamoto, and T. Sakuma, *Scripta Materialia* **49**, 791 (2003).
- 150 C. Elsässer and A. G. Marinopoulos, *Acta Materialia* **49**, 2951 (2001).
- 151 R. D. Shannon, *Acta Crystallographica Section a* **32**, 751 (1976).
- 152 C. R. Stanek, M. R. Bradford, and R. W. Grimes, *Journal of Physics: Condensed Matter* **16**, S2699 (2004).
- 153 M. Hong, S. R. Phillpot, C.-W. Lee, P. V. Nerikar, B. P. Uberuaga, C. R. Stanek, and S. B. Sinnott, *Physical Review B* **85** (2012).

- 154 J. C. Killeen, Journal of Nuclear Materials **58**, 39 (1975).
- 155 J. C. Killeen, Journal of Nuclear Materials **88**, 177 (1980).
- 156 L. Bourgeois, P. Dehaudt, C. Lemaignan, and J. P. Fredric, Journal of Nuclear Materials **295**, 73 (2001).
- 157 A. Leenaers, L. de Tollenaere, C. Delafoy, and S. Van den Berghe, Journal of Nuclear Materials **317**, 62 (2003).
- 158 J. H. Cho, M. P. Harmer, H. M. Chan, J. M. Rickman, and A. M. Thompson, Journal of the American Ceramic Society **80**, 1013 (1997).
- 159 A. Kuwabara, M. Nakano, H. Yoshida, Y. Ikuhara, and T. Sakuma, Acta Materialia **52**, 5563 (2004).
- 160 M. Kim, G. Duscher, N. Browning, K. Sohlberg, S. Pantelides, and S. Pennycook, Physical Review Letters **86**, 4056 (2001).
- 161 G. Busker, Imperial College, (2002).
- 162 D. A. Andersson, B. P. Uberuaga, P. V. Nerikar, C. Unal, and C. R. Stanek, Physical Review B **84**, 054105 (2011).
- 163 H. Yoshida, K. Morita, B. Kim, K. Hiraga, and T. Yamamoto, Acta Materialia **57**, 3029 (2009).
- 164 M. Boniecki, Y. Natanzon, and Z. Lodziana, Journal of the European Ceramic Society **30**, 657 (2010).
- 165 H. Yoshida, S. Hashimoto, and T. Yamamoto, Acta Materialia **53**, 433 (2005).
- 166 C. S. Barrett, M. H. Mueller, and Hitterma.RI, Phys Rev **129**, 625 (1963).
- 167 S. Sekiguchi, M. Fujimoto, M. Nomura, S.-B. Cho, J. Tanaka, T. Nishihara, M.-G. Kang, and H.-H. Park, Solid State Ionics **108**, 73 (1998).
- 168 P. P. Ewald, Annalen Der Physik **64**, 253 (1921).
- 169 D. Wolf, P. Keblinski, S. R. Phillpot, and J. Eggebrecht, The Journal of Chemical Physics **110**, 8254 (1999).
- 170 D. E. Parry, Surface Science **49**, 433 (1975).
- 171 J. Perdew, K. Burke, and M. Ernzerhof, Physical Review Letters **78**, 1396 (1997).
- 172 T. E. Karakasidis and E. Vamvakopoulos, Surface Science **600**, 1952 (2006).

- 173 G. Henkelman, B. P. Uberuaga, D. J. Harris, J. H. Harding, and N. L. Allan, Physical Review B **72**, 115437 (2005).
- 174 R. F. W. Bader and H. Essen, The Journal of Chemical Physics **80**, 1943 (1984).
- 175 W. Wunderlich, M. Fujimoto, and H. Ohsato, Thin Solid Films **375**, 9 (2000).
- 176 M. Kawai, D. Kan, S. Isojima, H. Kurata, S. Isoda, Y. Shimakawa, S. Kimura, and O. Sakata, Journal of Applied Physics **102**, 114311 (2007).
- 177 J. L. Maurice, et al., Materials Science and Engineering: B **144**, 1 (2007).
- 178 N. C. Bristowe, P. B. Littlewood, and E. Artacho, Physical Review B **83**, 205405 (2011).
- 179 Z. Bi, B. P. Uberuaga, L. J. Vernon, E. Fu, Y. Wang, N. Li, H. Wang, A. Misra, and Q. X. Jia, Journal of Applied Physics **113**, 023513 (2013).
- 180 M. A. Wall, D. G. Cahill, I. Petrov, D. Gall, and J. E. Greene, Physical Review B **70** (2004).
- 181 Z. Liu, P. Hu, and A. Alavi, Journal of the American Chemical Society **124**, 14770 (2002).
- 182 A. Eichler and J. Hafner, Physical Review Letters **79**, 4481 (1997).
- 183 L. C. Ciacchi and M. C. Payne, Physical Review Letters **92** (2004).
- 184 A. Grosz, A. Eichler, J. Hafner, M. J. Mehl, and D. A. Papaconstantopoulos, Surface Science **539**, 542 (2003).
- 185 G. Henkelman and H. Jonsson, Journal of Chemical Physics **113**, 9978 (2000).

## BIOGRAPHICAL SKETCH

Minki Hong was born in 1979 in Kunsan, a small and humble city in Republic of Korea (South Korea). After three relocations over a decade, his parents permanently settled down in Seoul, the capital of South Korea, hoping better education for their children in 1990. He graduated from Seoul High School, one of the three renowned high schools in Korea, in 1997 and in the same year, he began his undergraduate studies in the Department of Materials Science and Engineering at Yonsei University, one of the top three universities in Korea. After all, his parents made the right decision back in 1990.

He earned his Bachelor and Master degree in the same department at Yonsei University in 2001 and 2003 respectively: his Master thesis was entitled as "*The growth and characterization of ZnO nanowires*". Several months later, he entered the Officer Candidate School (OCS) of the R.O.K NAVY and then became a navy officer after four months of harsh training. He served his country for three years as a research officer in the Naval Technology Development Center (NTDC) and then resigned as Lieutenant Jr. Grade Officer in 2007. In 2008, he entered the Department of Materials Science and Engineering at University of Florida and after around a year, he joined the Computational Materials Science Focus Group. He had been involved various researches related to nuclear materials, thin films, catalysis, as well as radioactive detectors in collaboration with experiments. In August 2013, he received his Ph.D. in materials science and engineering from the University of Florida.